AERODYNAMIC PERFORMANCE

OF

WIND TURBINES

by

Robert E. Wilson
Oregon State University
Corvallis, Oregon

and

Peter B. S. Lissaman
Aerovironment, Inc.
Pasadena, California

and

Stel N. Walker
Oregon State University
Corvallis, Oregon

June, 1976

TABLE OF CONTENTS

Table of Contents (cont'd) page

CHAPTER I

INTRODUCTION

Since the publication of "Applied Aerodynamics of Wind Power Machines"[1] in 1974, additional work has been accomplished on analytical performance prediction methods for wind turbines. This report summarizes the state-of-the-art of performance prediction methods for both horizontal and vertical axis wind turbines.

Strip theory methods for horizontal axis wind turbines are evaluated for various tip loss models in Chapter 2. A comparison of these tip models is developed for the ERDA-NASA MOD-0 rotor. The occurrence of multiple solutions in strip theory analysis is discussed and illustrated. Chapter 2 also treats the performance of high-solidity turbines such as the Chalk design. Corrections to the strip analysis techniques are developed and incorporated into the analysis used for conventional horizontal axis wind turbines. The predicted performance of the Chalk Turbines is presented and discussed.

The configuration and performance of optimum horizontal axis wind turbines is addressed in Chapter 3. While optimization techniques are well developed for propellers, the situation is not as straightforward for wind turbines. Optimization schemes are developed and discussed and comparisons with the MOD-0 rotor are made. Performance at off-design conditions is also examined.

The final two chapters deal with performance prediction methods for vertical axis wind turbines. In Chapter 4 the performance model for the Darrieus Rotor is developed. Both linear and non-linear theories are developed. Multiple solutions are found to occur for Darrieus Rotors in the same

manner as occurs for horizontal axis rotors. This flow model is compared to existing experimental data and shown to yield excellent agreement.

Chapter 5 contains an analytical model of the flow in a Savonius Rotor. The flow model is shown to predict the essential features of flow in Savonius Rotors with consideration of viscous effects.

1.1 WIND TURBINE TEST DATA

The amount of test data available for wind turbines is surprisingly small and because of the scarcity of test data, performance analysis techniques often lack adequate verification. In the case of horizontal axis wind turbines there exist only two series of wind tunnel model tests[2,3] that are fully documented. Figures 1.1.1, 1.1.2 and 1.1.3 illustrate presently available test

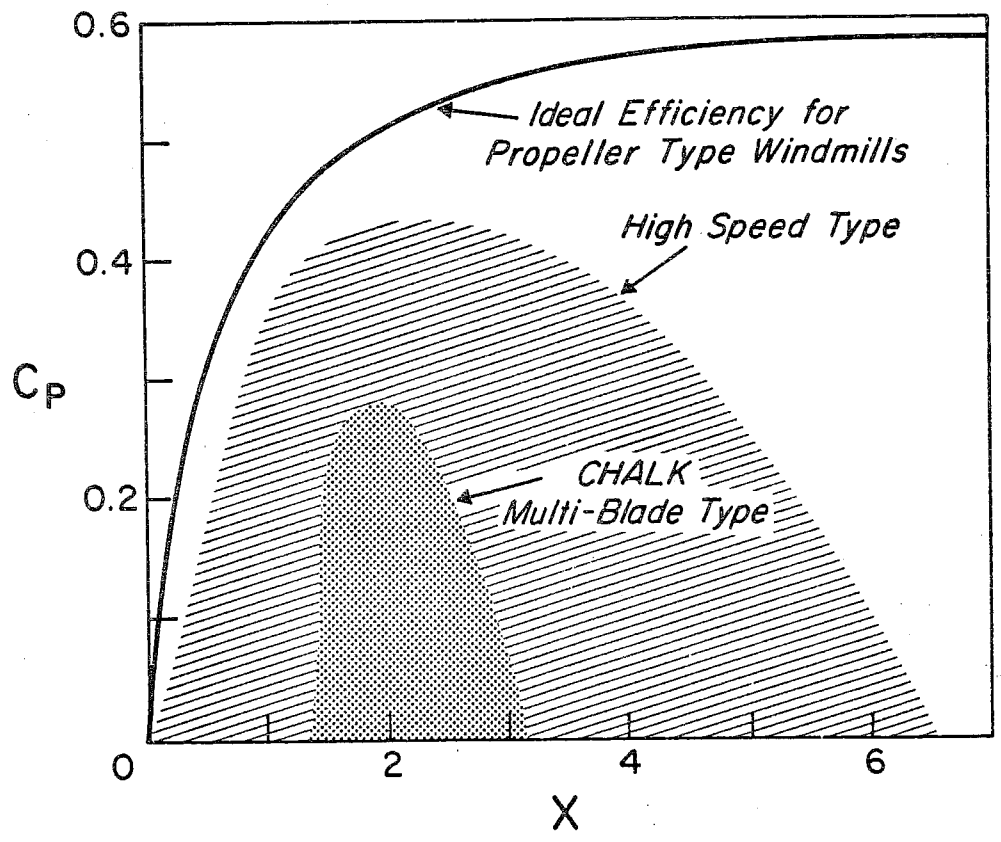

Figure 1.1.1 Experimental Data Envelopes for Horizontal Axis Machines.

data for various types of wind powered machines. Figure 1.1.3 illustrates the maximum values of the power coefficient that have been measured for each general type of machine. Again the present lack of experimental data for horizontal axis wind turbines is noted, particularly at high tip-speed ratios. In each chapter, available experimental data is compared to theory. The blockage effects for wind tunnel testing of wind turbines are large and in many cases in literature, no mention is made of the magnitude of the blockage corrections. Accordingly, the next section includes a discussion of wind tunnel corrections.

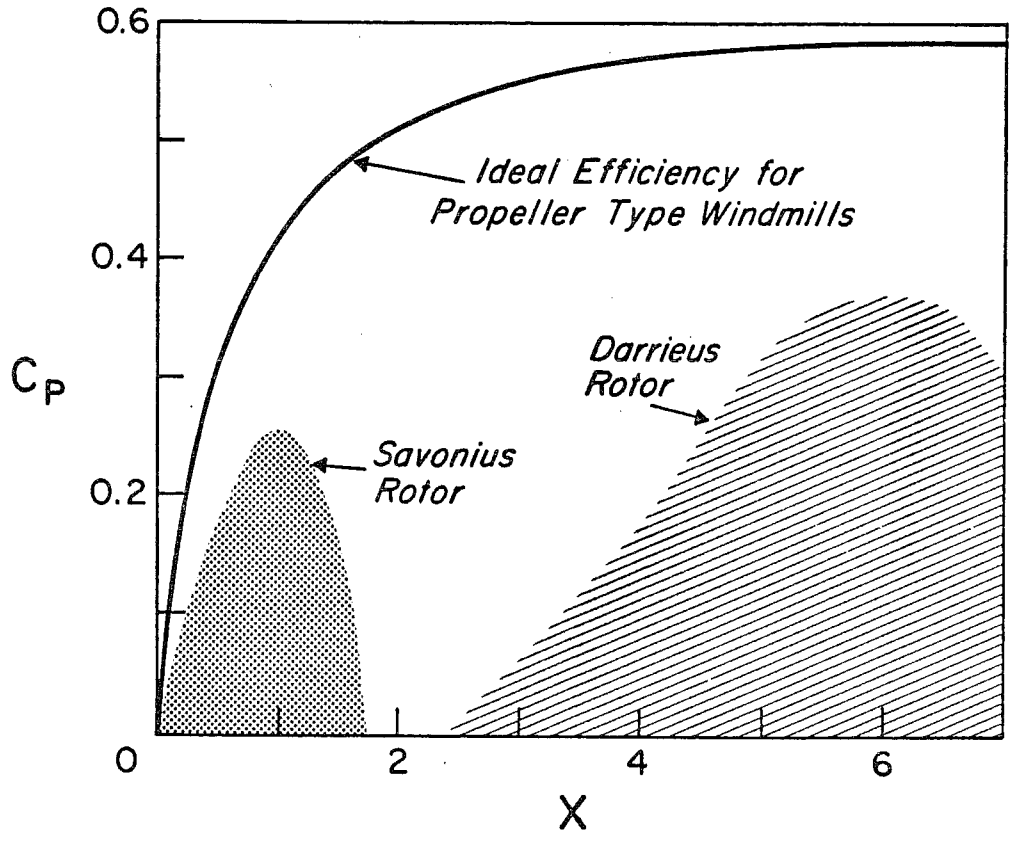

Figure 1.1.2 Experimental Data Envelopes for Vertical Axis Machines.

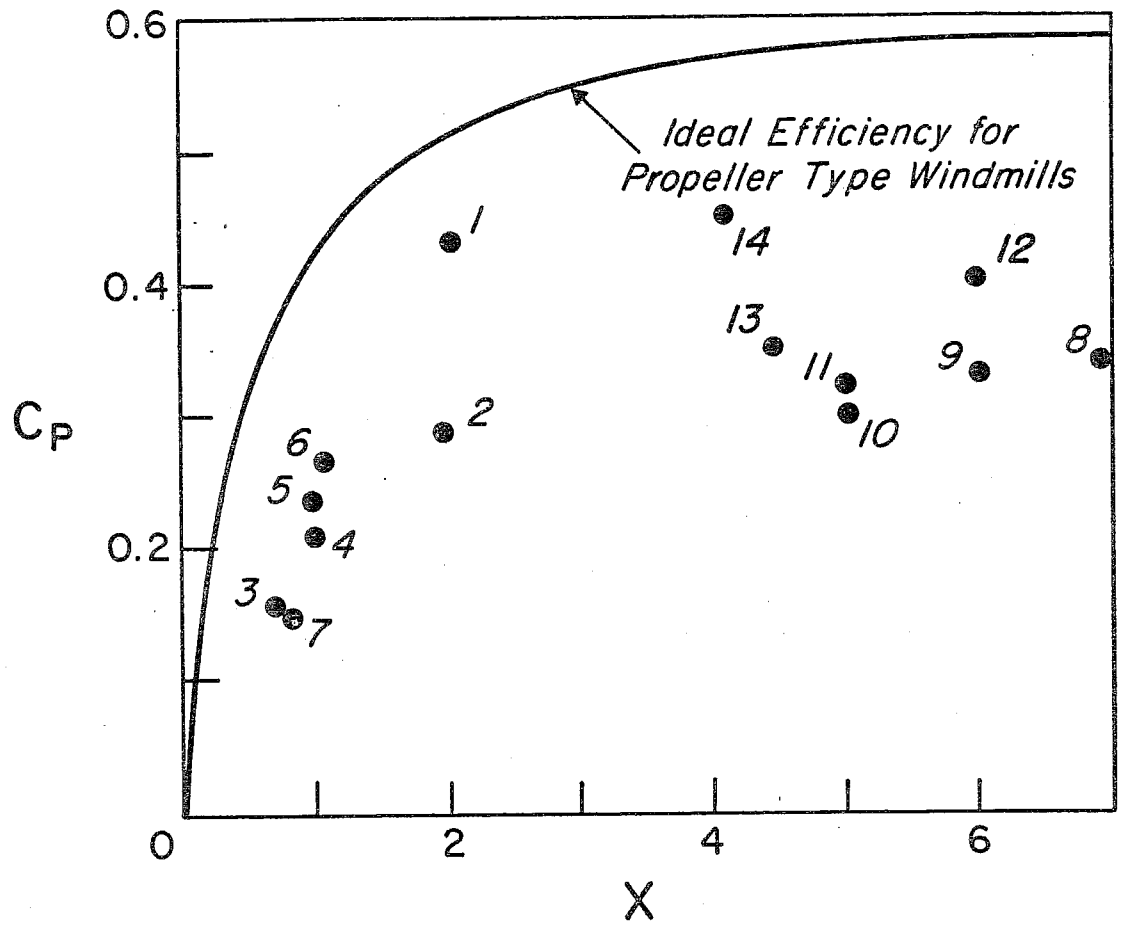

PROPELLER TYPE

1. Iwasaki (3)
2. McLaughlin (4)
12. NYU-Standford (2)
14. Sweeney (19)

SAVONIUS

3. Simonds-Bodek (5)
4. Bach (6)
5. New York Univ. (2)
6. Newman (7)
7. Mercier (8)

DARRIEUS

8. South-Rangi (9)
9. South-Rangi (10)
10. Muraca (11)
11. South-Rangi (13)
13. Blackwell-Sheldahl-Feltz (17)

Figure 1.1.3 Maximum Measured Power Coefficient for Various Type Wind Turbines.

1.2 WIND TUNNEL CORRECTIONS FOR WIND TURBINE TESTING

The wind tunnel imposes a constraint on the wind turbine by limiting the extent of the free air stream. The flow past the wind turbine is constrained, and the uniform axial velocity V_∞ which occurs in front of the wind turbine differs from that which would occur if it was operating under the same torque conditions in the free stream. In general, it turns out that the equivalent free stream velocity V' is less than that of the wind tunnel. The magnitude of this reduction can be determined by applying the axial momentum theory, which neglects the rotational motion of the slipstream. Using the method developed by Glauert[12] for propellers, the correction for blockage may be determined for wind turbines. Figure 1.2.1 gives the power coefficient corrections as a function of the observed thrust coefficient.

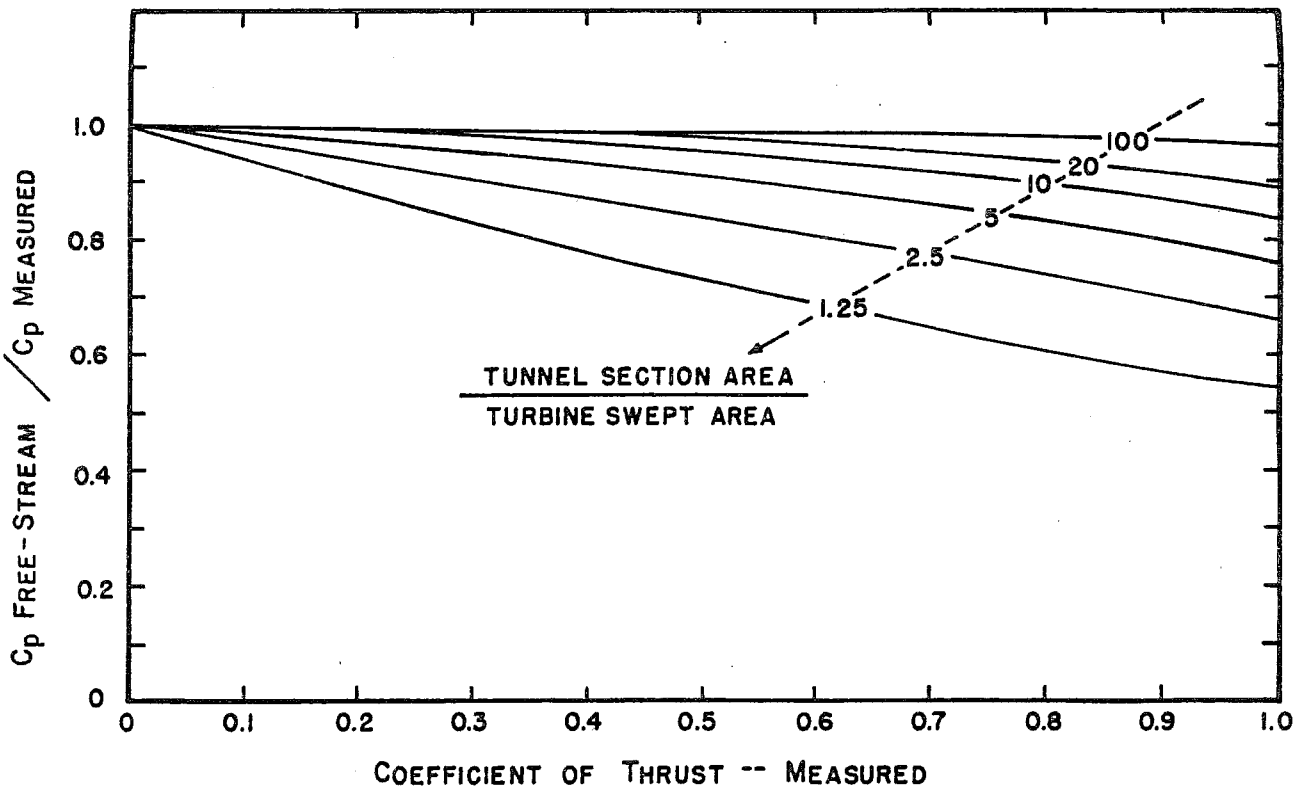

Figure 1.2.1 Blockage Correction for Wind Turbine Testing.

REFERENCES

1. Wilson, R. E. and Lissaman, Peter B. S., "Applied Aerodynamics of Wind Powered Machines," Oregon State University, May 1974.

2. N.Y.U. Final Report on the Wind Turbine, Office of Production, Research and Development WAR Production Board, PB 25370, Washington, D.C., January 31, 1946.

3. Iwasaki, Matsonosoka, "The Experimental and Theoretical Investigations of Windmills," Reports of Research Institute for Applied Mechanics, Kyushu University, Vol. II, No. 8, 1953.

4. McLaughlin, Dennis K., "Preliminary Performance Data on the Chalk Wind Turbine," Unpublished, Oklahoma State University, December 1975.

5. Simonds, M. H. and Bodek, A., "Performance Test of A Savonius Rotor," Brace Research Institute, T.R. T10, McGill University, 1964.

6. Bach, von G., Untersuchungen uber Savonius-Rotoren und verwandte Stromungsmaschmen, Forsch. auf dem Gebiete des Ingenieurwesens, 2, pp. 218-231, 1931.

7. Newman, B. G., "Measurements on a Savonius Rotor with Variable Gap," Sherbrooke University Symposium on Wind Energy, May 1974.

8. Mercier, John A., "Power Generating Characteristics of Savonius Rotors," Davidson Lab, Stevens Institute of Technology, Report 1181, 1966.

9. South, P. and Rangi, R. S., "Preliminary Tests of a High Speed Vertical Axis Windmill Model," NRC, NAE LTR-LA-74, March 1971.

10. South, P. and Rangi, R. S., "A Wind Tunnel Investigation of a 14 ft. Diameter Vertical Axis Windmill," NRC, NAE LTR-L-105, September 1972.

11. Muraca, Ralph J., "Wind Tunnel Investigation of a 14 ft. Vertical Axis Windmill," NASA-LANGLEY Research Center, Technical Note in Preparation, May 1975.

12. Glauert, H.; Durand, W. F. (Ed.), Aerodynamic Theory, "Airplane Propellers," Vol. IV, Division I, Chapter VII, Section 4, pp. 169-360, Julius Springer, Berlin, 1935.

13. South, P. and Rangi, R., "The Performance and Economics of the Vertical-Axis Wind Turbine Developed at the National Research Council, Ottawa, Canada," Presented at the 1973 Annual Meeting of the Pacific Northwest Region of the American Society of Agricultural Engineers, Calgary, Alberta, October 10-12, 1973.

14. Culver, F. S., "Performance of Two Successful Windmill Generating Plants," Electrical World, Vol. 69, pp. 367-369, February 24, 1917.

15. Blazdell, C., "A Six-Foot Experimental Wind Motor," Model Engineer and Electrician, Vol. 41, pp. 145-151, August 14, 1919; pp 171-178, August 21, 1919.

16. Pancratz, F. J., "Wind Power for Farm Electric Plants," Mechanical Engineering, Vol. 46, pp. 675-682, November 1924.

17. Blackwell, Bennie F.; Sheldahl, Robert E., and Feltz, Louis V., "Wind Tunnel Performance Data for the Darrieus Wind Turbine with NACA 0012 Blades," Sandia Laboratories, SAND76-0130, May 1976.

18. Sweeney, T. E., et al, "Sailwing Windmill Characteristics and Related Topics," Princeton University Report, AMS Report No. 1240, NSF/RANN/GI-41891/PR/74/4, Spring 1975.

19. Sweeney, T. E., et al, "The Performance Characteristics of a Two-Bladed Sailwing Windmill Rotor and Related Topics," Princeton University Report, AMS Report No. 1254, NSF/RANN/GI-41891/PR/75/2, Fall 1975.

CHAPTER II

PERFORMANCE AERODYNAMICS OF HORIZONTAL AXIS ROTORS

INTRODUCTION

The propeller type wind turbine can be considered to be an airscrew which extracts energy from the driving air and converts it into a mechanical form in contrast to a propeller which expels energy into the air from another energy source. The similarity of the propeller and the wind turbine enables the same theoretical development to be followed for performance analysis. Propeller theory developed along two independent methods of approach, one of which has been called momentum theory and the other, blade element theory.

Momentum theory was first developed by W. J. M. Rankine[1] in 1865 and later improved by R. E. Froude[2]. The basis of the theory is the determination of the forces acting on the rotor to produce the motion of the fluid. The theory has been useful in predicting ideal efficiency and flow velocity, but it gives no information concerning the blade shape necessary to generate the fluid motion. Rotational effects of the wake were included in the theory by A. Betz[3].

Blade element theory was originated by W. Froude[4] in 1878 and developed by S. Drzewiecki[5]. The approach of blade element theory is opposite of that of momentum in that the concern is with the forces produced by the blades as a result of the motion of the fluid. It was hampered in its original development by lack of knowledge of sectional aerodynamics and mutual interference of blades.

Modern propeller theory has developed from the concept of free vortices being shed from the rotating blades. These vortices define a slipstream and generate induced velocities. The theory can be attributed to the work of Lanchester[6] and Flamm[7] for the original concept; to Joukowski[8], for induced velocity analysis; to A. Betz[9], for optimization; to L. Prandtl[10] and S. Goldstein[11], for circulation distribution or tip loss analysis; and H. Glauert[12, 13 and 14], E. Pistolesti[15], and S. Kawada[16], for general improvements. The theory has been referred to by a number of names: vortex theory, modified blade element theory, and strip theory.

This is the most frequently used theory for performance analysis of propellers and helicopter rotors, although more elegant methods of analysis are available. The technique, which assumes local 2-D flow at each radial rotor station, is a design-analysis approach in which the airfoil sectional aerodynamics, chord and pitch angle are required in order to determine the forces and the torque.

It has been assumed that strip theory approaches will be adequate for wind machine performance analysis; however, experimental verification is sparse and clouded by the fact that the available test data has been taken in a Reynolds Number range for which the section aerodynamics are quite sensitive to free stream turbulence. One reason for the belief that strip theory is expected to give acceptable results is the fact that a wind turbine wake expands rather than contracts. At low advance ratios (high tip speed ratios), propellers and helicopter rotors have been observed to shed strong tip vortices. Since the wake is contracting, the position of this vortex in the wake is inboard of the tip and strong interaction occurs between the tip vortex and the flow in the plane of the blade. The resulting radial

distribution is found to be appreciably different than the force distributions predicted by strip theories. Because most wind turbines operate at high tip speed ratios, a strong interaction is expected; however, due to the expanding wake, the tip vortex moves outboard negating a strong interaction. From an outboard position in the wake, the tip vortex generates induced velocities that decrease the local angle of attack, in addition these velocities are of lower magnitude than for inboard vortex positions of a contracting wake.

Strip theory analysis requires some modification because of the pattern of shed vorticity, even in the absence of tip vortices. The shed vorticity interacts with the blade flow near the blade tip. So-called tip losses have been treated in a variety of approaches, the simplest of these being to reduce the maximum rotor radius to some fraction of the actual radius characteristically on the order of 97% of the actual radius. Prandtl and Goldstein have analyzed flow about lightly-loaded propellers (negligible wake contraction) and developed models for the reduction of circulation due to wake interaction at the tips.

The basic theoretical development of strip theory is presented in this chapter, along with the use of tip loss models and a comparison of results using different models.

2.1 AXIAL MOMENTUM THEORY

The function of a wind turbine is to extract energy from the air and to produce mechanical energy which later may be transformed into other forms of energy. Energy losses, in addition to the energy extracted, are attributed

to the rotational motion of the fluid that is imparted by the blades and frictional drag. As a first approximation to determine the maximum possible output of a wind turbine, the following assumptions are made:

1. Blades operate without frictional drag.
2. A slipstream that is well defined separates the flow passing through the rotor disc from that outside the disc.
3. The static pressure in and out of the slipstream far ahead of and behind the rotor are equal to the undisturbed free-stream static pressure ($p_2 = p_\infty$).
4. Thrust loading is uniform over the rotor disc.
5. No rotation is imparted to the flow by the disc.

Applying the momentum theorem to the control volume in Figure 2.1.1, where the upstream and downstream control volume planes are infinitely far removed from the turbine plane, one obtains:

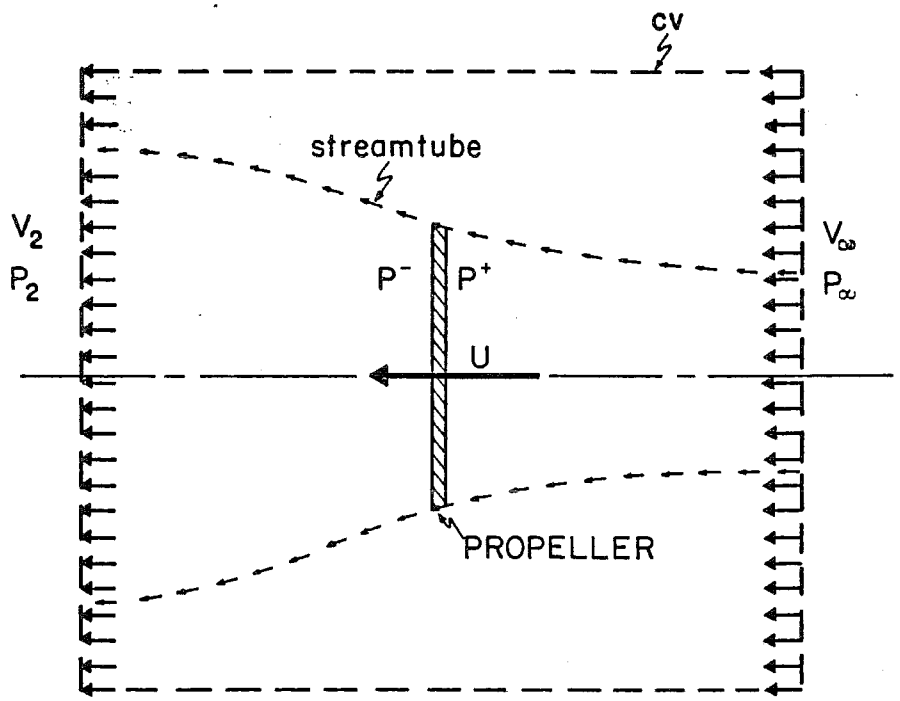

Figure 2.1.1. Control Volume of a Wind Turbine

$-T$ = Momentum flux out - momentum flux in

$$T = \dot{m}(V_\infty - V_2) = \rho AU\ (V_\infty - V_2) \tag{2.1.1}$$

Also from pressure conditions, the thrust can be expressed as:

$$T = A(p^+ - p^-) \tag{2.1.2}$$

Now applying Bernoulli's equation to flow upstream of the wind turbine, one obtains

$$\tfrac{1}{2}\rho V_\infty^2 + p_\infty = \tfrac{1}{2}\rho U^2 + p^+ \tag{2.1.3}$$

and downstream of the wind turbine,

$$\tfrac{1}{2}\rho V_2^2 + p_\infty = \tfrac{1}{2}\rho U^2 + p^- \tag{2.1.4}$$

or by subtracting these equations

$$p^+ - p^- = \tfrac{1}{2}\rho (V_\infty^2 - V_2^2)$$

Substituting into equation 2.1.2 gives

$$T = \tfrac{1}{2}\rho A(V_\infty^2 - V_2^2) \tag{2.1.5}$$

Now, equating equation 2.1.5 with 2.1.1 provides

$$\tfrac{1}{2}\rho A(V_\infty^2 - V_2^2) = \rho AV(V_\infty - V_2)$$

or

$$U = \frac{V_\infty + V_2}{2} \tag{2.1.6}$$

This result states that the velocity through the turbine is the average of the wind velocity ahead of the turbine and wake velocity aft of the turbine. Now defining the axial induction factor a by

$$U \equiv V_\infty\ (1-a)$$

and using the definition of a and equation 2.1.6 gives

$$V_\infty(1 - a) = \frac{V_\infty + V_2}{2}$$

then the wake velocity can be expressed as

$$V_2 = V_\infty(1 - 2a)$$

The wake induced velocity is twice that of the induced velocity in the plane of the rotor. This also may be concluded by constructing a system of helical vortices and calculating the induced velocity by utilizing the Biot - Savart relation. (see Section 2.10)

Therefore

$$a = 1 - \frac{V_\infty + V_2}{2V_\infty} \tag{2.1.7}$$

which implies that if the rotor absorbs all the energy, i.e., $V_2 = 0$, then a would have a maximum value of $\frac{1}{2}$. Because power is given by mass flow rate times the change in kinetic energy, the power, P, is

$$P = \dot{m}\Delta K.E. = \rho AU\left(\frac{V_\infty^2}{2} - \frac{V_2^2}{2}\right) = \tfrac{1}{2}\rho AV_\infty^3\, 4a(1 - a)^2$$

or

$$P = 2\rho AV_\infty^3 a(1 - a)^2 \tag{2.1.8}$$

Maximum power occurs when $\frac{dP}{da} = 0$

$$\frac{dP}{da} = 2\rho AV_\infty^3\,(1 - 4a + 3a^2) = 0$$

or

$$a = 1 \text{ or } 1/3$$

Maximum power occurs when $a = 1/3$ so

$$P_{max} = 16/27 \ (\tfrac{1}{2}\rho A V_{\infty}^{3})$$

The coefficient of power* equals approximately 0.593.

* $C_P \equiv \dfrac{\text{Power}}{\frac{1}{2}\rho A V_{\infty}^{3}}$

2.2 MOMENTUM THEORY FOR A ROTATING WAKE

The initial assumptions of axial momentum theory considered no rotation was imparted to the flow. It is possible to develop simple and useful relationships if we consider the angular velocity, ω, imparted to the slipstream flow to be small in magnitude when compared with the angular velocity, Ω, of the wind turbine rotor. This assumption maintains the approximation of axial momentum theory, that the pressure in the wake is equal to the free-stream pressure.

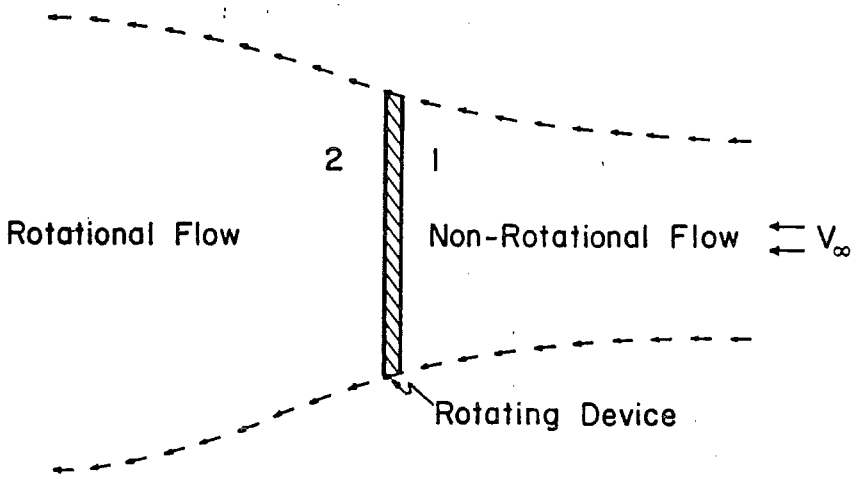

Figure 2.2.1. Flow Diagram of a Wind Turbine.

Writing the energy equation for the flow illustrated in Figure 2.2.1, it can be shown that the rotational kinetic energy reduces the power that can be extracted.

$$K.E._{translational_{(1)}} = \text{Power Extracted} + K.E._{translational_{(2)}} + K.E._{rotational_{(2)}}$$

The power is equal to the product of the torque acting on the rotor, Q, and the angular velocity of the rotor, Ω. In order to obtain maximum power it is necessary to have a high angular velocity and low torque because high torque will result in large wake rotational energy. An angular induction factor is defined as:

$$a' = \frac{\text{angular velocity of the wind at the rotor}}{\text{twice the angular velocity of the rotor}} = \frac{\omega}{2\Omega} \qquad (2.2.1)$$

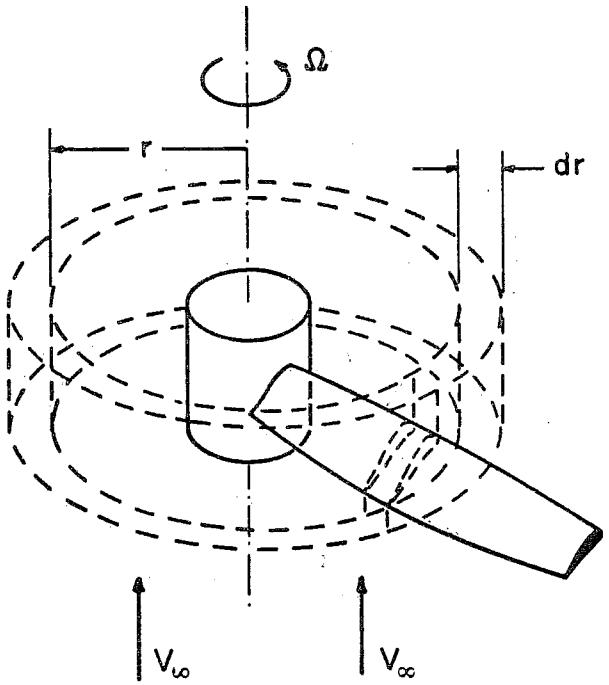

Figure 2.2.2 Rotor Blade Element

Using the angular ring in Figure 2.2.2, and writing control volume relations for momentum and moment of momentum, we obtain: (taking into account blade coning)

$$dT = \rho U 2\pi r_L dr_L (V_\infty - V_2)$$

where $r_L = r\cos\psi$

$dr_L = dr\cos\psi$

ψ = coning angle.

Assuming that

$$(V_\infty - V_2) = 2aV_\infty$$

$$dT = 4\pi r_L \rho V_\infty^2 a(1-a)\,dr_L \tag{2.2.2}$$

The moment of momentum equation becomes

$$dQ = d\dot{m}(V_t r) = 2\pi r_L \rho U r_L^2 \omega \, dr_L$$

$$= 4\pi r_L^3 \rho V_\infty (1-a) a' \Omega \, dr_L \tag{2.2.3}$$

As $dP = \Omega \, dQ$

$$P = \int_0^R \Omega \, dQ$$

Now, substituting equation (2.2.3) into the integral equation for power:

$$P = \int_0^{R\cos\psi} 4\pi\rho V_\infty \Omega^2 (1 - a) a' r_L^3 \, dr_L$$

defining $x_L \equiv \frac{r_L \Omega}{V_\infty}$ as the local tip speed ratio (2.2.4)

and $X_\psi \equiv \frac{R\Omega \cos\psi}{V_\infty}$ where R is the rotor radius (2.2.5)

we obtain

$$P = \rho A V_\infty^3 \frac{4\cos^2\phi}{X_\psi^2} \int_0^{X_\psi} (1 - a) a' x_L^3 dx_L \tag{2.2.6}$$

where $A = \pi R^2$. The coefficient of power becomes

$$C_p = \frac{8}{X_\psi^2} \cos^2\psi \int_0^{X_\psi} x_L^3 a'(1 - a) dx_L \qquad (2.2.7)$$

2.3 BLADE ELEMENT THEORY

By determining the forces acting on a differential element of the blade and then integrating over the length of the blade, torque and thrust loading of a rotor may be determined analytically. The fundamental assumptions are that there is no interference between successive blade elements along the blade and that the forces acting on a blade element are solely due to the lift and drag characteristics of the sectional profile of a blade element.

In an actual wind turbine, the blades may be made so that they cone. Without coning the force coefficients can be represented as shown in Figure 2.3.1 (ψ=0) and with coning as in Figure 2.3.1 ($\psi \neq 0$). Note that only the normal force coefficient is affected by coning.

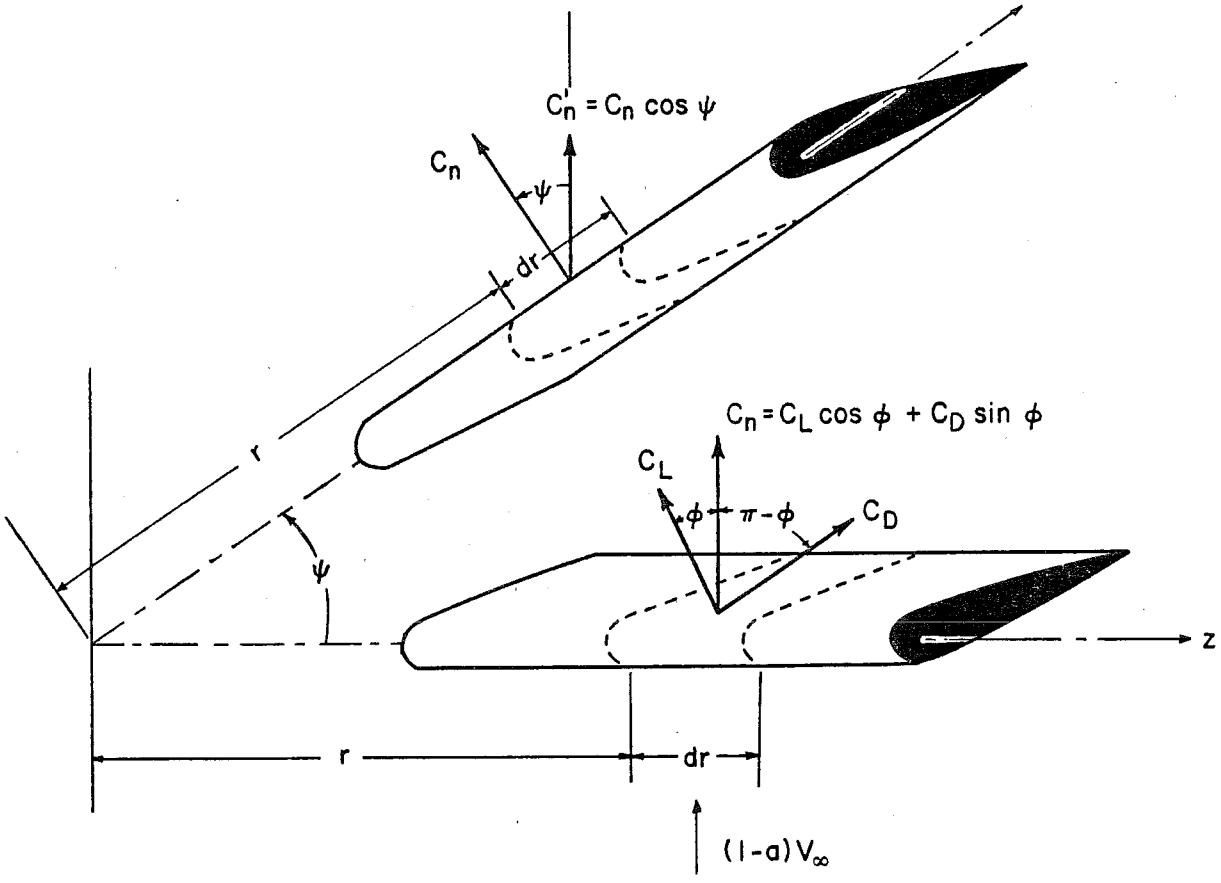

Figure 2.3.1 Blade Coning

The force coefficients in the coned position may be written as

$$C_n' = C_L \cos\phi \cos\psi + C_D \sin\phi \cos\psi$$

$$C_t = C_L \sin\phi - C_D \cos\phi$$

Also, the radial distance must include the effects of ψ. Thus

$$r_L = r \cos\psi$$

$$dr_L = dr \cos\psi$$

By using the velocities determined from the momentum theorem and applying them to the blade element, the velocity diagram, Figure 2.3.2 is obtained.

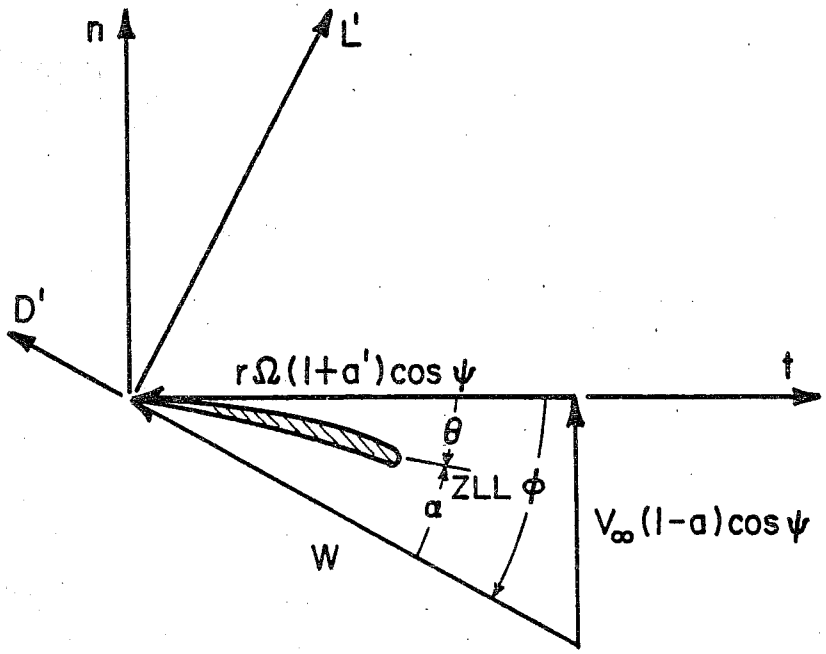

Figure 2.3.2 Velocity Diagram

From Figure 2.3.2, one can see that

$$\tan\phi = \frac{1-a}{1+a'} \frac{V_\infty \cos\psi}{r_L \Omega}$$

$$\alpha = \phi - \theta$$

$$C_n = (C_L \cos\phi + C_D \sin\phi)$$

$$C_n' = C_n \cos\psi$$

$$C_t = C_L \sin\phi - C_D \cos\phi$$

By determining the thrust acting on the blade element, one obtains

$$dT = Bc\tfrac{1}{2}\rho W^2 C_n' \frac{dr_L}{\cos\psi} \qquad (2.3.1)$$

where B = number of blades

c = chord

The torque acting on the blade element is given by the following expression

$$dQ_{\text{blade element}} = r_L Bc(\tfrac{1}{2}\rho W^2) C_t \frac{dr_L}{\cos\psi} \qquad (2.3.2)$$

2.4 STRIP THEORY

Utilizing both the Axial Momentum and Blade Element Theories, a series of relationships can be developed to determine the performance of a wind turbine.

By equating the thrust determined from the momentum theory equation (2.2.2) to equation (2.3.1), the thrust determined by blade element theory, one obtains for an annular element at radius r_L,

$$dT_{momentum} = dT_{blade\ element}$$

or

$$4\pi r_L \rho V_\infty^2 a(1-a)dr_L = Bc\tfrac{1}{2}\rho W^2 C_n' \frac{dr_L}{\cos\psi} \qquad (2.4.1)$$

so

$$(1-a)(2a) = \frac{\sigma_L}{4}\frac{W^2}{V_\infty^2}\frac{C_n'}{\cos\psi}$$

where

$$\sigma_L = \frac{Bc}{\pi r_L} \qquad (2.4.2)$$

and

$$\sigma_m = \frac{Bc}{\pi R\cos\psi} \qquad (2.4.3)$$

From Figure 2.3.2 one can write

$$\sin\phi = \frac{(1-a)V_\infty\cos\psi}{W}$$

substituting this expression into equation 2.4.1 for the relative velocity W

$$2a(1-a) = \frac{\sigma_L C_n' (1-a)^2 \cos^2\psi}{4 \sin^2\phi \cos\psi}$$

or

$$\frac{a}{1-a} = \frac{\sigma_L C_n \cos^2\psi}{8 \sin^2\phi} \qquad (2.4.4)$$

Expression (2.4.4) now relates the axial flow conditions to the blade element geometry. By considering the moment of momentum, we can likewise develop a relationship between the rotational flow and blade element forces.

Equating the angular momentum determined from the momentum theory, equation (2.2.3) with equation (2.3.2) of blade element theory one obtains

$$dQ_{\text{angular momentum}} = dQ_{\text{blade element}}$$

or

$$4\pi r_L^2 \rho V_\infty (1-a) a' \Omega \, r_L dr = r_L B c \rho \tfrac{1}{2} W^2 C_t \frac{dr}{\cos\psi}$$

or

$$\cos\psi V_\infty (1-a) 2a' \Omega \, r_L = \tfrac{1}{4}\sigma_L C_t W^2 \qquad (2.4.5)$$

From Figure 2.3.2

$$\sin\phi = \frac{(1-a)V_\infty \cos\psi}{W}$$

$$\cos\phi = (1+a')\frac{r_L \Omega}{W}$$

substituting into equation (2.4.5)

$$\frac{2a'}{1+a'} \sin\phi \cos\phi = \frac{\sigma_L C_t}{4}$$

or

$$\frac{a'}{1+a'} = \frac{\sigma_L C_t}{8 \sin\phi \cos\phi} \qquad (2.4.6)$$

Equations (2.4.4) and 2.4.6), which determine the axial and angular interference factors contain drag terms. It has been an assumption that the drag terms should be omitted in calculations of a and a' on the basis that the retarded air due to drag is confined to thin helical sheets in the wake and have little, if any, effects on the induced flows. Therefore C_n and C_t used in calculation of a and a' are redefined as

$$C_n'' = C_L \cos\phi$$

$$C_t'' = C_L \sin\phi$$

so Equation (2.4.4) becomes

$$\frac{a}{1-a} = \frac{\sigma_L C_L \cos^2\psi \cos\phi}{8 \sin^2\phi} \qquad (2.4.7)$$

and Equation (2.4.6) becomes

$$\frac{a'}{1+a'} = \frac{\sigma_L C_L}{8\cos\phi} \qquad (2.4.8)$$

By using the relations developed, a and a' can be determined for a given differential element by the following iteration process:

1. Assume a and a'
2. Calculate ϕ : $\phi = \tan^{-1}[(1-a)\cos\psi/(1+a')x]$
3. Calculate α : $\alpha = \phi - \theta$
4. Calculate C_L, C_D, C_t, C_n
5. Calculate a and a' ; equation (2.4.7) and equation (2.4.8)
6. Compare to previous values of a and a' if equal, stop
7. Go back to 2.

Having determined a and a' by the above iteration process, we also have calculated C_t and C_n. We can determine torque, thrust, and power from the following equations:

$$Q = \frac{\frac{1}{2}\rho V_\infty^2 \pi R^3 \cos\psi^3}{X_\psi^2} \int_0^{X_\psi} \sigma_m (W/V_\infty)^2 C_t \, x_L dx_L$$

$$T = \frac{\frac{1}{2}\rho V_\infty^2 \pi R^2 \cos^2\psi}{X_\psi} \int_0^{X_\psi} \sigma_m (W/V_\infty)^2 C_n \, dx_L$$

$$C_p = \frac{8}{X_\psi^2} \int_0^{X_\psi} x_L^3 a'(1-a) dx_L$$

The above equations do not include tip loss and blade interference effects. Modifications to account for these effects as well as defining sectional aerodynamics are necessary for a meaningful solution to the system of equations. These areas are developed in subsequent sections of this chapter.

2.5 MULTIPLE SOLUTIONS IN STRIP THEORY

The equations for the induction factors a and a' do not always have a single unique solution[17]. This can be illustrated by graphically examining the blade force and momentum terms in equation (2.4.1). If we defined a local force coefficient, C_{T_L}, as

$$C_{T_L} = \frac{dT}{\frac{1}{2}\rho V_\infty^2 2\pi r_L dr_L} \tag{2.5.1}$$

both sides of equation (2.4.1) may be expressed in dimensionless form. The momentum contribution becomes

$$C_{T_L}\Big)_{\text{momentum}} = 4a(1-a) \tag{2.5.2}$$

and the blade force contribution becomes

$$C_{T_L}\Big)_{\text{blade}} = \frac{\sigma_L C_n'' (1-a)^2}{2\sin^2\phi} \tag{2.5.3}$$

The momentum equation is seen to be parabolic while the blade equation depends on the relation between the lift coefficient and the angle of attack, the local solidity, and the tip speed ratio.

The equation for the blade force may be simplified considerably by neglecting the induced rotation. Then equation (2.5.3) becomes

$$C_{T_L}\Big)_{\text{blade}} = \frac{x\sigma_L C_L}{2}\sqrt{x^2+(1-a)^2} \tag{2.5.4}$$

where x is the local tip speed ratio $r_L\Omega/V_\infty$. Thus both equations may be expressed in the form

$$C_{T_L} = C_{T_L}(a)$$

The blade equation, of course, also requires specification of the blade configuration in terms of the parameters σ_L, x and $C_L(\alpha)$. For the case where $C_L = 2\pi\sin\alpha$, the blade equation becomes a straight line passing through the point $C_{T_L} = 0$, a = 1 when the pitch angle is zero. The slope of the blade equation depends upon the local solidity and the local tip speed ratio. There is then for $C_L = 2\pi\sin\alpha$, one and only one solution that satisfies both the momentum and blade equations.

For other lift coefficient variations, however, multiple solutions may occur. Figure 2.5.1 shows the momentum and blade force equations plotted in dimensionless form. It may be observed that the blade equation retains the general shape of the lift coefficient versus angle of attack curve. While only two lift coefficient variations are illustrated it is apparent that under some conditions there may be three valid solutions to the strip theory equations. Values of the axial induction factor a greater than 0.5 are not valid because such conditions imply a wake velocity which is negative.

Figures 2.5.2 through 2.5.4 show the effects of blade pitch angle, tip speed ratio and solidity on the blade force equations. Again, it is apparent that under some conditions three valid solutions exist to the strip theory equations. The method outlined in Section 2.4 will converge to either solution number one or solution number three but will not converge to the middle solution. The reason for the lack of numerical convergence for the middle solution is that when $\left(\frac{dC_{T_L}}{da}\right)_{\text{blade}} < \left(\frac{dC_{T_L}}{da}\right)_{\text{momentum}}$ the iteration

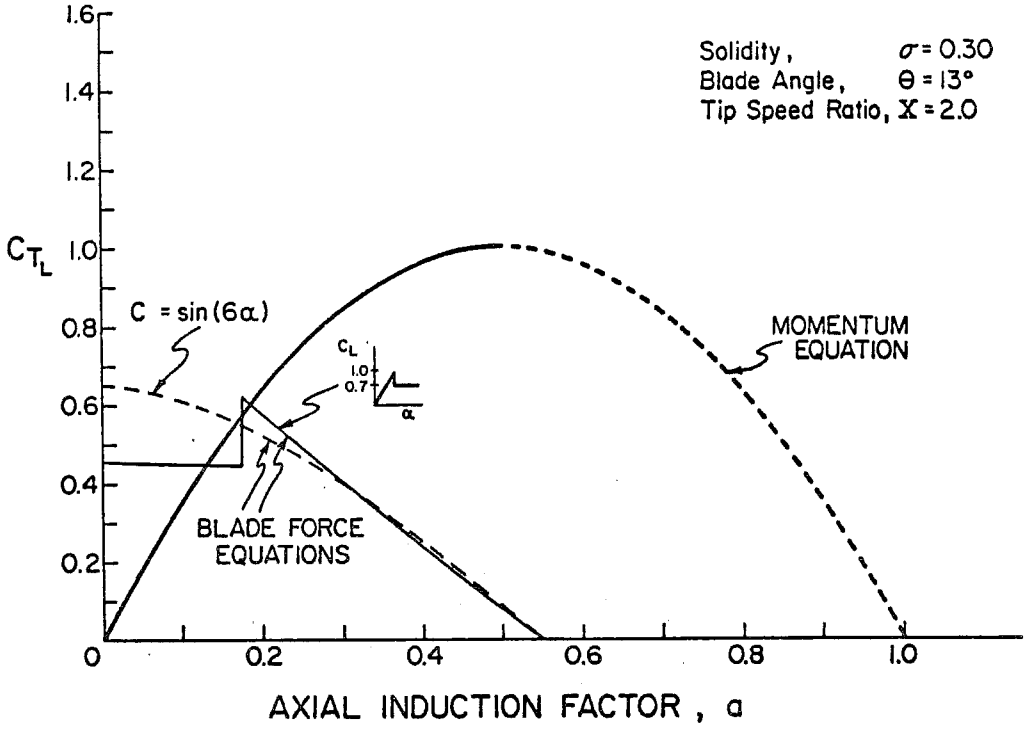

Figure 2.5.1 Dependence of Blade Force Equation on Lift Curve Characteristics

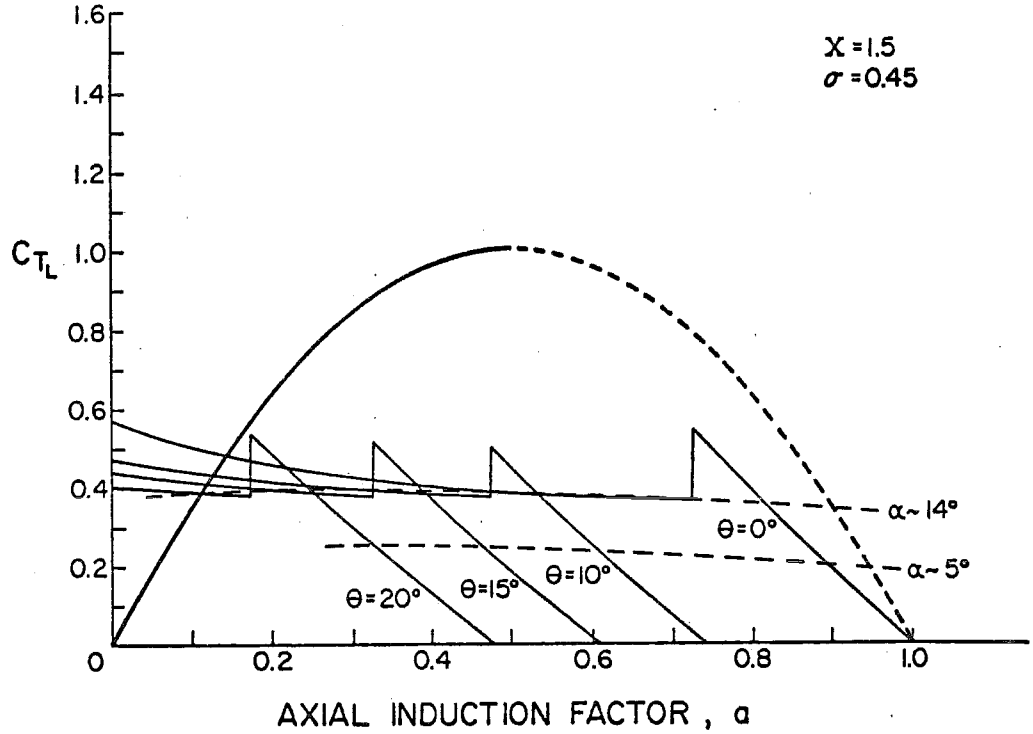

Figure 2.5.2 Effect of Blade Pitch Angle

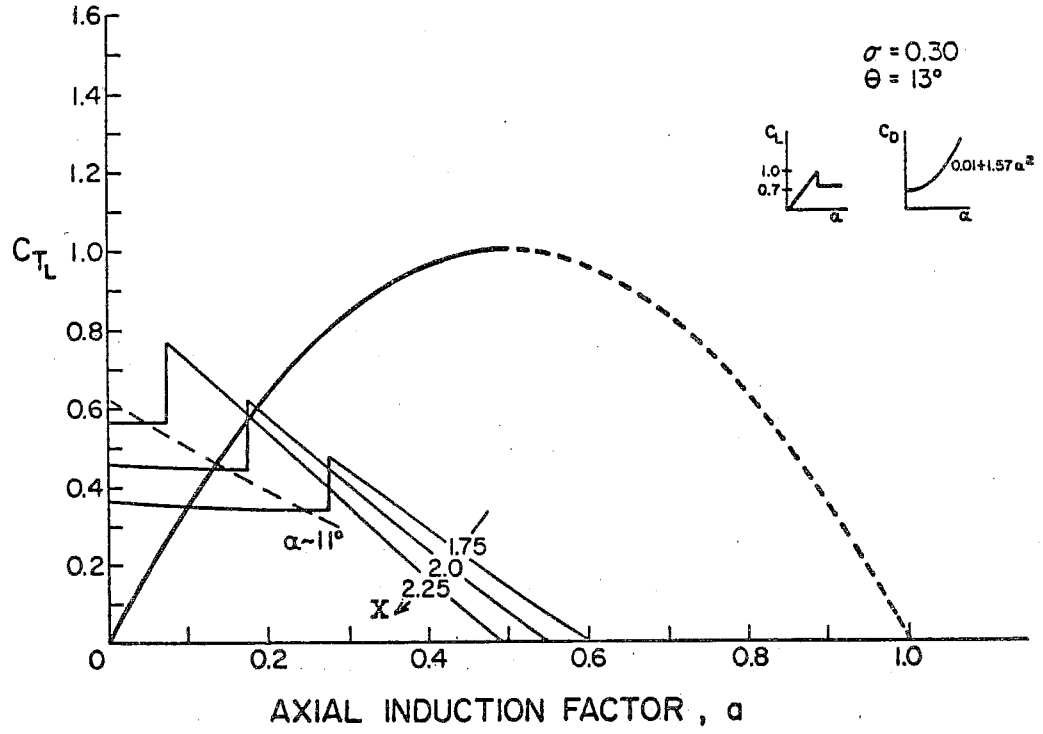

Figure 2.5.3 Effect of Local Tip Speed Ratio

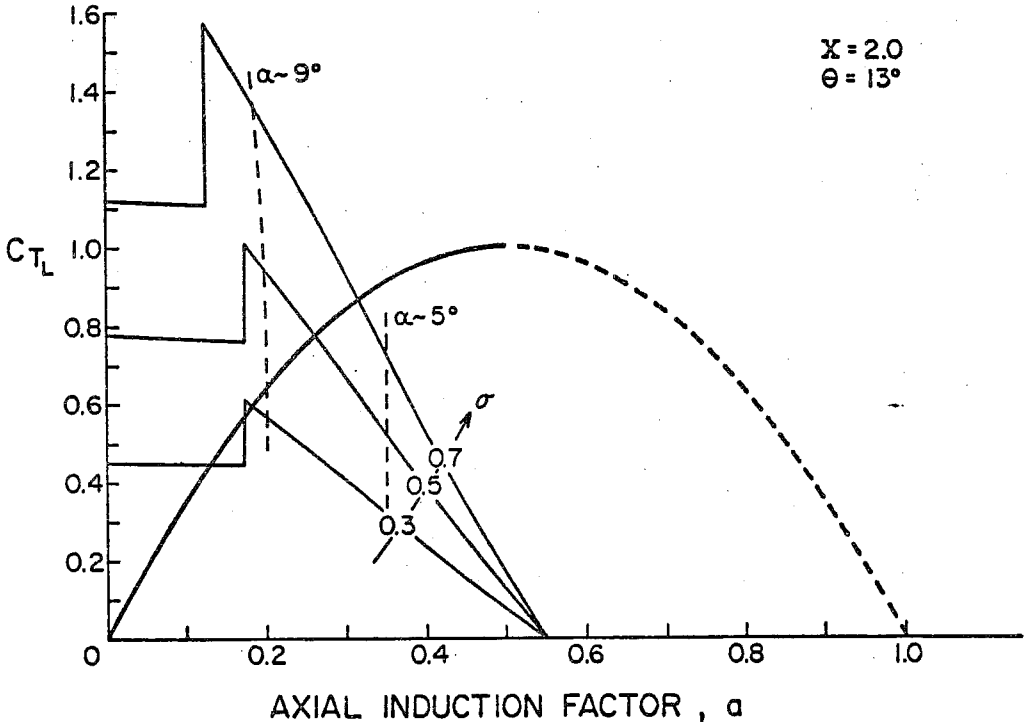

Figure 2.5.4 Effect of Local Solidity

converges, and when $\left.\frac{dC_{T_L}}{da}\right)_b > \left.\frac{dC_{T_L}}{da}\right)_m$, the iteration sequence diverges.

The lift curve selected is meant to be representative of a broad class of lift curves for which the lift has a sharp maximum and then levels off. While it is recognized that the numerous uncertainties make it improbable that performance test data can verify which other solutions occur (if any!) this discussion has been presented to enable performance and structural analysts to be aware of the multiple solutions possible in strip theory analysis.

As a guiding principle, it is suggested that the solution to be chosen in the case of multiple solutions is the one that maintains continuity of angle of attack along the blade span.

2.6 TIP LOSS CORRECTIONS

Strip theory, as previously developed, does not account for the interaction of shed vorticity with the blade flow near the blade tip. This "tip loss" or circulation reduction near the tip can be explained by the momentum theory. According to the theory discussed previously, the wind imparts a rotation to the rotor, thus dissipating some of its kinetic energy or velocity and creating a pressure difference between one side of the blade and the other. Because the pressure is greater on one side, air will flow around the blade tips as shown in Figure 2.6.1. This means that the circulation is reduced at the tip and as a consequence the torque is reduced.

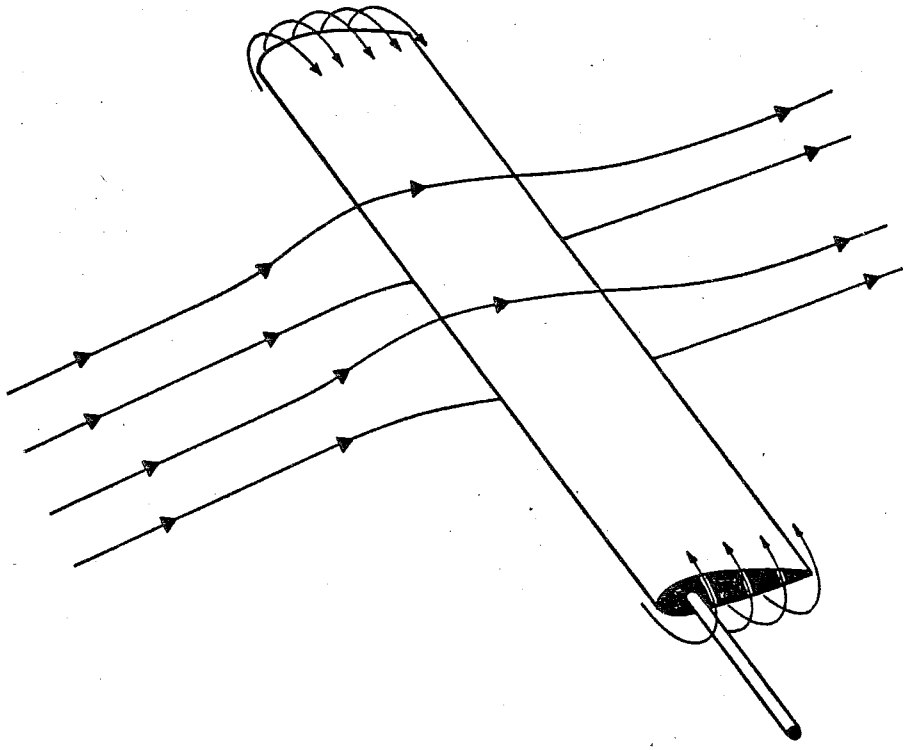

Figure 2.6.1 Tip and Hub Losses-Flow Diagram

Because the blade element forces at the tip contribute greatly to the torque and thus to the overall performance of the wind turbine, the tip flow is very important to the analysis. Tip losses have been treated in a variety of different manners in the propeller and helicopter rotor industry. The simplest method being to reduce the maximum rotor radius by some fraction of the actual radius, which in helicopter studies is of the order of 0.03R. Other relations have been developed that calculate this fraction of reduction based on the tip chord length. A more detailed analysis was done by Prandtl as a method for estimation of lightly loaded propeller tip losses. Later, Goldstein developed a more rigorous analysis. A comparison of the circulation distribution of a two-bladed propeller using the Prandtl and Goldstein methods is shown in Figure 2.6.2. Figure 2.6.3 shows numerical analysis of a wind turbine design using different tip loss models. As can be seen, there are substantial differences between methods and the application of these methods to wind turbines raises the question of which method is most accurate.

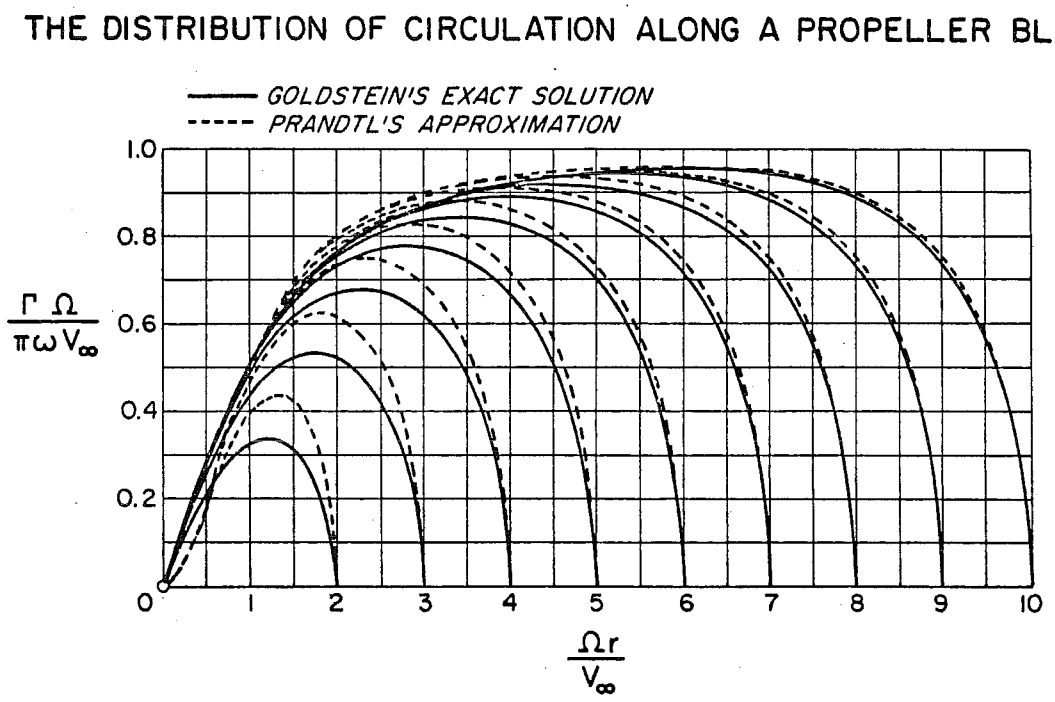

Figure 2.6.2 Circulation Distribution Along a Blade for a Two Bladed Propeller

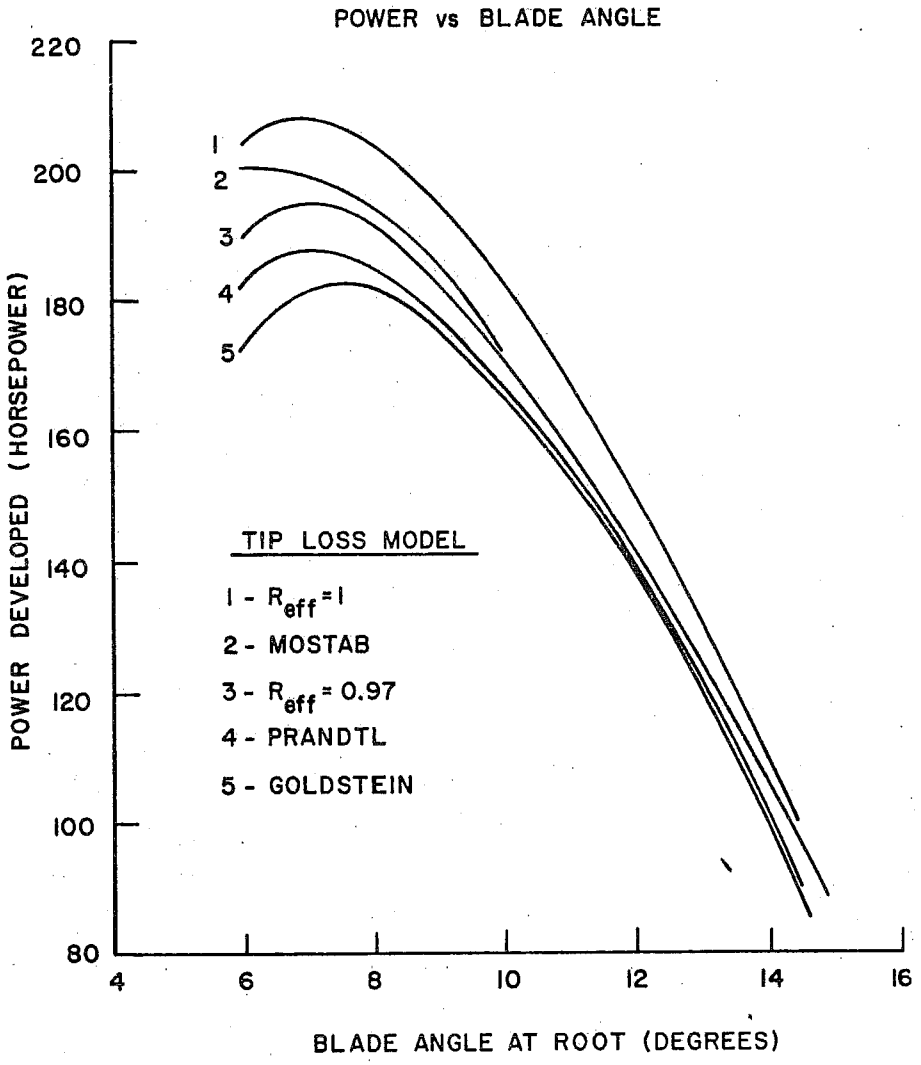

Figure 2.6.3 Performance Variation with Tip Loss Model.

Due to the lack of verification, the theoretical and computer analysis has options of either no tip loss, Prandtl's tip loss, Goldstein's tip loss or the effective radius concept of tip loss.

PRANDTL TIP LOSS FACTOR

L. Prandtl[10] developed a method to approximate the radial flow effect near the blade tip. The basis of his approximation was to replace the system of vortex sheets generated by the blade with a series of parallel planes at a uniform spacing, ℓ, where ℓ is the normal distance between successive vortex sheets at the slipstream boundary, or

$$\ell = \frac{2\pi R}{B} \sin \phi_T$$

Here B represents blade number and ϕ_T is the angle of the helical surface with the slipstream boundary. Thus, the flow around the edges of the vortex sheets could then be approximated as the flow around the edges of a system of parallel planes.

Prandtl's factor is defined as

$$F_p = \frac{2}{\pi} \text{arc cos } e^{-f}$$

where

$$f = \frac{B}{2} \frac{R-r}{R \sin \phi_T}$$

The expression for f can be suitably approximated by writing $r\sin\phi$ in place of $R\sin\phi_T$, because local angles of ϕ are more convenient in calculation procedures. Prandtl's approximation, as one can see from Figure 2.6.2, is sufficiently accurate for high tip speed ratios when the number of blades exceeds two. Of course, it should be remembered that the approximation was developed for a lightly loaded propeller (contraction negligible) and that the vortex system is a rigid helix, an optimum condition for propellers. Neither of these conditions are necessarily valid for wind turbines.

GOLDSTEIN TIP LOSS FACTOR

Goldstein[11] developed a more accurate analysis of tip loss for propellers by determining the circulation along the blade in terms of the induced velocity for a rotating blade. He also ignored contraction and utilized the rigid helix vortex representation. His solution was obtained by solving Laplace's equation with suitable boundary conditions.

Goldstein's tip loss factor is

$$K = \frac{1 + \mu^2}{\mu^2} \frac{r\Omega}{\pi\nu\omega}$$

where

Ω = angular velocity of rotor

r = local radius

R = maximum blade radius

ω = advance velocity of helical vortex surfaces

ν = velocity of advance

μ = local tip speed ratio

μ_o = tip speed ratio of rotor

Γ = bound circulation around the blade section

a_m = coefficient in Γ distribution

A_m = approximation coefficient to a_m's

ϵ_m = correction factor to approximation coefficient, A_m

$I_n(x)$ = modified Bessel function of 1st kind

$T_{1,n}(n)$ = modified Lomme function or Goldstein function defined in Ref. 11.

$$\frac{r\Omega}{\pi\nu\omega} = G(\mu) - \frac{2}{\pi} \sum_{m=o}^{\infty} \left(\frac{\mu_o^2}{1+\mu_o^2} A_m - \epsilon_m\right) \frac{I_{2m+1}(\overline{2m+1}\ \mu)}{I_{2m+1}(\overline{2m+1}\ \mu_o)}$$

$$G(\mu) = \frac{\mu^2}{1 + \mu^2} - \frac{8}{\pi^2} \sum_{m=0}^{\infty} \frac{F_{2m+1}(u)}{(2m+1)^2}$$

$$F_{2m+1}(u) = \frac{\mu^2}{1 + \mu^2} - T_{1,2m+1}\left(\overline{2m + 1}\ \mu\right)$$

As one can see from Figure 2.6.2, Goldstein's analysis should be used for the one and two-blade cases and for low tip speed ratios. A disadvantage of this method is the complexity of the solution which involves Bessel functions, but with the use of a digital computer and suitable approximations it can be easily handled.

EFFECTIVE RADIUS TIP LOSS CONCEPT

The tip loss model that has been used by NASA and the helicopter industry is one in which the rotor radius is reduced to an effective radius, R_e:

$$R_e = R \cdot B_o$$

where B_o is a constant (input) tip loss factor.
Then with R_e defined, radial integration proceeds inward from the tip, setting $C_L = 0$ at all integration steps greater than R_E. For specific integration around R_e, the integration step is changed to evaluate conditions at R_e and let $C_L = C_{L_F} * C_L$ at that station, where

$$C_{L_F}(R_e) = (R_e - r_k)/(r_{k+1} - r_k)$$

as shown in Figure 2.6.4.

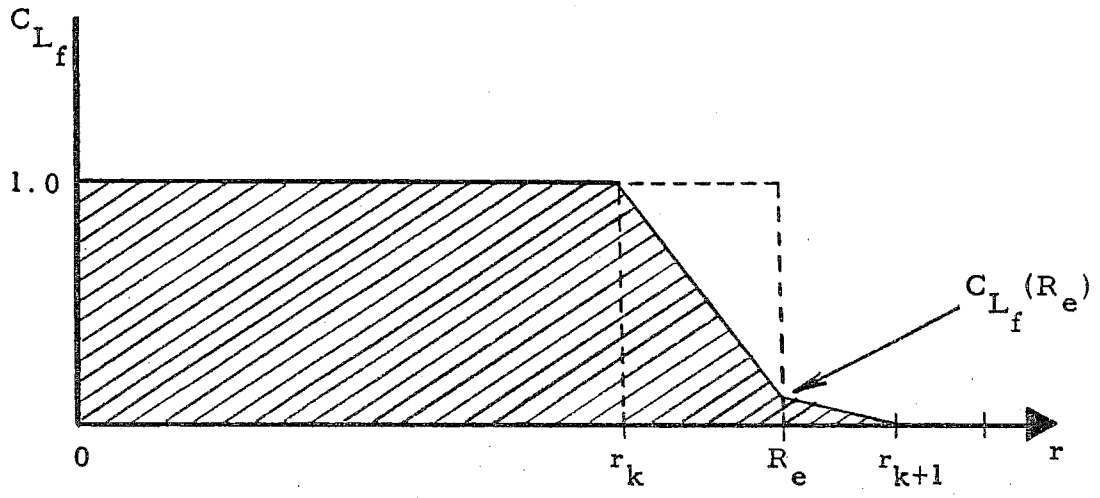

Figure 2.6.4 Variation Function for Lift Coefficient using Effective Radius Concept.

TIP LOSS FACTOR APPLICATION

The application of Prandtl's or Goldstein's tip loss factor to previous developed strip theory is of great importance. The tip correction represents physically the fact that the maximum decrease of axial velocity $2aV_\infty$ in the slipstream occurs at the vortex sheets and the average decrease is axial velocity in the slipstream is only a percentage of this velocity. Therefore equations (2.2.2) and (2.2.3) of axial momentum theory assume the forms:

$$\frac{dT}{dr} = 4\pi r\rho V_\infty^2(1-a)aF \qquad (2.2.2)$$

$$\frac{dQ}{dr} = 4\pi r^3\rho V_\infty\Omega(1-a)a'F \qquad (2.2.3)$$

In combination with blade element theory, equations (2.4.7) and (2.4.8) of general strip theory assume the forms:

$$\frac{a}{1-a} = \frac{\sigma_L C_L \cos^2\psi\cos\phi}{8F\sin^2\phi} \qquad (2.6.1)$$

$$\frac{a'}{1+a'} = \frac{\sigma_L C_L}{8F\cos\phi} \qquad (2.6.2)$$

Another application approach has been suggested by Wilson[18]. Since thrust is determined by

$$dT_{momentum} = dT_{blade\ element}$$

$$\rho U \Delta V 2\pi r_L\, dr_L = \frac{B}{2}\rho W^2 C_n'\, c dr_L$$

Consider the induced axial velocity to be localized at the rotor blade in a manner similar to the induced rotational velocity. Thus $U = (1-aF)V_\infty$ and $\Delta V = 2aFV_\infty$ so we obtain

$$(1 - aF)aF = \frac{\sigma_L C_L \cos\phi}{8\sin^2\phi}(1-a)^2 \equiv S(1-a)^2 \qquad \text{where } S \equiv \frac{\sigma_L C_L \cos\phi}{8\sin^2\phi}$$

then

$$a = \frac{2S + F - \sqrt{F^2 + 4SF(1 - F)}}{2(S + F^2)} \qquad (2.6.3)$$

and a' is as previously defined (2.5.2)

As $F \to 1$

$$a \to \frac{S}{1 + S}$$

whereas when $F \to 0$

$$a \to 1$$

Because there is uncertainty as to which approach most accurately corrects the basic strip theory, both methods are considered in the analysis. The first method discussed being referred to as the first order or standard method of tip-loss application and the second method suggested by Wilson as the second order method of tip loss application.

HUB LOSS (INNER BLADE TIP LOSS) EFFECTS

Another factor is the inner blade tip loss, when there is no hub. Prandtl's tip loss formula has been applied in the following way to account for this, and is considered sufficiently accurate for this purpose.

$$F = \frac{2}{\pi} \arccos e^{-f}$$

$$f = \frac{B}{2} \frac{r - r_{hub}}{r_{hub} \sin\phi}$$

where

r_{hub} = radius of hub

This is applied to the general strip theory by defining the tip loss factor as

$$F_{Total} = F_{Tip} * F_{Hub}$$

and applying either the first order or the second order method to the strip theory.

2.7 CASCADE THEORY

For high solidity wind turbines, it is necessary to account for flow blockage of the air as it passes through the turbine blades and also to account for the finite chord of the blade. The velocity of the air relative to the blade element is the resultant of the velocity through the wind turbine plane of rotation, $V_\infty(1-a)$, and a rotational component $\Omega r(1-a')$ as shown in Figure 2.2.2. If at a given radius of the turbine, r, the circumference can be unrolled and represented as a flat surface as shown in Figure 2.7.1. The blade elements are represented as a cascade of airfoils along an axis LL, where the distance between airfoils sections is $2\pi r/B$. The cascade of airfoil sections representing B blade elements of the turbine must be repeated to form an infinite cascade of airfoils.

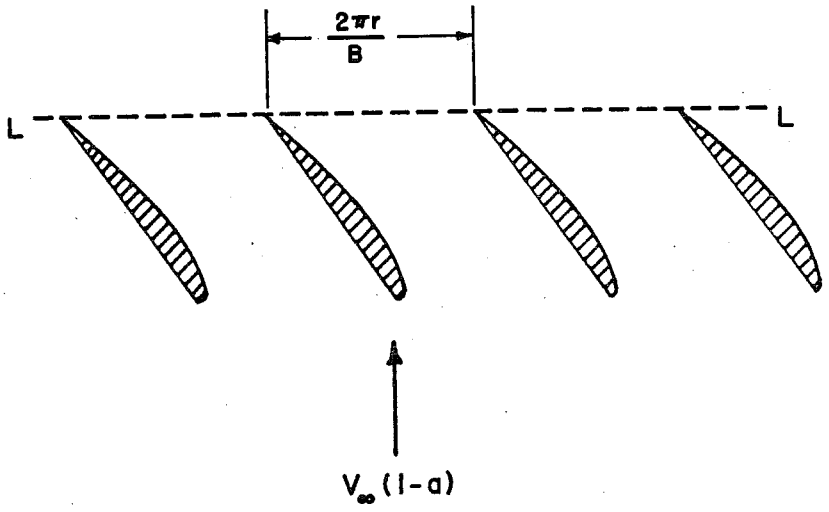

Figure 2.7.1 Cascade of Airfoil Sections

Immediately in front of the wind turbine, the effective axial velocity (Free stream velocity minus the axial induction velocity) and the rotational velocity define the velocity state as shown in Figure 2.7.2. As the flow enters the cascade of airfoils, the axial velocity must increase to satisfy continuity since the cross sectional area of the channel decreases. As the flow proceeds, the tangential component of induced velocity increases from zero at the leading edge to $(2a'\Omega r)$ at the trailing edge. As the flow passes the cascade, the tangential component of velocity remains unaltered, while the axial component must decrease again by continuity; because of this, the flow traces a curved path which effectively increases the camber of all sections.

The following assumptions are made as given by McCormick[19] for propellers:

1. The tangential velocity varies linearly from 0 at the leading edge to $2a'\Omega r$ at the trailing edge.
2. The flow angle θ is the slope of flow at any point at a distance y from the leading edge.

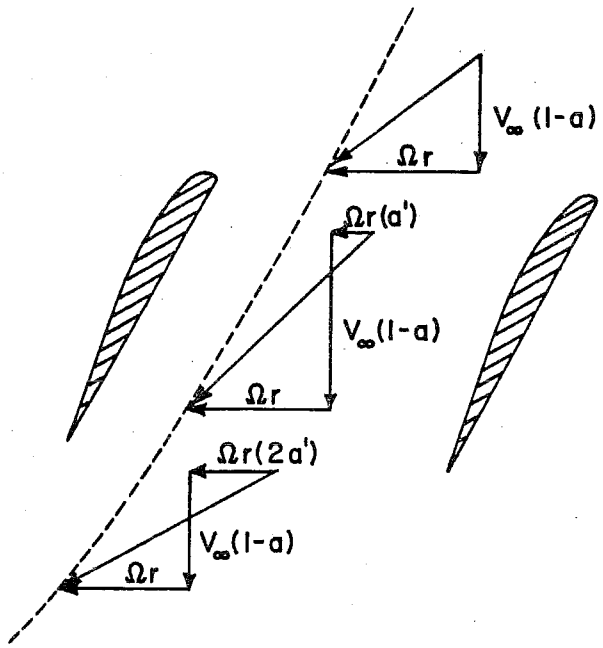

Figure 2.7.2 Flow geometry of a cascade of airfoil sections.

Therefore

$$\tan \theta = \frac{V_\infty(1-a)}{\Omega r(1+2 \frac{y}{c} a')} \tag{2.7.1}$$

and the change in θ from the leading edge to the trailing edge is

$$\Delta\theta = \tan^{-1} \frac{V_\infty(1-a)}{\Omega r(1+2a')} - \tan^{-1} \frac{V_\infty(1-a)}{\Omega r}$$

The effective change in the camber ratio become

$$\Delta\frac{z}{c} = \frac{\Delta\theta}{8} \tag{2.7.3}$$

For a circular arc airfoil, this corresponds to a reduction in the angle of attack of the zero lift line of

$$\Delta\alpha = \frac{\Delta\theta}{4} \tag{2.7.4}$$

EFFECT OF THICKNESS

To consider the effect of thickness, the airfoil can be approximated with an ellipse of the same thickness to chord ratio. Let us define:

$$t = t_{max} \left[2\left(\frac{y}{c/2}\right) - \left(\frac{y}{c/2}\right)^2\right]^{1/2} \tag{2.7.5}$$

$$\sigma = \frac{Bc}{\pi R}$$

$$x = r/R$$

$$X = \frac{R\Omega}{V_\infty}$$

y = distance from the leading edge

From continuity

$$2\pi r V_\infty = V(y)\ \{2\pi r - Bt_{max}[2(\frac{y}{c/2}) - (\frac{y}{c/2})^2]^{1/2}\} \qquad (2.7.6)$$

and

$$\theta = \tan^{-1}\frac{V(y)}{\omega r}$$

or

$$= \tan^{-1}\frac{1/X}{x\{1-\frac{\sigma t_{max}}{xc}[(\frac{y}{c})-(\frac{y}{c})^2]^{1/2}\}}$$

then

$$\frac{dz}{dy} = \theta - \tan^{-1}\frac{1}{Xx}$$

Integration gives

$$Z_{max} = \int_0^c (\theta-\tan^{-1}\frac{1}{Xx})\ dy$$

which leads to

$$\Delta\alpha = \frac{z_{max}}{c} = \int_0^1 (\theta-\tan^{-1}\frac{1}{Xx})\ d(\frac{y}{c})$$

or

$$\Delta\alpha = \frac{4}{15}\frac{\frac{1}{X}\sigma}{((\frac{1}{X})^2+x^2)}\ \frac{t_{max}}{c}$$

In performance calculations, the sectional angles of attack are reduced by the amounts given by expressions (2.7.4) and (2.7.7).

2.8 HIGH SOLIDITY WIND TURBINE ANALYSIS

The Chalk Wind Turbine invented by Thomas O. Chalk, marketed by the American Wind Turbine Company as the SST (Super Speed Turbine) and commonly referred to as the Bicycle Wheel Wind Turbine has been analyzed using the analysis previously discussed including the cascade corrections.

The design specifications used appear in Table 2.8.1. The sectional aerodynamics for the N60 airfoil were used because of the availability of low Reynolds Number data[20] and because of the great similarity of the N60 airfoil to the Clark Y airfoil. In addition, the analysis utilized a Prandtl-tip loss model.

TABLE 2.8.1

BICYCLE WHEEL WIND TURBINE SPECIFICATIONS

Outside diameter	-	15 ft. 3 in.
Inside diameter	-	5 ft. 3 in.
Length of blades	-	5 ft.
Number of blades	-	48
Chord of blades	-	3.475 in.
Blade pitch	-	9° outside rim, 18° inside rim } referenced to rotor plane
Blade twist	-	9°
Support wires	-	0.062 in diameter
Number of wires	-	not covered by blades = 96
Length of hub in axial direction	-	≈ 2 ft.
Airfoil	-	Clark Y

Figure 2.8.1 shows as plot of C_p versus tip speed ratio which is equivalent to a plot of power versus RPM at constant wind velocity. Figure 2.8.2 is a plot of C_p/X^3 versus $1/X$, which is equivalent to a graph of power versus wind-speed at constant RPM or Figure 2.8.3.

When the analysis was examined it was observed that the rapid decrease in power at high wind speeds is caused by aerodynamic stall and not by the drag of the wires, as originally conceived. At high tip speed ratios the windmill brake/vortex ring states are entered, a state of operation not covered by the analysis.

Preliminary experimental data obtained by Professor Dennis K. McLaughlin of Oklahoma State University is plotted in Figure 2.8.1.

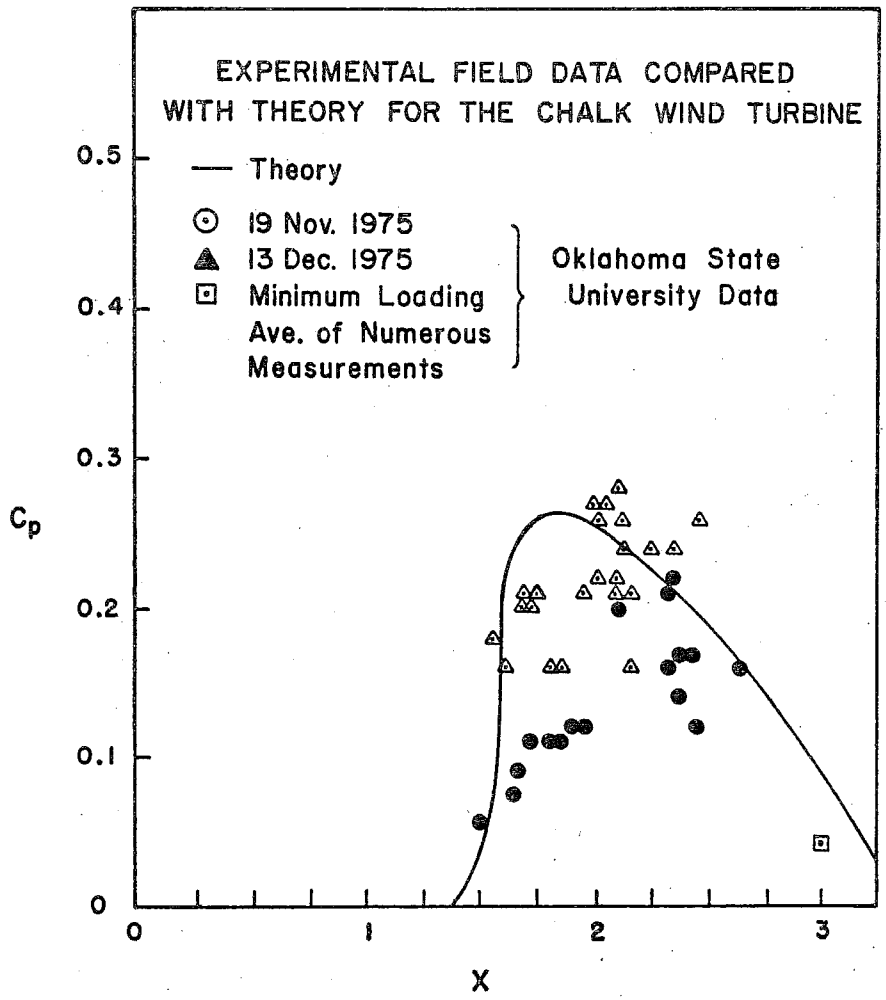

Figure 2.8.1 Power Coefficient versus Tip Speed Ratio for Chalk Wind Turbine

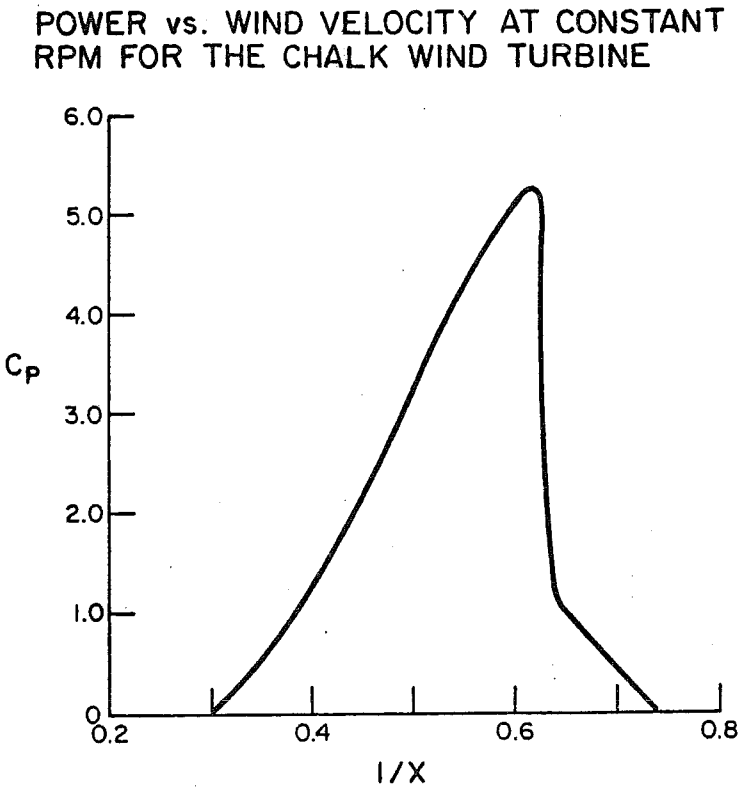

Figure 2.8.2 Power versus RPM at Constant Wind Velocity for the Chalk Wind Turbine

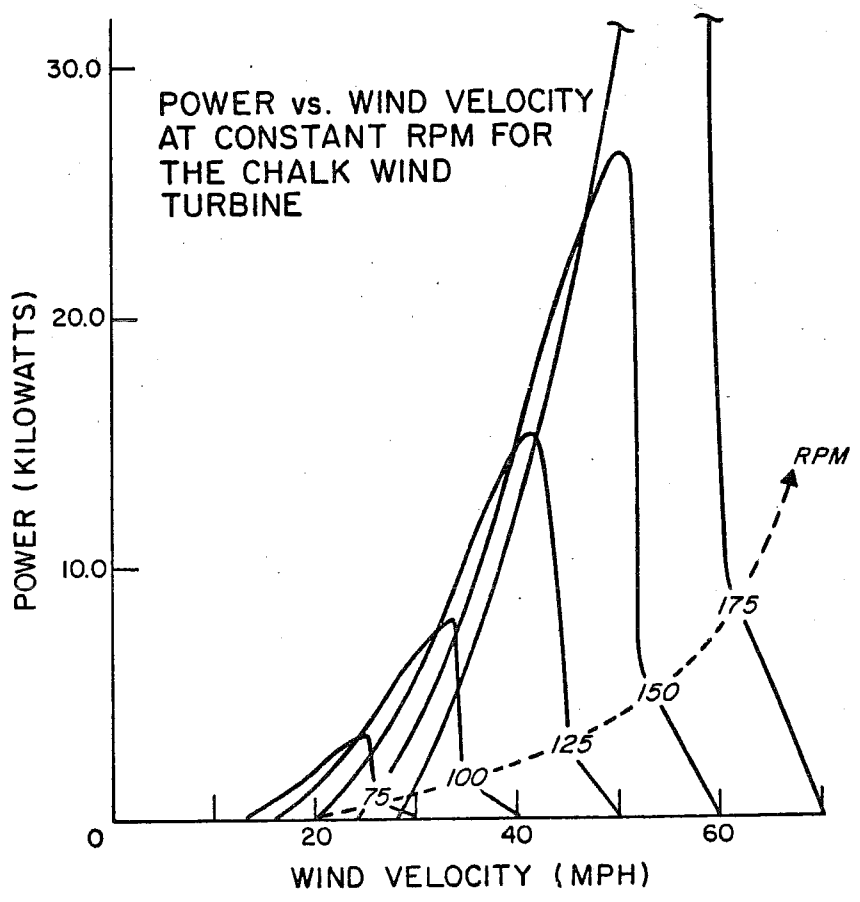

Figure 2.8.3 Power verus Wind Speed at Constant RPM

2.9 VORTEX RING/WINDMILL BRAKE STATE

The flow model developed by strip theory breaks down when the axial interference factor a exceeds 1/2*. This may be illustrated as shown in Figure 2.9.1 which shows the momentum equation and the blade element equations for zero drag and $C_L = 2\pi\sin\alpha$. The boundary between the momentum theory and vortex ring/windmill brake state can be expressed approximately by the relation

$$\theta \geq \frac{1}{2x} - \frac{r}{Bcx^2}$$

where $\theta \equiv$ ange of zero lift measured from the plane of rotation

$x \equiv$ local tip speed ratio, $\frac{r\Omega}{V_\infty}$

$r \equiv$ local radius

$c \equiv$ local chord

$B \equiv$ number of blades

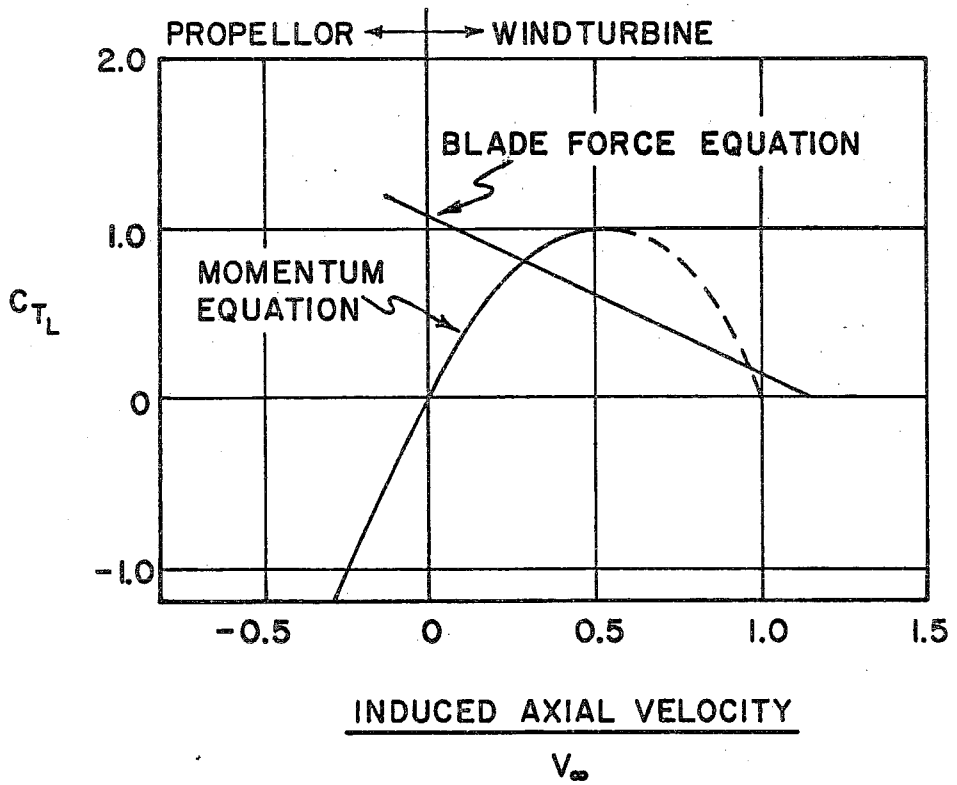

Figure 2.9.1 Graphic Display of Equations used in Strip Theory

* Actually when $(a\ F) \geq 1/2$.

The flow field for the vortex ring/windmill brake state for wind turbine has not been determined. The flow field is distinctively different, however, from the flow model of the strip theory model and the previous approach is not valid for this area of operation.

Empirical work done by H. Glauert[21] and others, redefined in terms of an average axial interference factor shows the deviation from momentum theory as shown in Figure 2.9.2 for the overall thrust coefficient, C_T.

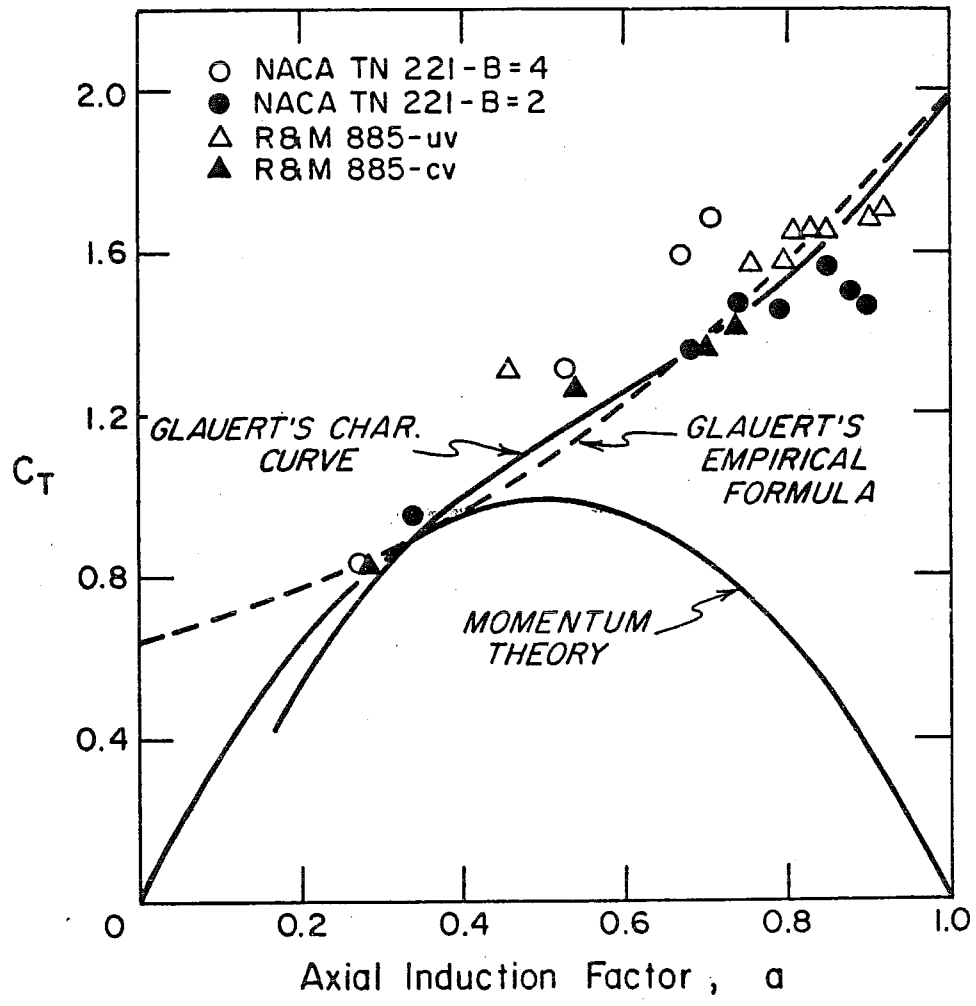

Figure 2.9.2 Windmill Brake State Performance

2.10 INDUCED VELOCITY VARIATION

The variation of the axial induced velocity with distance from the turbine plane is of importance in the placement of instruments to measure the true free stream wind velocity.

Calculation of this velocity may be accomplished by applying the Biot-Savart law to a vortex filament shed from the blade as it moves rearward in a helical manner (Figure 2.10.1).

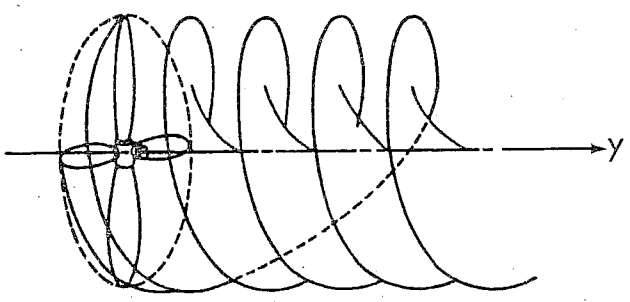

Figure 2.10.1 Rotor Wake Model

The axial velocity induced by a single helical vortex is shown in Figure 2.10.2.

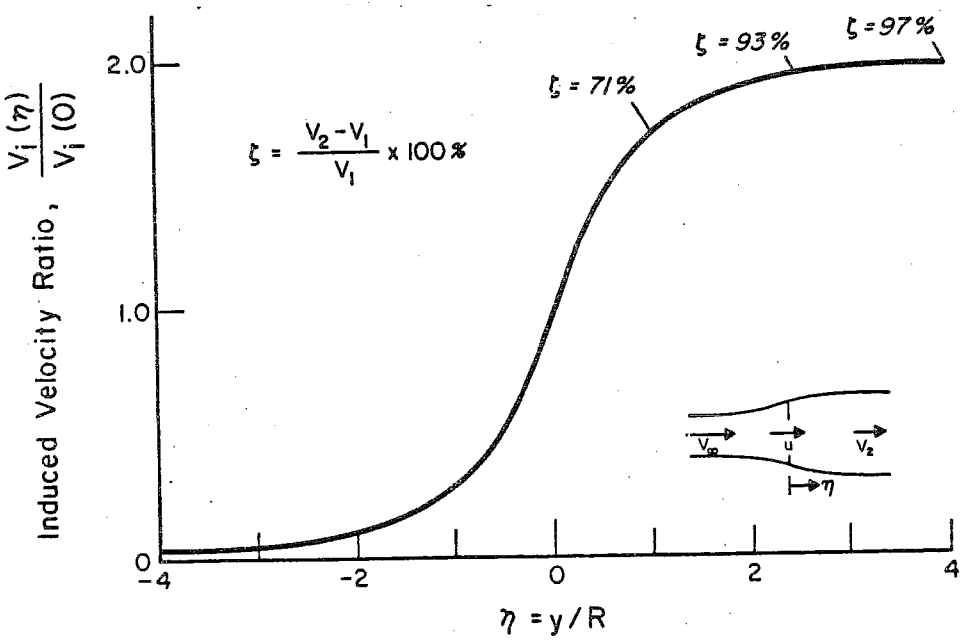

Figure 2.10.2 Induced Axial Velocity Variation

$$\frac{V_\infty - U(\eta)}{V_\infty - U(0)} = 1 + \frac{\eta}{\sqrt{1+\eta^2}}$$

REFERENCES

1. Rankine, W. J. M., Transactions, Institute of Naval Architects, Vol. 6, p. 13, 1865.

2. Froude, R. E., Transactions, Institute of Naval Architects, Vol. 30, p. 390, 1889.

3. Betz, A., Zeitshur.f. Flugtechnik u. Motorl. 11, 105, 1920.

4. Froude, W., Transactions, Institute of Naval Architects, Vol. 19, p. 47, 1878.

5. Drzewiecki, S., Bulletin del'Association Technique Maritime, 1892.

6. Lanchester, F. W., Aerodynamics, London, 1907.

7. Flamm, Die Schiffschraube, Berlin, 1909.

8. Joukowski, N. E., Soc. Math. Moscow, 1912, reprinted in "Theorie Tourbillonnaire de l'helice Propulsive," Paris, 1929.

9. Betz, A., Gottinger Nachr., p. 193, 1919.

10. Prandtl, L., Gottinger Nachr., p. 193 Appendix, 1919.

11. Goldstein, S., "On the Vortex Theory of Screw Propellers," Proc. Royal Soc. A123, 440, 1929.

12. Glauert, H., "An Aerodynamic Theory of the Airscrew," Reports and Memoranda, AE. 43, No. 786, January 1922.

13. Glauert, H., Br. A.R.C.R. and M. 869, 1922.

14. Glauert, H., Durand, W. F., (Ed.), "Airplane Propellers," Vol. IV, Division I, Chapter VII, Section 4, pp. 169-360, Julius Springer, Berlin, 1935.

15. Pistolesti, E., Vortrage aus dem Gebiete der Hydro-und Aerodynamik, Innsbruck, 1922.

16. Kawada, S., Tokyo Imperial University, Aero. Res. Inst., No. 14, 1926.

17. Barieau, R. E., Private Communication.

18. Wilson, Robert E. and Lissaman, Peter B. S., "Applied Aerodynamics of Wind Power Machines," Oregon State University, May 1974.

19. McCormick, B. W., Aerodynamics of V/Stol Flight, pp. 73-100, Academic Press, 1967.

20. Schmitz, F. W., "Aerodynamics of the Model Airplane, Part 1, Airfoil Measurements," N 70-39001, NTIS, November 1967.

21. Glauert, H., "The Analysis of Experimental Results in the Windmill Brake and Vortex Ring States of an Airscrew," Reports and Memoranda, No. 1026 AE. 222, February 1926.

CHAPTER III

OPTIMUM-PERFORMANCE OF HORIZONTAL AXIS WIND TURBINES

INTRODUCTION

It is desirable to know the maximum efficiency that can be obtained from a wind turbine as well as the configuration required to obtain such performance. The principal use of such knowledge is expected to be in the evaluation of design tradeoffs rather than in the construction of performance-optimized wind turbines. While propeller theory has provided the basis for design analysis of wind turbines, the criteria for optimum propeller performance leads to a different result than for optimum wind turbine performance.

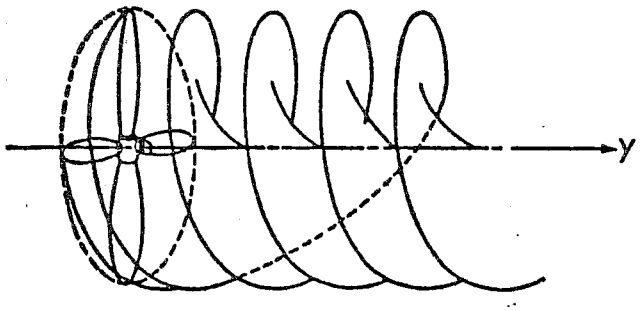

Figure 3.0.1 Helical wake model.

The optimum propeller was originally investigated by Betz[1] who proved that for maximum blade tractive power the far-wake must move rearward as a rigid helical surface as shown in Figure 3.0.1. The Betz condition for a lightly loaded rotor results in the requirement that the wake displacement velocity, v', illustrated in Figure 3.0.2, be constant along the blade.

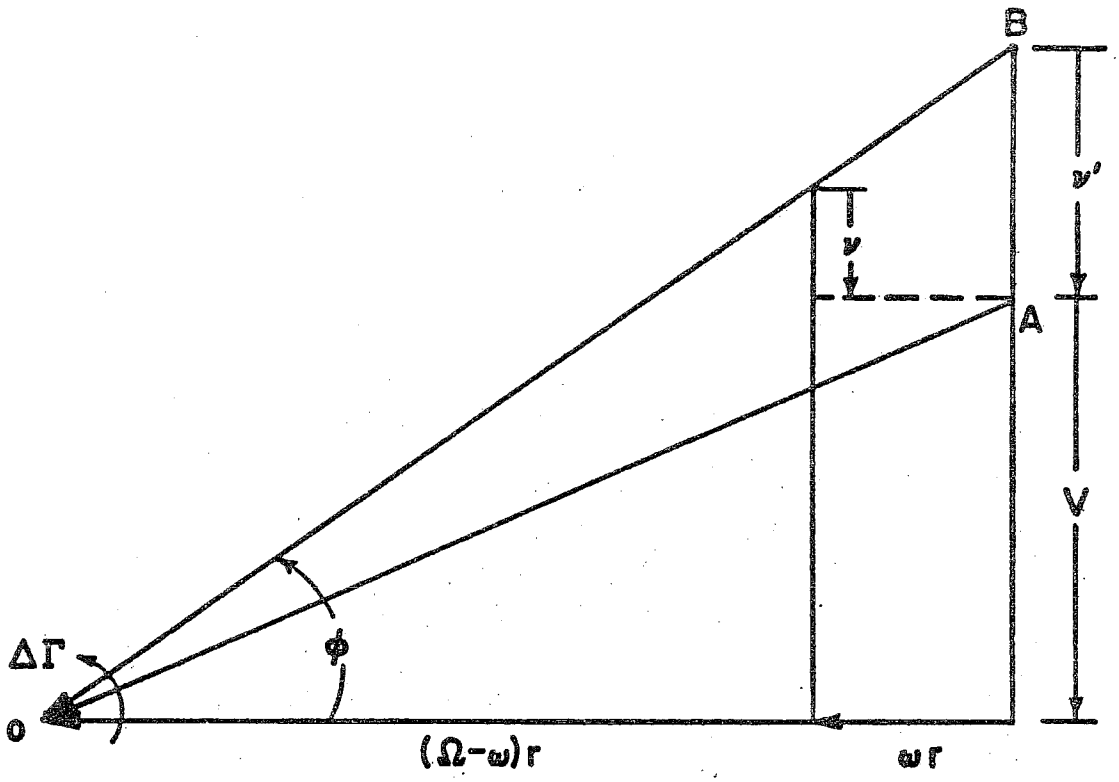

Figure 3.0.2 Wake flow velocity diagram for a propeller.

Goldstein[2] used the Betz rigid wake criteria to determine the exact distribution of circulation for a lightly-loaded propeller. Theodorsen[3,4,5,6,7] extended the Betz criteria to include heavy loading since the far wake has the same appearance regardless of the loading. By redefining Goldstein's solution for heavy loading and including wake contraction, Theodorsen developed a theory, for a specified power coefficient, that could be used to determine the wake displacement velocity; thereby, the optimum design configuration and optimum performance could be calculated. Crigler[8] presented Theodorsen's theory for the practical design of propellers, and later Lerbs[9,10] presented a refined approach, similar to Theodorsen's, for the design of marine propellers.

To define an optimum wind turbine, the relation between induced power and shaft power must be made stationary; while for the propeller, it is the expres-

sion relating maximum tractive power and shaft power which is to be held stationary. For a wind turbine, the efficiency depends on the ability of the wind to do useful work, UT, on the turbine and to convert that work into shaft power, ΩQ. Here Ω is the angular velocity of the turbine, Q the torque, T the axial force exerted by the wind, and U the axial velocity through the turbine. Just as is the case for the propeller, an increase in circulation for a wind turbine will result in an increase in torque ΔQ and axial force ΔT. This may be expressed as the ratio of power output increase to useful work increase λ,

$$\lambda = \frac{\Omega \Delta Q}{U \Delta T}$$

The procedure used for the propeller to establish that the efficiency is maximum does not yield the same result for the wind turbine because a change in circulation would not only change the axial force, T, and torque, Q, but also the axial velocity, U. However, it can be established that the induced tangential velocity for a wind turbine must be a minimum along the blade to obtain maximum performance. The flow field in the plane of the rotor is shown in Figure 3.0.3. The expressions for the axial force and torque increments due to an increment of circulation $\Delta\Gamma$ are expressible as

$$\Delta T = \rho \Delta\Gamma (\Omega + \frac{\omega}{2}) r dr$$

$$\Delta Q = \rho \Delta\Gamma (V - \nu) r dr$$

or $$\Delta Q = \rho \Delta\Gamma U r dr$$

Therefore,

$$\lambda = \frac{\Omega \Delta Q}{U \Delta T} = \frac{\Omega}{(\Omega + \frac{\omega}{2})}$$

or

$$\lambda = \frac{1}{(1+\frac{\omega}{2\Omega})} = \frac{1}{1+a'}$$

where $a' \equiv \frac{\omega}{2\Omega}$.

For a wind turbine we want λ to be large; therefore, the induced angular velocity must be a minimum along the blade. This condition leads to a variable wake displacement velocity as can be seen from Figure 3.0.3.

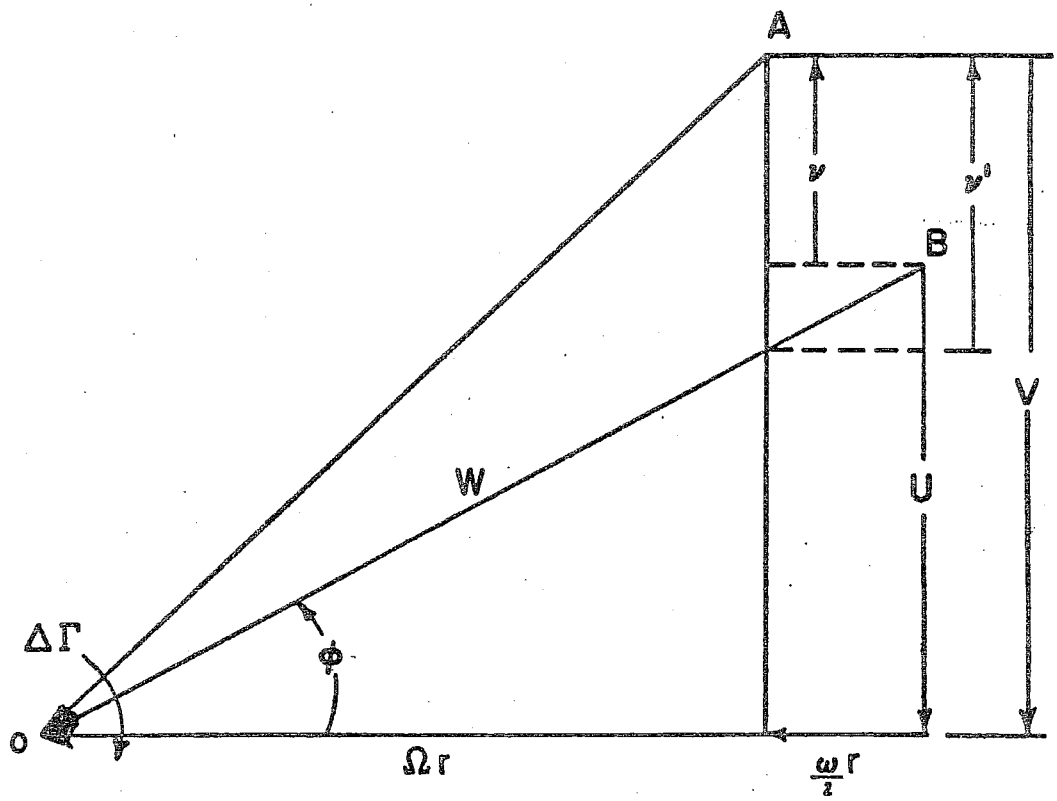

Figure 3.0.3 Rotor flow velocity diagram for a wind turbine.

Near the blade tips, at high tip speed ratios, the optimum wind turbine experiences a nearly constant wake displacement velocity; however, as the axis is approached, the displacement velocity increases. Therefore, it is apparent

that the wake vortex sheet will change shape with distance from the rotor, as shown in Figure 3.0.4. For this reason, the approaches of Goldstein, Theodorsen, and Lerbs cannot be used for wind turbines except for high tip-speed-ratio design, where errors in design specification at inner blade stations are not critical to performance.

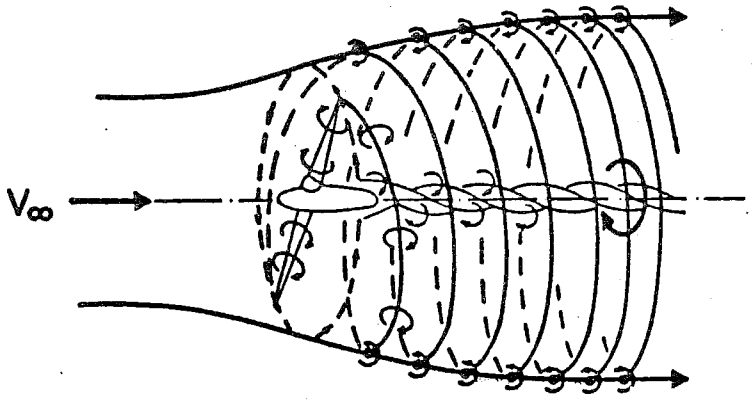

Figure 3.0.4 Vortex system of a wind turbine. The root displacement velocity is different than at tip.

Rohrbach and Worobel[11] have investigated the effect of blade number and section lift-to-drag ratio on the maximum performance that can be obtained from wind turbines. Figure 3.0.5 shows the effect of the section lift-to-drag ratio on peak performance of an optimum two-bladed wind turbine as obtained by Rohrbach and Worobel. Figure 3.0.6 shows the effect of blade number

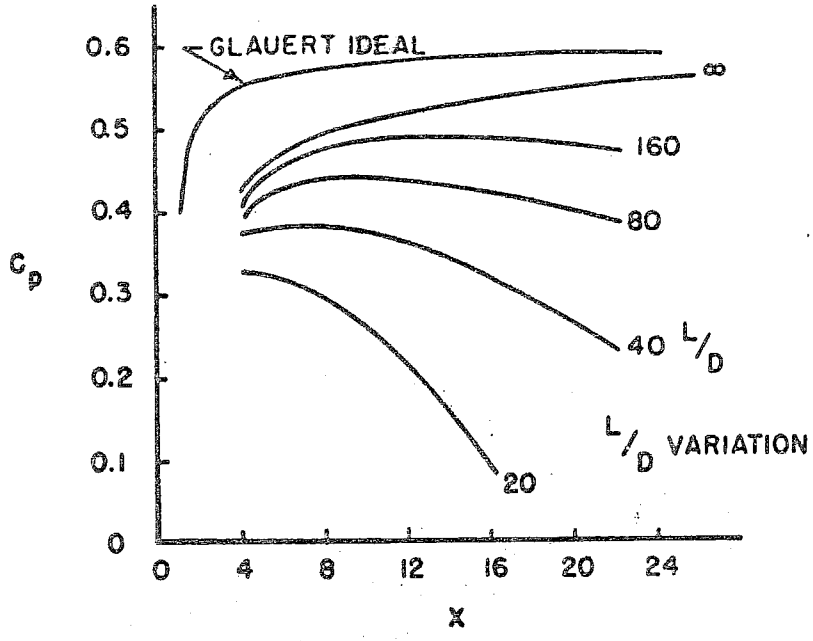

Figure 3.0.5 Effect of L/D on peak performance of optimum two-bladed wind turbines (Rohrbach and Worobel[11]).

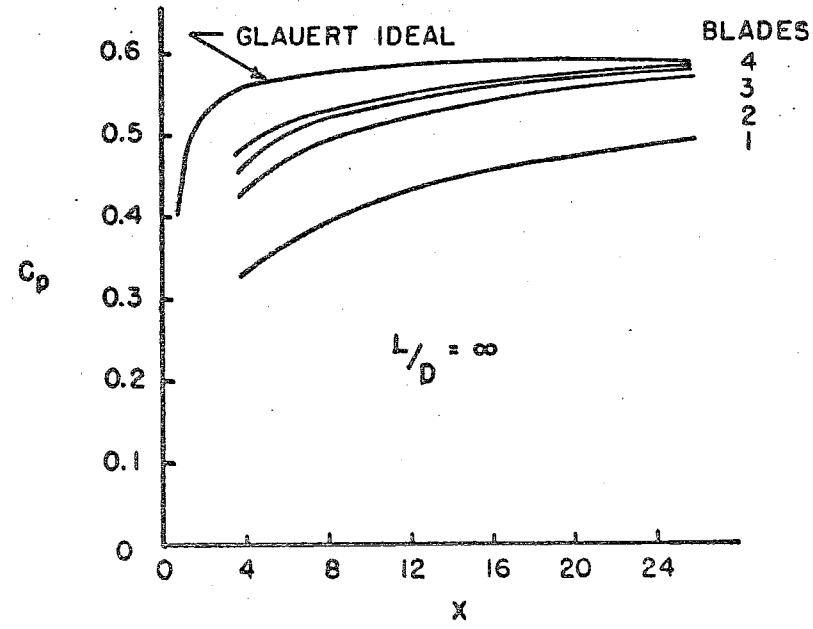

Figure 3.0.6 Effect of number of blades on peak performance of optimum wind turbines (Rohrbach and Worobel[11]).

on peak performance. The calculations of Rohrbach and Worobel have been found to yield slightly lower maximum performance than found in this study, the difference being attributed[16] to the fact that they used a finite hub radius.

Glauert[12] defined the configuration and performance of an optimum actuator disk by developing a closed-form solution to a variation problem using strip theory equations. Glauert's solution, however, neglected drag and tip-loss. This paper presents an approach using modified strip theory that incorporates tip-loss, determines the lift/drag effect on optimum performance, and examines the performance of optimum wind turbines at off-design conditions.

3.1 LOCAL OPTIMIZATION

Optimum performance may be determined by maximizing the power output at each station along the blade neglecting drag. The power developed at a differential element, dr, located at radial position, r, is

$$dP = \Omega dQ = \Omega r B c \frac{\rho}{2} W^2 C_t dr \qquad (3.1.1)$$

Defining local and overall tip-speed-ratios and solidity,

$$x = \frac{r\Omega}{V_\infty}, \quad X = \frac{R\Omega}{V_\infty}, \quad \text{and} \quad \sigma_L = \frac{Bc}{\pi r}$$

the local contribution to the power coefficient is given by

$$\frac{dC_p}{dx} = \sigma_L C_L \sin\phi \left(\frac{x}{X}\right)^2 \left(\frac{W}{V_\infty}\right)^2 \qquad (3.1.2)$$

where

$$C_p \equiv \frac{\text{Power}}{\frac{1}{2}\rho V_\infty^3 \pi R^2}$$

The differential contribution $\frac{dC_p}{dx}$ is maximized by varying the axial velocity, U, or its dimensionless equivalent, (1-a), until the power contribution becomes stationary. The equations for linear and angular momentum in the annular element must also be satisfied. From reference (13), the equation relating blade torque to the fluid angular momentum is

$$\frac{\sigma_L C_L}{8\cos\phi} = \frac{a'F}{1+a'} \tag{3.1.3}$$

The corresponding equation relating the blade force to the fluid linear momentum is

$$\frac{\sigma_L C_L \cos\phi}{8\sin^2\phi} = \frac{(1-aF)aF}{(1-a)^2} \tag{3.1.4}$$

Equation (3.1.4) contains a second order contribution from the tip-loss-factor. While experimental results for wind turbines are not sufficiently accurate to ascertain the validity of including the second-order term, the effect of retaining this term in the equations has resulted in significantly reduced numerical computation times in design optimization studies performed by Walker[14].

With the aid of the flow geometry at the blade illustrated in Figure 3.1.1, and Equation (3.1.3), the Equation (3.1.2) becomes

$$\frac{dC_p}{dx} = 8a'(1-a)F\,\frac{x^3}{X^2} \tag{3.1.5}$$

Equations (3.1.3) and (3.1.4) may be combined to give

$$a(1-aF) = a'x^2(1+a') \tag{3.1.6}$$

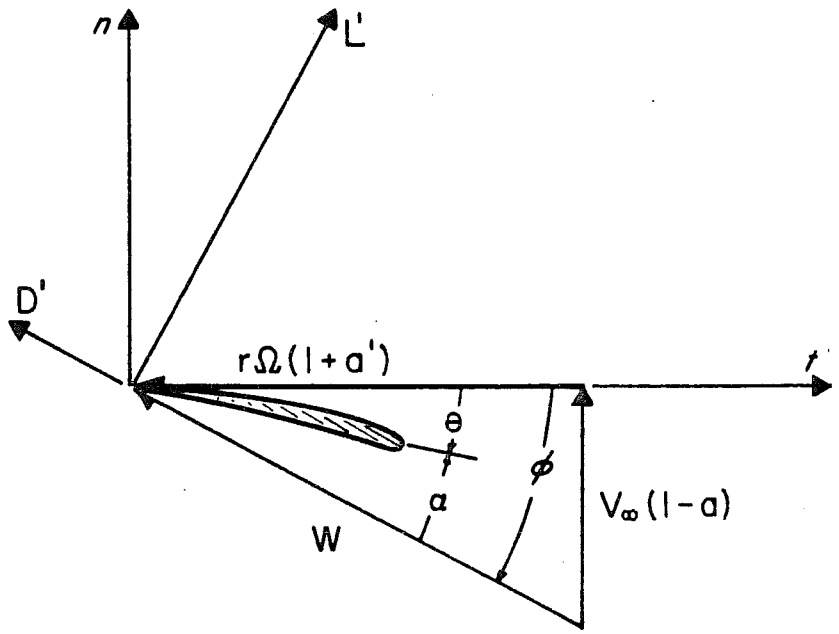

Figure 3.1.1 Blade flow velocity diagram.

The last two equations have been obtained using the assumption that only lift forces contribute to the induced velocities. It may be observed that if the tip-loss factor, F, is equal to unity, the above equations reduce to those of Glauert.

At each radial station, the power contribution is obtained by varying the axial interference factor, a, until Equation (3.1.5) is maximized. In the process of maximizing Equation (3.1.5), Equation (3.1.6) must also be satisfied. Additionally, F is a function of a, a', x and X. Therefore, for each trial value of a, iteration is required to obtain consistent values of a' and F.

As a result of optimizing the performance at each station, the flow angle, ϕ, and the product of cC_L are determined as a function of blade radius. The overall power coefficient is obtained by integrating the power coefficient contributions along the blade. The effect of drag can be determined parametrically by conducting multiple integrations for a range of blade section L/D ratios.

The blade twist is not determined by this process because the angle of attack depends upon C_L and only the product, cC_L, is available. It is necessary to specify either the chord distribution or the lift distribution to obtain the twist distribution.

3.2 OPTIMUM ROTOR CONFIGURATION AND PERFORMANCE

The parameters that determine the design point of a performance-optimized rotor are: blade number, tip speed ratio and the section L/D ratio. The effect of the L/D ratio on the induced velocities is small, well within the accuracy of experimental measurement. Hence, the rotor configuration was determined using the assumption of zero drag and the L/D ratio was then used to determine the effect of drag on rotor performance. The effect of each of the design parameters on optimum performance is:

1. Blade Number - the greater the blade number, the better the performance.
2. Tip Speed Ratio - higher tip speed ratios yield lower induced angular velocities; however, the drag effects also increase with increasing tip speeds. As a consequence, the power output at large tip-speed-ratios depends on the blade L/D ratio.
3. Lift-to-Drag Ratio - the higher the L/D ratio, the higher the performance independent of blade number or tip speed ratio.

In considering a wind turbine design, the question arises as to how many blades should be used. In general, as the number of blades increases so does the cost. The advantages of increasing the number of blades are improved performance and lower torque variations due to wind shear. Furthermore, power output increases, but with diminishing returns.

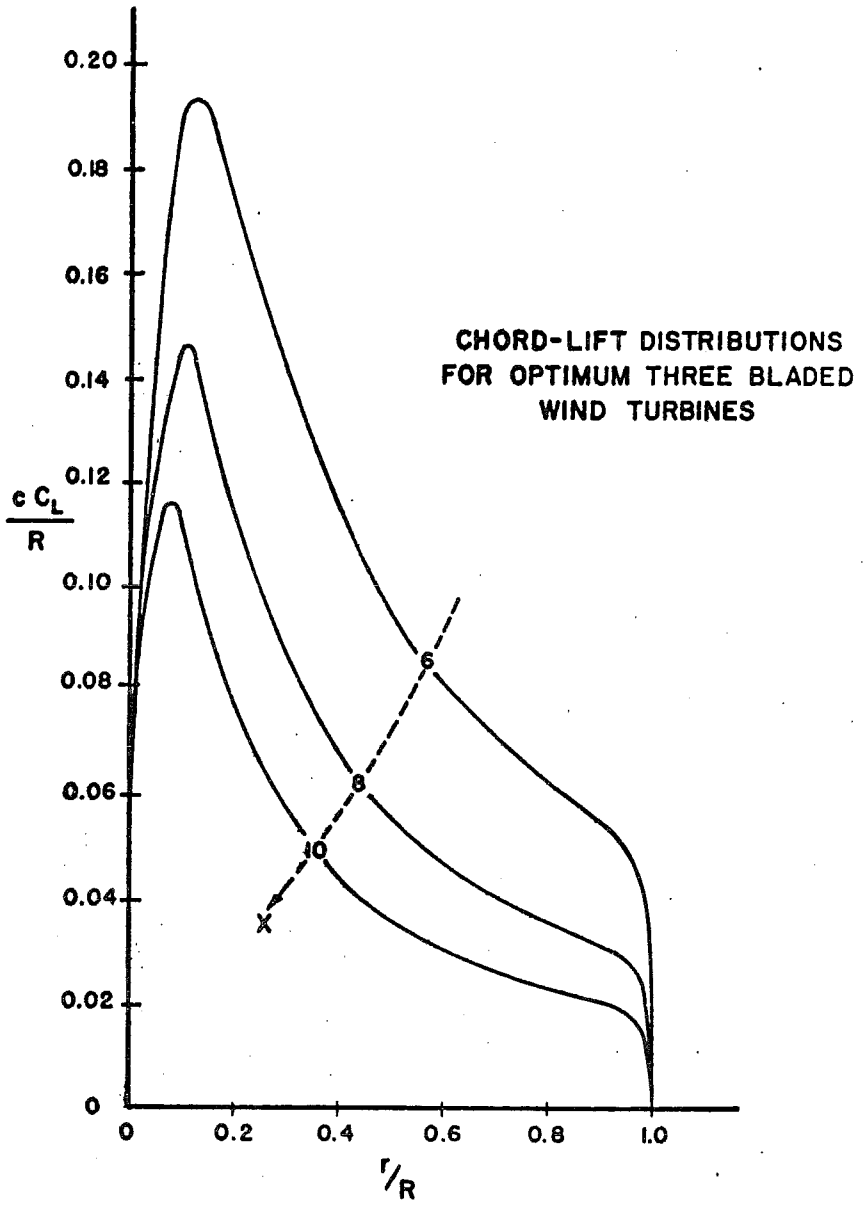

Figure 3.2.1 Blade chord-lift distributions for optimum performance three-bladed wind turbines.

The blade configuration for optimum performance requires that the blade width or chord and the blade twist angle vary continuously and in such a manner as to produce maximum power at a given tip speed ratio. As an example of a performance-optimized wind turbine, the blade chord and angle distributions

change are shown in Figure 3.2.1 and 3.2.2 for three-bladed machines. Note that as tip speed ratio increases, blade solidity and blade angle decrease.

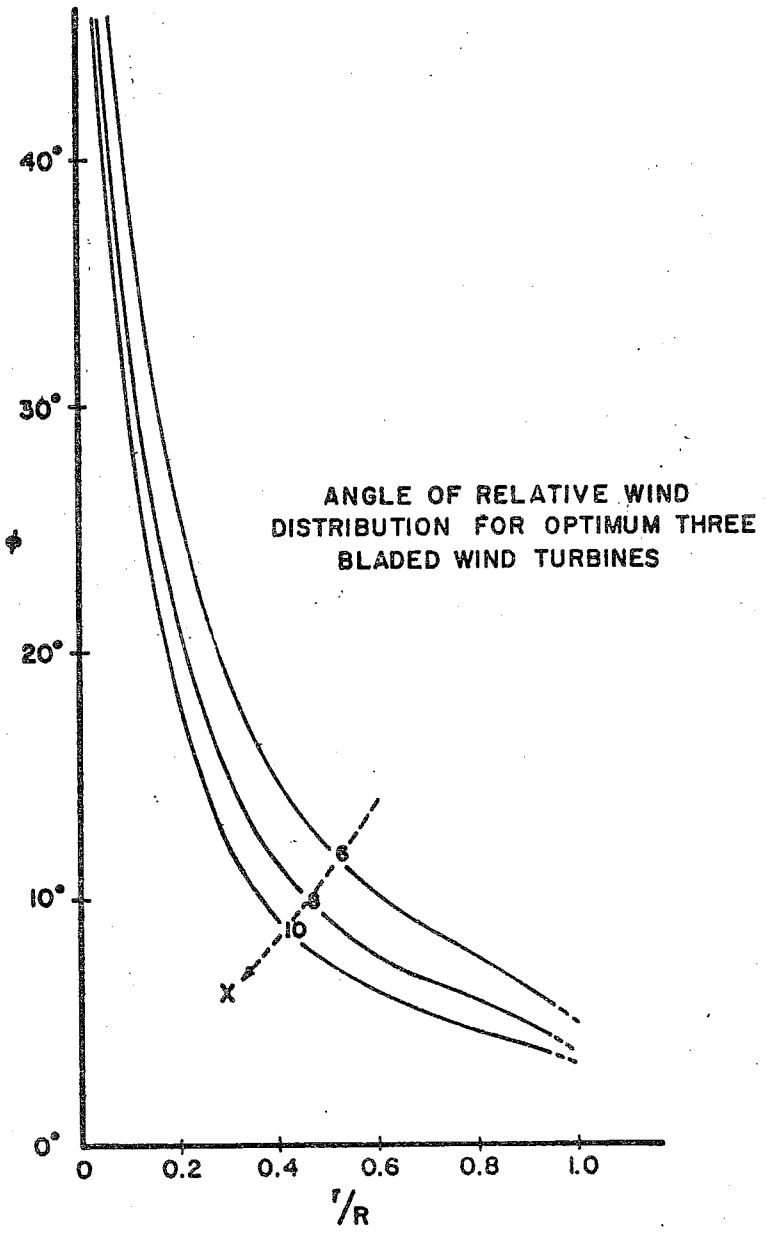

Figure 3.2.2 Angle of relative wind for optimum performance three-bladed wind turbines.

Table 3.2.1 presents the blade configuration for three-bladed optimum rotors at various tip speed ratios.

Table 3.2.1 Blade Geometry for Three-Bladed Wind Turbines

	X=6.0 $C_{P_{max}}$=0.535		X=8.0 $C_{P_{max}}$=0.548		X=10.0 $C_{P_{max}}$=0.555	
r/R	$\frac{cC_L}{R}$	ϕ	$\frac{cC_L}{R}$	ϕ	$\frac{cC_L}{R}$	ϕ
1.00	0.0000	5.000	0.0000	4.000	0.0000	3.200
0.95	0.0498	5.736	0.0290	4.468	0.0189	3.668
0.90	0.0550	6.524	0.0316	5.036	0.0204	4.099
0.85	0.0589	7.129	0.0337	5.464	0.0217	4.422
0.80	0.0627	7.690	0.0358	5.866	0.0230	4.730
0.75	0.0667	8.261	0.0381	6.282	0.0245	5.055
0.70	0.0711	8.875	0.0407	6.737	0.0262	5.417
0.65	0.0761	9.556	0.0436	7.251	0.0282	5.830
0.60	0.0818	10.331	0.0471	7.843	0.0304	6.308
0.55	0.0884	11.229	0.0510	8.535	0.0331	6.870
0.50	0.0960	12.284	0.0557	9.357	0.0362	7.540
0.45	0.1049	13.546	0.0613	10.349	0.0400	8.353
0.40	0.1154	15.078	0.0681	11.569	0.0446	9.357
0.35	0.1278	16.975	0.0763	13.103	0.0503	10.630
0.30	0.1423	19.369	0.0865	15.080	0.0576	12.290
0.25	0.1589	22.460	0.0993	17.710	0.0670	14.534
0.20	0.1765	26.535	0.1148	21.337	0.0794	17.710
0.15	0.1911	32.001	0.1324	26.537	0.0953	22.460
0.10	0.1900	39.355	0.1452	34.207	0.1123	29.995
0.05	0.1446	48.590	0.1263	45.172	0.1091	42.254

In order to specify blade configuration, it is not sufficient to examine the turbine performance at only the design condition; off-design operation must also be considered. Figure 3.2.3 illustrates the off-design-tip-speed-ratio performance of two rotors. Figures 3.2.4 and 3.2.5 illustrate the off-design blade pitch effects on performance. As can be seen, small changes in pitch angles have pronounced effects on off-design performance and delay entrance into the windmill-brake flow state. One may also observe from Figure 3.2.4

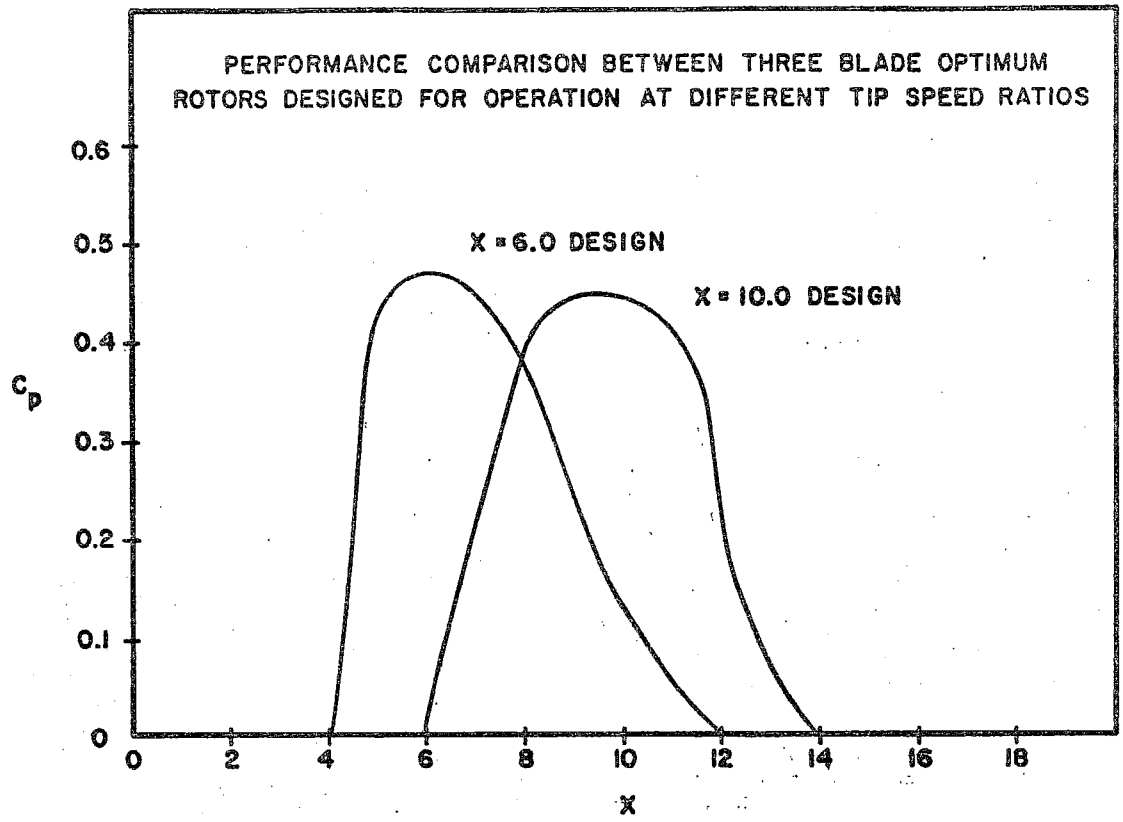

Figure 3.2.3 Off-design tip speed ratio performance of optimum performance three-bladed wind turbines, designed to operate at tip speed ratios of six and ten. (L/D = 55, C_L = 0.9 at all stations, NACA 23018 airfoil series.)

that for a design tip speed ratio of ten, pitching the blade in either direction from the design blade setting, 0°, produces a smaller power coefficient, signifying an optimum condition as expected. However, we observe that at a slightly lower tip speed ratio than the design tip-speed ratio (X = 10.0), performance is higher. This may be explained by Figure 3.2.6 which shows that for L/D ranges of 50-75, the power coefficient increases slightly as the tip speed ratio decreases from ten.

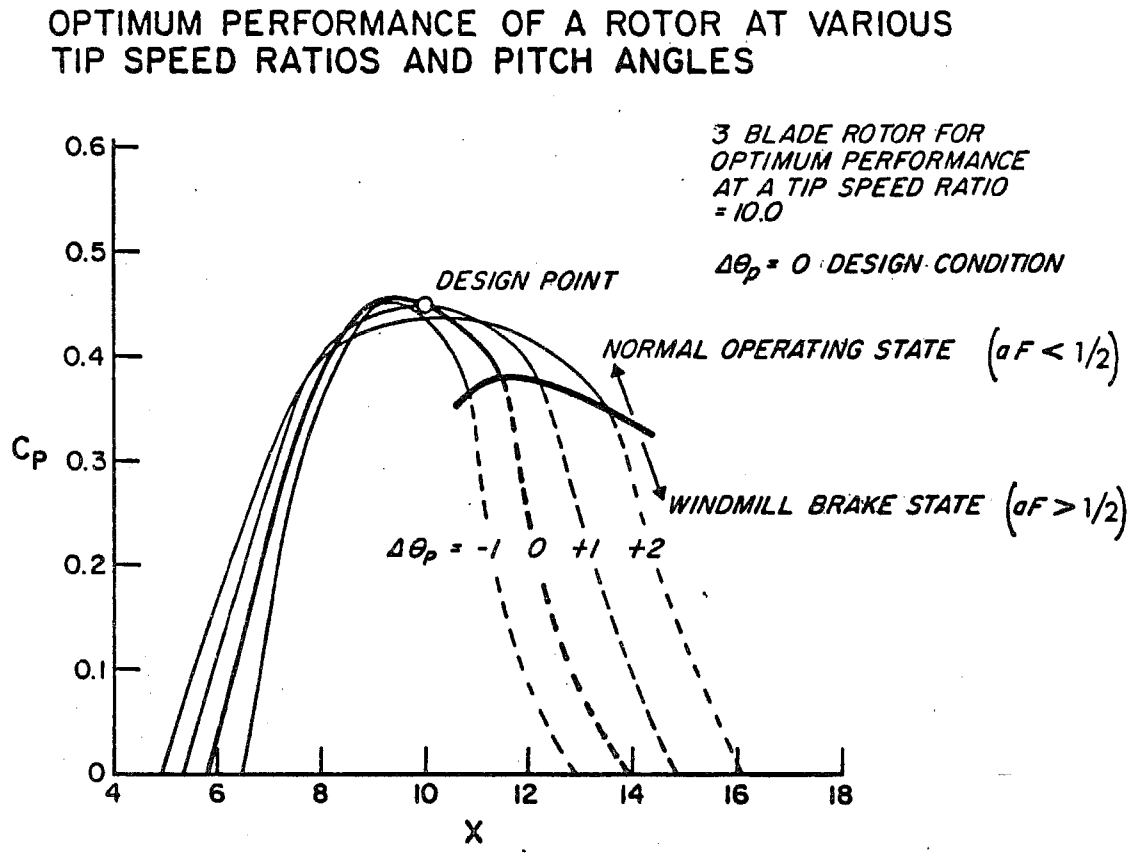

Figure 3.2.4 Blade pitch effects on an optimum performance three-bladed turbine (X_{design} = 10.0, L/D ≅ 55, C_L = 0.9 at all stations, NACA 23018 airfoil series).

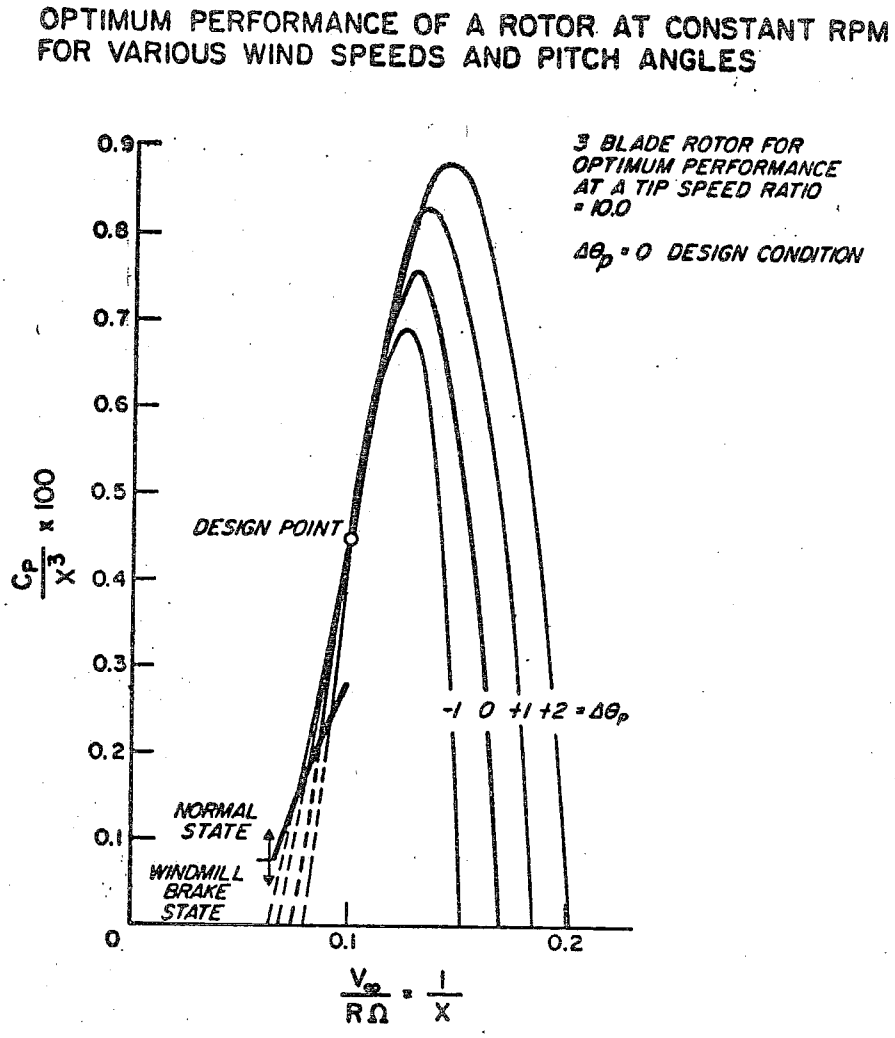

Figure 3.2.5 Blade pitch effects for operation at different wind velocities at constant RPM (1/X) for a three-bladed turbine (X_{design} = 10.0, L/D ≅ 55, C_L = 0.9 at all stations, NACA 23018 airfoil series).

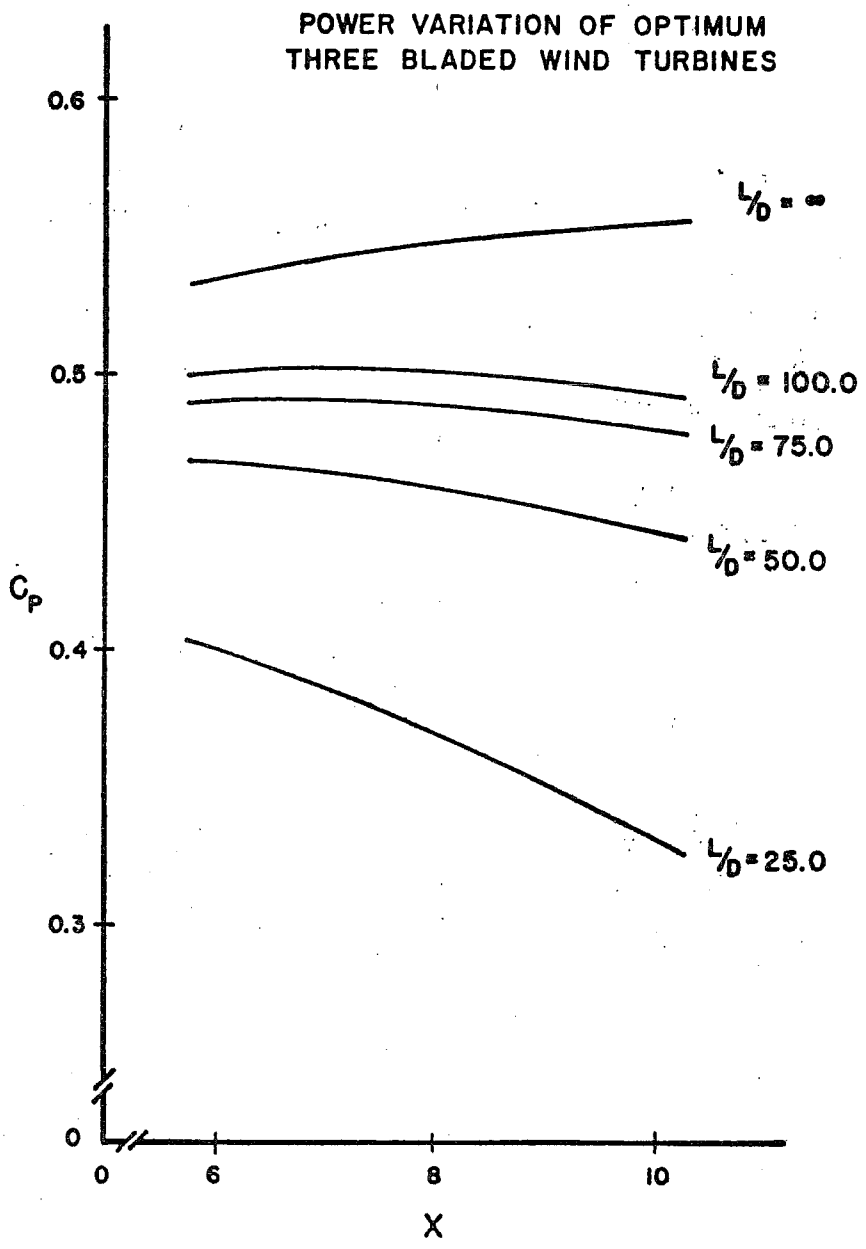

Figure 3.2.6 Power coefficient variation as affected by drag for optimum performance three-bladed wind turbines.

Table 3.2.2 gives a comparison of different methods of computing the maximum performance of a two-bladed rotor at a tip speed ratio of 10. The power coefficients are given for various blade L/D ratios.

Table 3.2.2 Comparison of Various Methods of Maximum Performance Prediction for a 2-Bladed Rotor at a Tip Speed Ratio of Ten

Method	C_P $\frac{L}{D} = \infty$	C_P 100	C_P 75	C_P 50	C_P 25
Local Opt. F=1	.585	.526	.506	.467	.349
Local Opt. Prandtl	.547	.491	.473	.436	.324
Local Opt. Goldstein	.540	.485	.467	.431	.321
Rohrbach & Worobel	.51	.46	.44	.41	
Constant Axial Velocity	.521	.462	.442	.402	.284

The first row gives the performance using Glauert's actuator disk model. Glauert's results correspond to the limiting case of infinite blade number. The second and third rows give the results using local optimization with the Prandtl and Goldstein tip loss models. As can be seen from the values of the power coefficient, the power determined using the Prandtl model is about 1% higher than that obtained using the Goldstein model. While the difference in predicted performance is only 1% the difference in calculation time is more than an order of magnitude; therefore, the Prandtl tip-loss model has been used in generating the results given in this paper.

The fourth row gives the results of Rohrbach and Worobel. Their results are seen to yield optimum performance about 5% lower than perdicted using local optimization. The difference is due to a finite hub radius. The last row gives the results when the power was optimized at

the 3/4 R blade position and the axial velocity, U, obtained at that blade position was maintained over the rest of the blade. It may be noted that this approach yields substantially the same results as Rohrbach and Worobel.

The design procedure for determining the optimum blade configurations can be illustrated with several examples.

Example Case 1. Obtain the blade configuration of a two-bladed wind turbine for operation at a tip speed ratio of ten and compare its predicted off-design performance with that determined for the NASA-ERDA MOD-0 turbine.

Procedure

First determine the optimum blade parameters, cC_L/R and ϕ. This is accomplished by using the local optimization analysis described in section 3.2. From this analysis, the angle ϕ and the chord-lift coefficient/maximum radius ratio as a function of local radius are obtained. The variation of these parameters with radius is shown in Figures 3.2.7 and 3.2.8. The next step is to select an airfoil section. For this example, we will choose NACA profile 23018, the airfoil section used on the NASA-ERDA MOD-0. The L/D maximum for this airfoil occurs near $C_L = 0.9$, at an angle of attack equal to 8°. It may be noted that the L/D ratio varies only slightly in the C_L range from 0.6 to 1.0. From the infinite number of possible variations in the cC_L product, we select two representative cases:

Design I. $C_L = 0.9$ and $\alpha = 8°$ constant along the blade.

Design II. C_L varies from 0.6 at the tip to 1.0 at the hub.

Design I

To determine the chord distribution for Design I, the cC_L product obtained from the optimization process is divided by the lift coefficient. In order to compare the optimized design with the NASA-ERDA MOD-0, the chord is given for

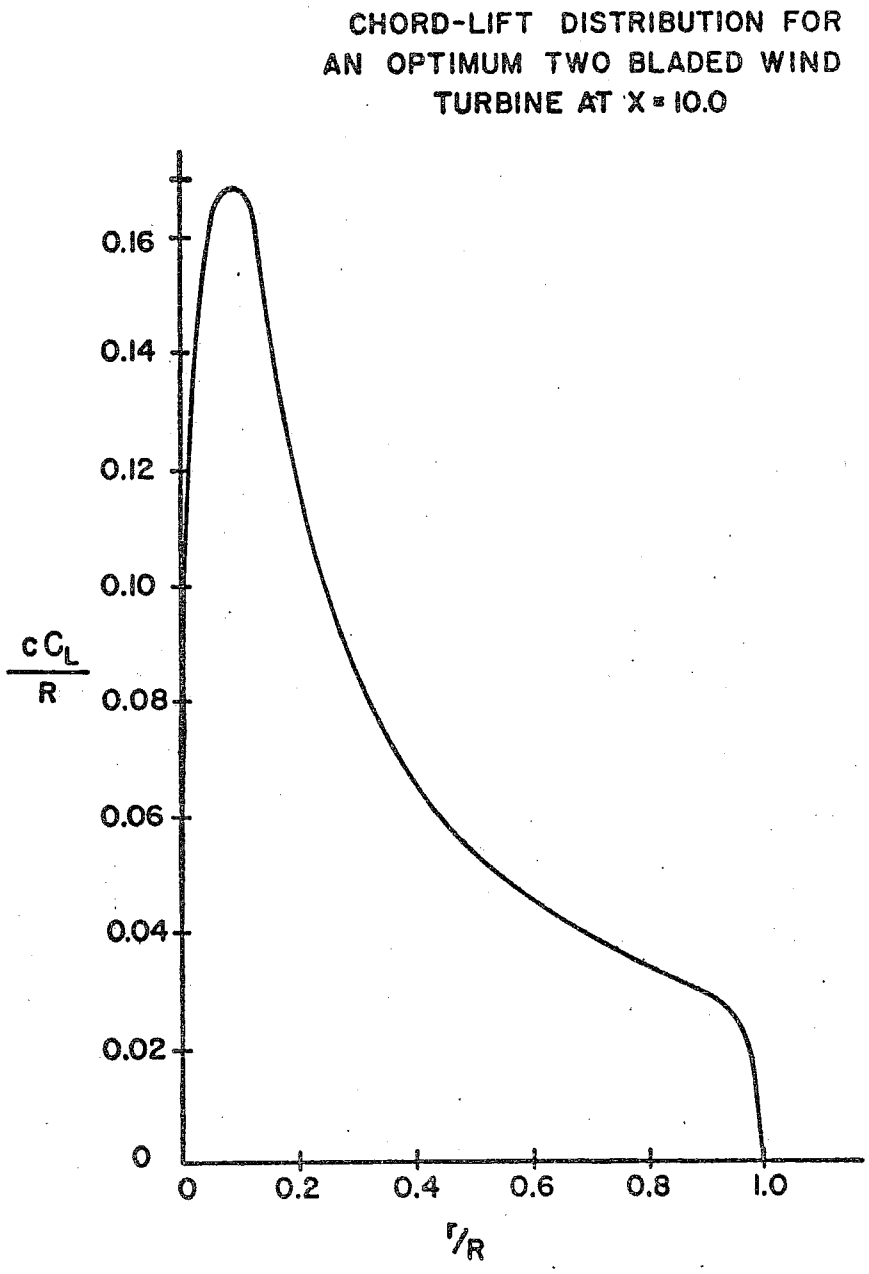

Figure 3.2.7 Optimum performance blade chord-lift distribution for a two-bladed wind turbine of a tip speed ratio of ten.

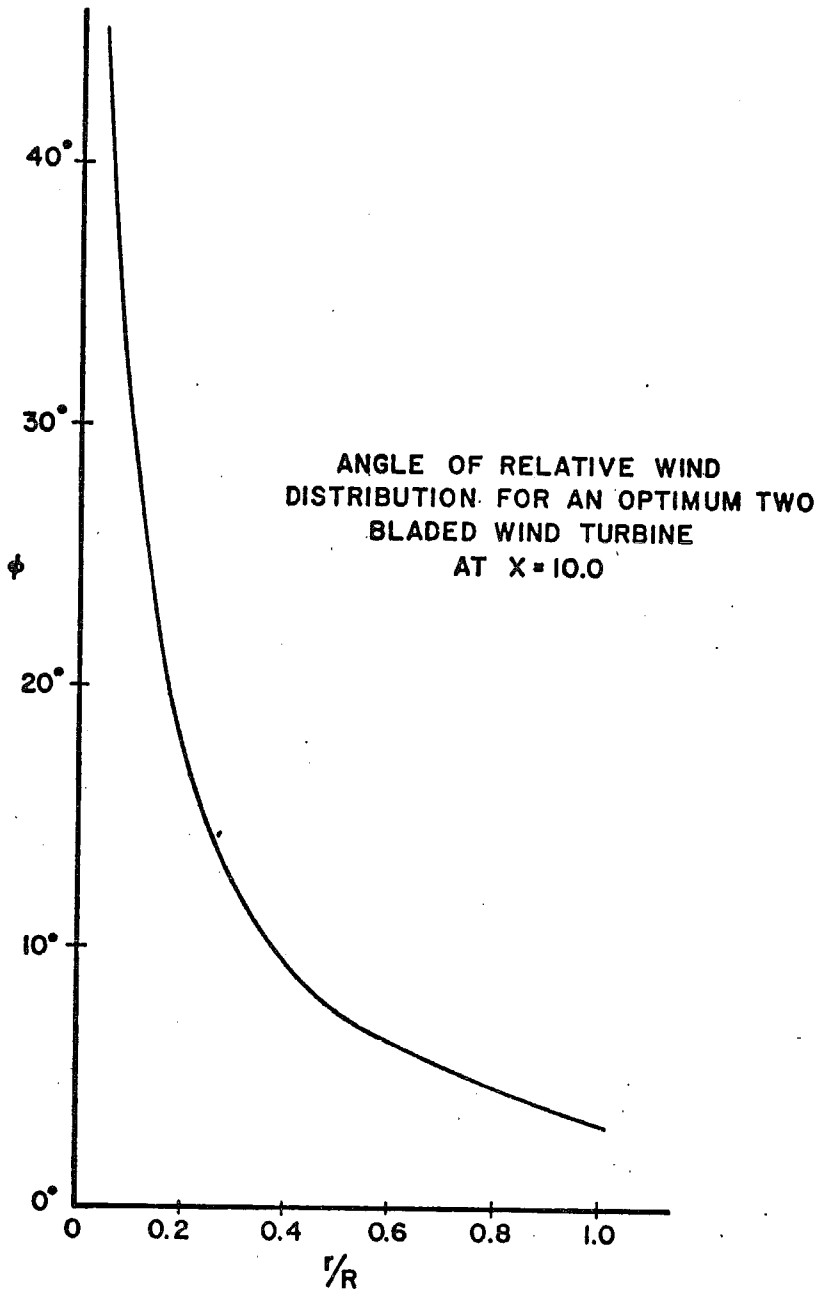

Figure 3.2.8 Optimum performance angle of relative wind for a two-bladed wind turbine at a tip speed ratio of ten.

R_{max} = 19.05 meters.

To determine the blade twist angle for Design I, we subtract the angle of attack, 8°, from the angle of relative wind, ϕ, at each station.

$$\theta_{twist} = \phi - \alpha$$

Design I is now specified as shown in Table 3.2.3.

Table 3.2.3 Blade Geometry for Design I
(C_L = 0.9, α = 8°, 2 Blades, R_{TIP} = 19.05 m)

Station	Chord (meters)	θ_{twist} (degrees)
100	0	-5.000
95	0.5919	-4.494
90	0.6422	-4.023
85	0.6867	-3.661
80	0.7312	-3.325
75	0.7794	-2.978
70	0.8330	-2.613
65	0.8952	-2.182
60	0.9665	-1.699
55	1.0506	-1.134
50	1.1500	-0.462
45	1.2698	+0.351
40	1.4161	1.357
35	1.5978	2.630
30	1.8288	4.290
25	2.1281	6.534
20	2.5210	9.710
15	3.0264	14.460
10	3.5643	21.995
5	3.4653	34.255

Design II

Design II is determined in the same way as Design I, except C_L and α vary at each station according to the following relations:

$$C_L = C_{L_{Root}} - (C_{L_{Root}} - C_{L_{Tip}})r/R$$

$$\alpha = \alpha_{Root} - (\alpha_{Root} - \alpha_{Tip})r/R$$

which can be rewritten

$$C_L = 1. - 0.4\ r/R$$

$$\alpha = 9.64° - 4.38\ (r/R)°$$

Design II is now specified as shown in Table 3.2.4.

Table 3.2.4 Blade Geometry for Design II
$C_L = 1. - 0.4\ (r/R)$,
$\alpha = 9.64° - 4.38(r/R)°$, 2 Blades, $R_{Tip} = 19.05$ m

Station	Chord (meters)	θ_{twist} (degrees)
100	0	-2.259
95	.8470	-1.972
90	.9031	-1.721
85	.9367	-1.578
80	.9677	-1.461
75	1.0019	-1.333
70	1.0415	-1.178
65	1.0887	-0.976
60	1.1445	-0.712
55	1.2122	-0.366
50	1.2939	0.087
45	1.3935	0.680
40	1.5170	1.467
35	1.6721	2.520
30	1.8703	3.902
25	2.1281	5.987
20	2.4661	8.943
15	2.8974	13.474
10	3.3418	20.790
5	3.1824	32.831

Designs I and II are compared to the blade geometry of the NASA-ERDA MOD-0 wind turbine in Figures 3.2.9 and 3.2.10. Figure 3.2.9 shows that the optimum designs have a greater blade twist nearer the hub than the MOD-0 configuration. Figure 3.2.10 shows that the MOD-0 design is a good approximation

to optimum chord distribution for Design I, except near the hub.

The performance of Designs I and II may be determined by the standard strip theory analysis used in references (13, 14). The power coefficients for off-design tip speed ratios of Designs I and II and the NASA-ERDA MOD-0 are presented in Figure 3.2.11. The NASA-ERDA MOD-0 blade design is a good approximation to the Design I optimum outer blade geometry. It is not surprising to find that the MOD-0 turbine has a power coefficient only five percent below optimum Design I at the design tip speed ratio, because outer blade geometry has the greatest influence on performance.

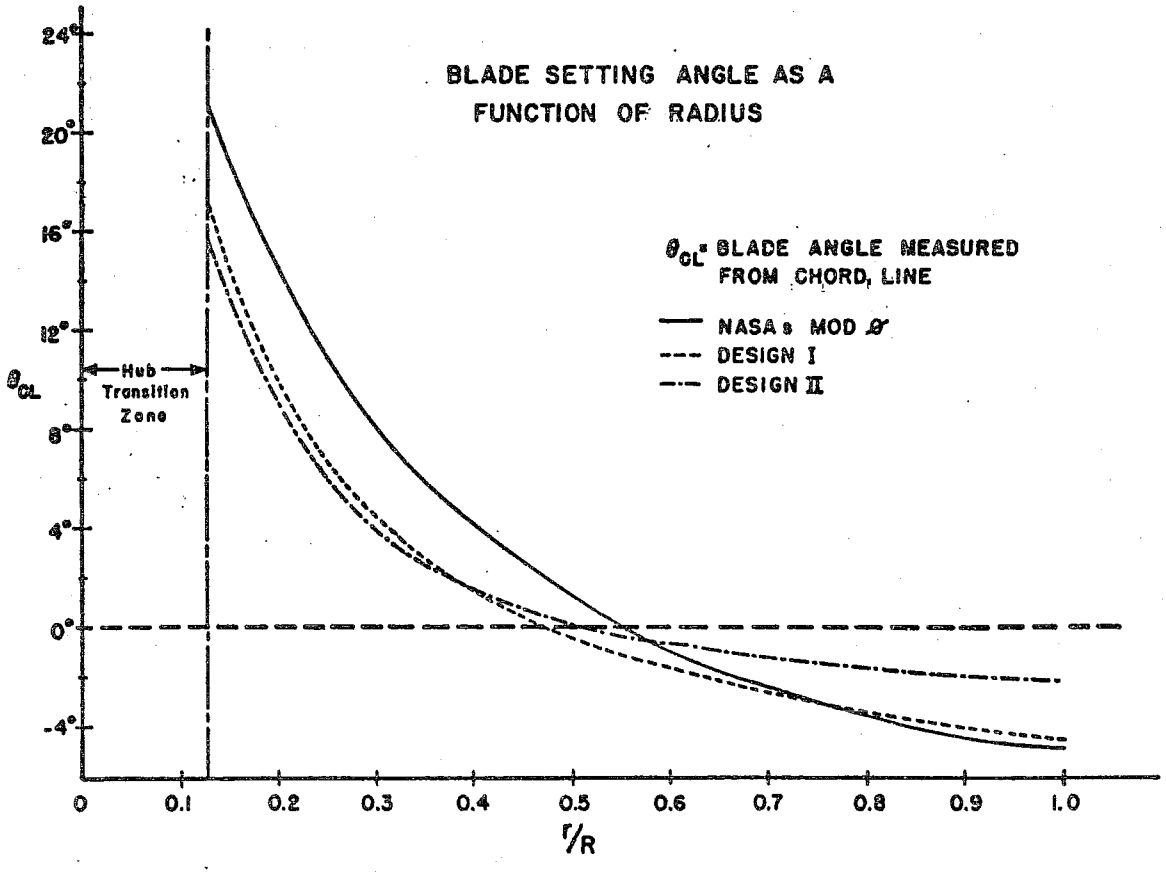

Figure 3.2.9 Blade setting angle as a function of radius for Designs I and II compared to NASA's MOD-0.

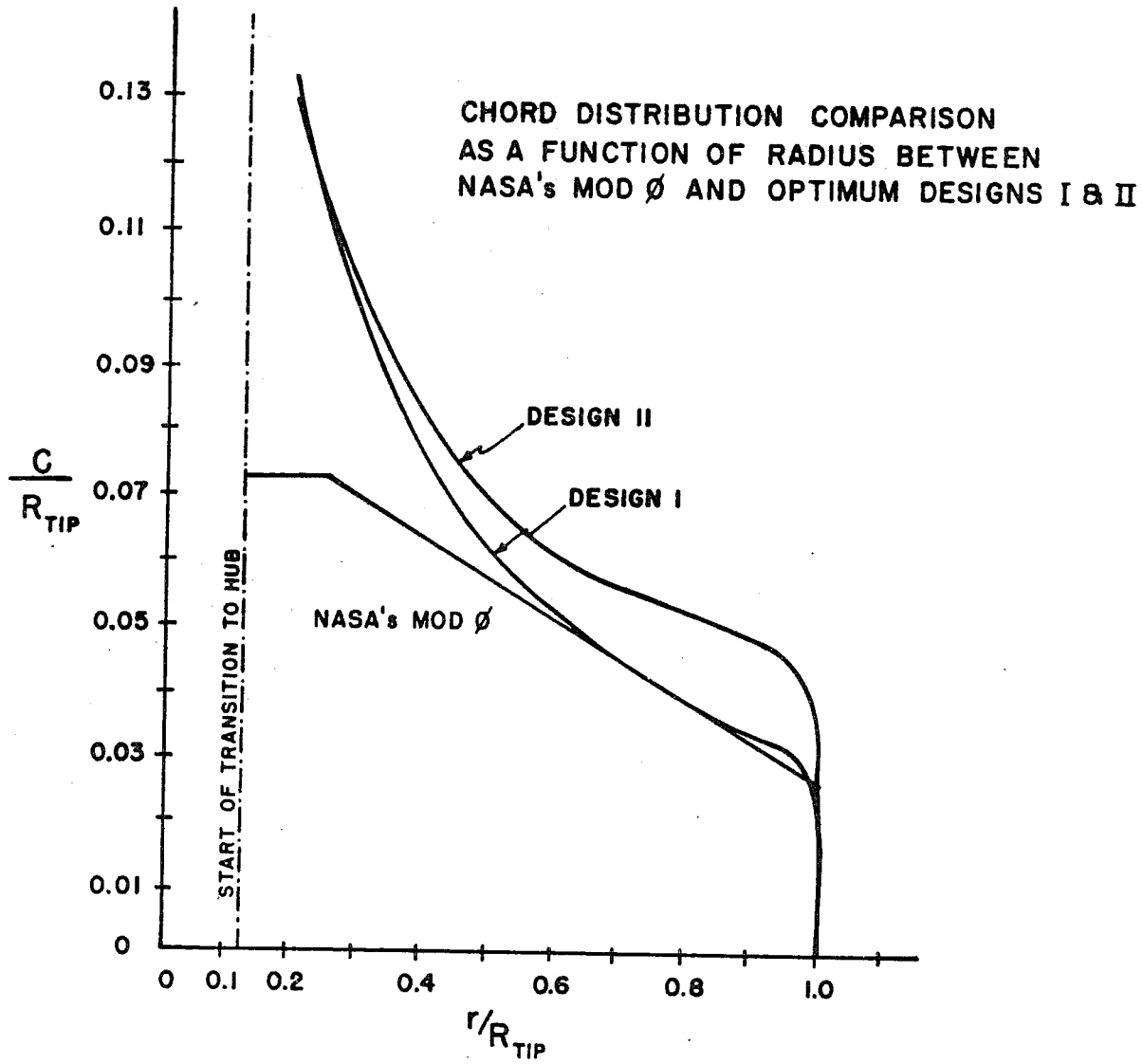

Figure 3.2.10 Blade chord distribution for Designs I and II compared to NASA's MOD-0 design.

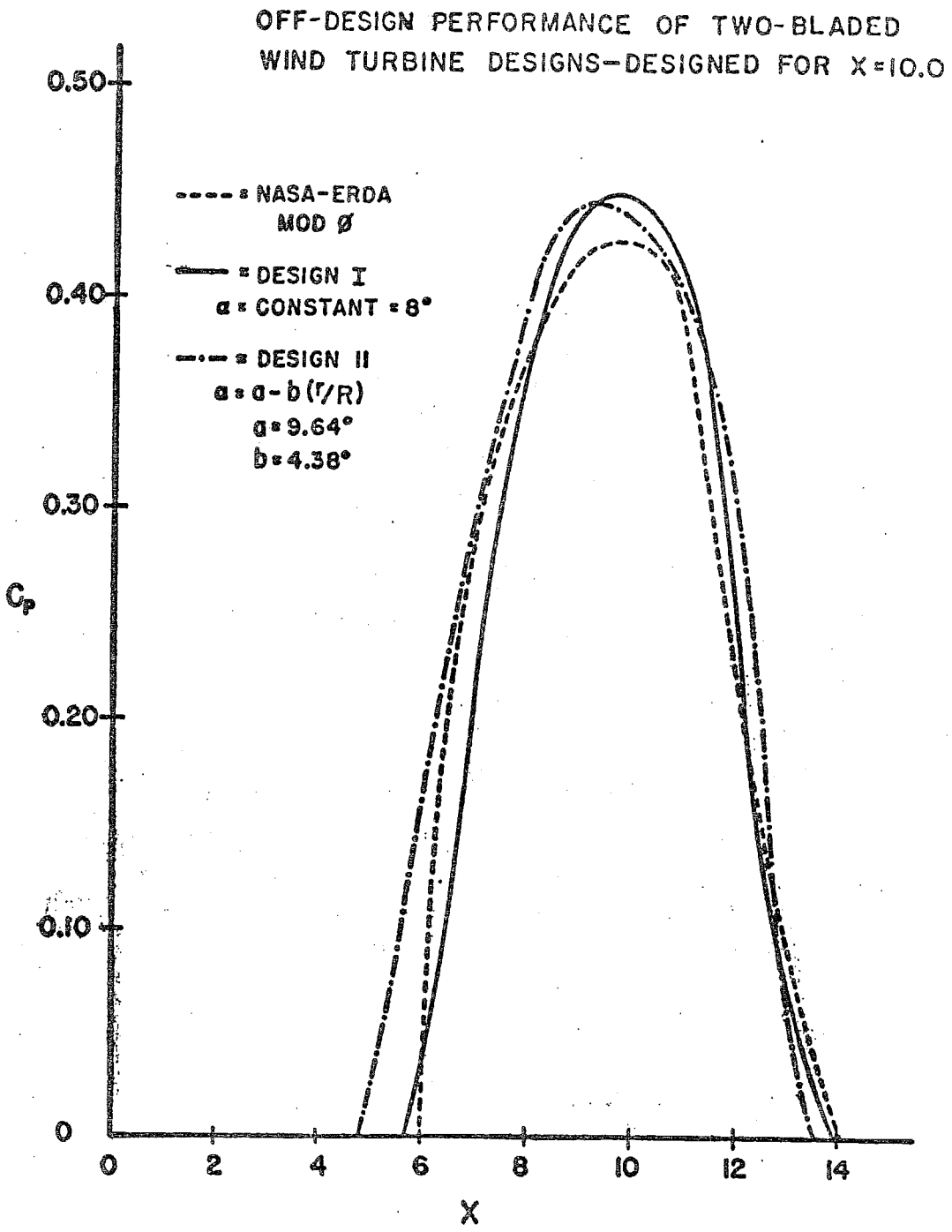

Figure 3.2.11 Off-design tip speed ratio performance for Designs I and II (two blades, X_{design} = 10.0) compared to the MOD-0 design.

Example Case 2. Determine an optimum blade configuration for a Chalk-type* wind turbine at an operating tip speed ratio of 1.75. The design should have the same design parameters as the Chalk wind turbine described in Table 3.2.5 except for the chord and blade twist distribution.

Table 3.2.5 Chalk Wind Turbine Specifications

Outside diameter	4.6482 meters
Inside diameter	1.6002 meters
Length of blades	1.5240 meters
Number of blades	48
Chord of blades	0.0883 meters
Blade pitch	9° outside rim (referenced to rotor plane)
	18° inside rim (referenced to rotor plane)
Blade twist	9°
Support wires	0.00157 meters
Number of wires	not covered by blades = 96
Length of hub in axial direction	≈ .6096 meters
Airfoil	Clark Y
$C_{P_{max}}$	0.3

Procedure

To generate an optimum design, again we use the procedure of section 3.2 to obtain the blade design parameter variations for a 48 blade wind turbine at a tip speed ratio of 1.75 as shown in Figures 3.2.12 and 3.2.13. The sectional aerodynamics were obtained from Schmitz[15]. At a Reynolds number of 105,000, it can be determined that the most suitable L/D range is between 12.5 and 13.5. Choosing a chord dimension such that the lift coefficient calculated at each blade station (using Figure 3.2.13), is in the suitable L/D range and does not exceed the maximum lift coefficient, we can determine the angle of attack.

* Invented by Thomas Chalk.

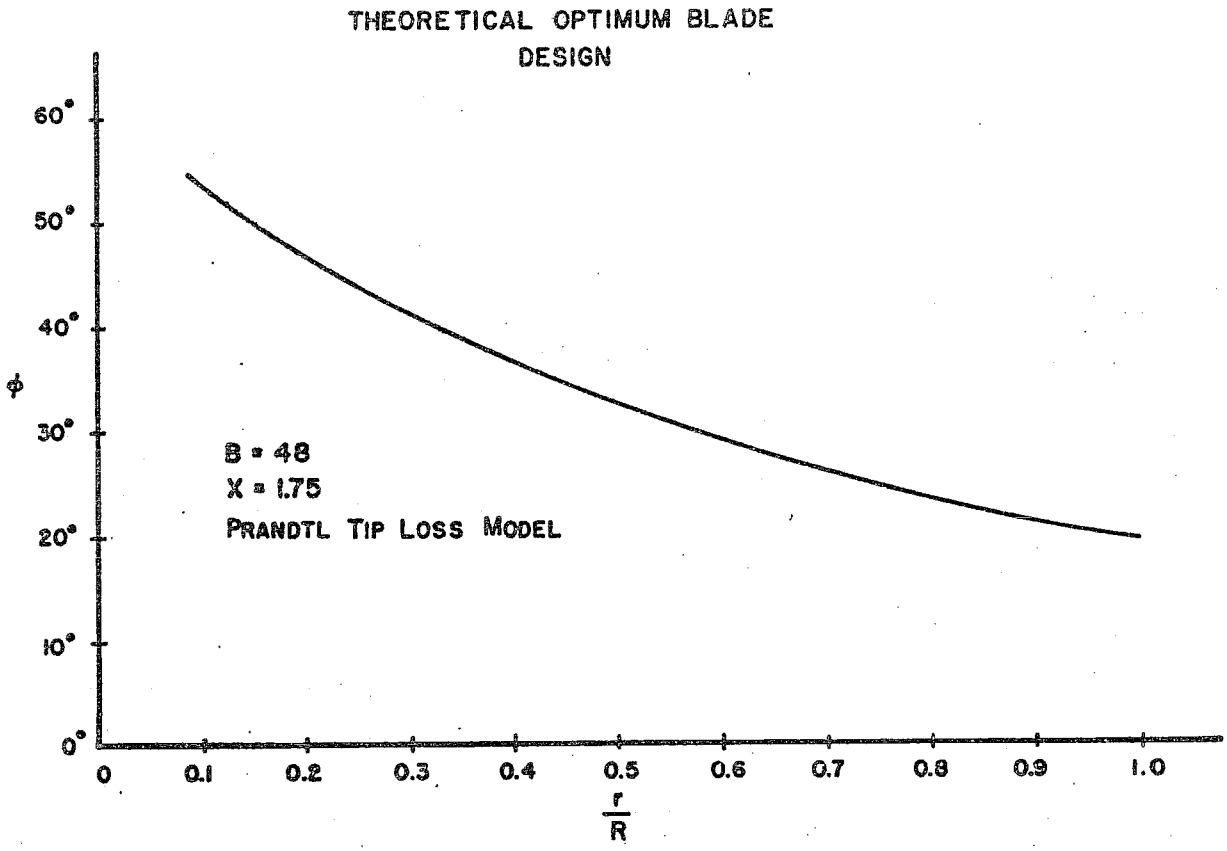

Figure 3.2.12 Optimum angle of relative wind for Chalk-type wind turbines at a tip speed ratio of 1.75.

Using Figure 3.2.12 to determine the angle of the relative wind at each station and subtracting the angle of attack at each station, the blade twist angle distribution may be determined as listed in Table 3.2.6 and shown in Figure 3.2.14.

Comparing the optimum design parameters, Table 3.2.6, to the Chalk wind turbine, Table 3.2.5, we observe that the blade chord and blade twist are increased substantially from the original design. Figure 3.2.15 illustrates the effect of the lift/drag ratio on an optimum Chalk wind turbine and on an optimum high speed wind turbine.

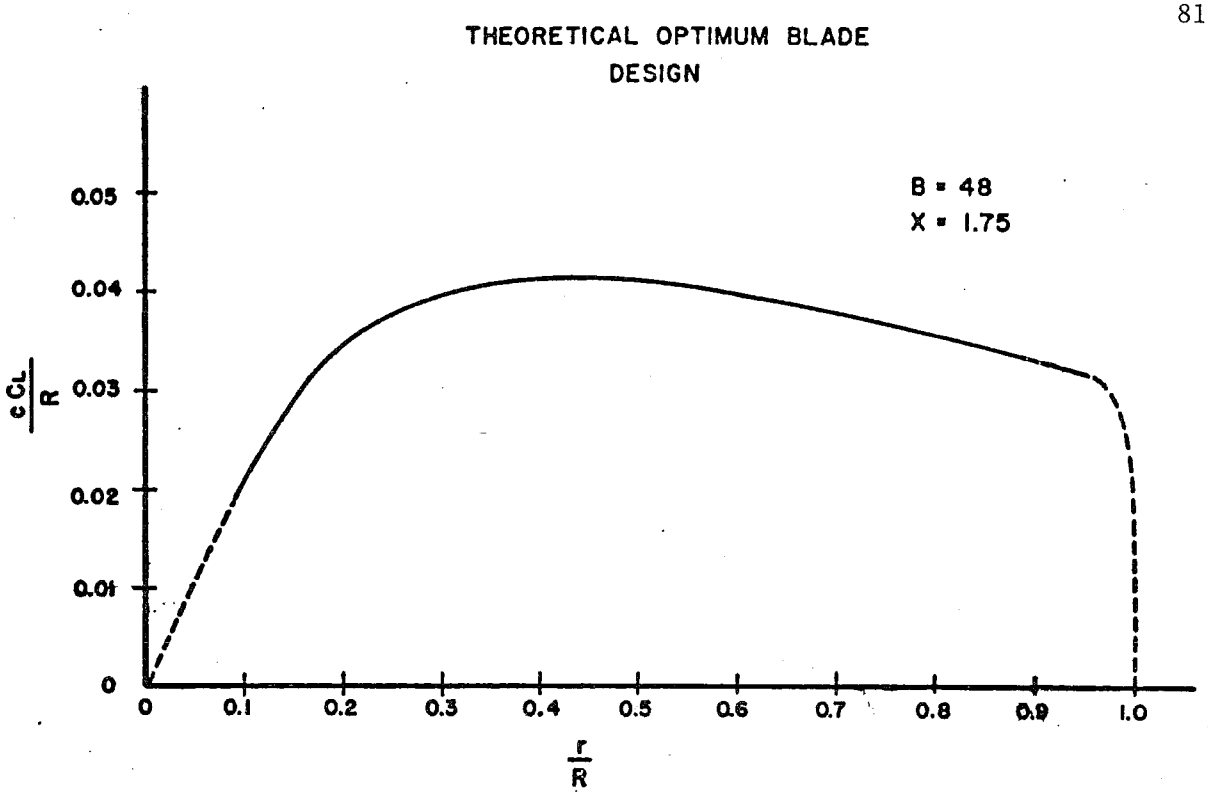

Figure 3.2.13 Optimum blade chord-lift distribution for a Chalk-type wind turbine at a tip speed ratio of 1.75.

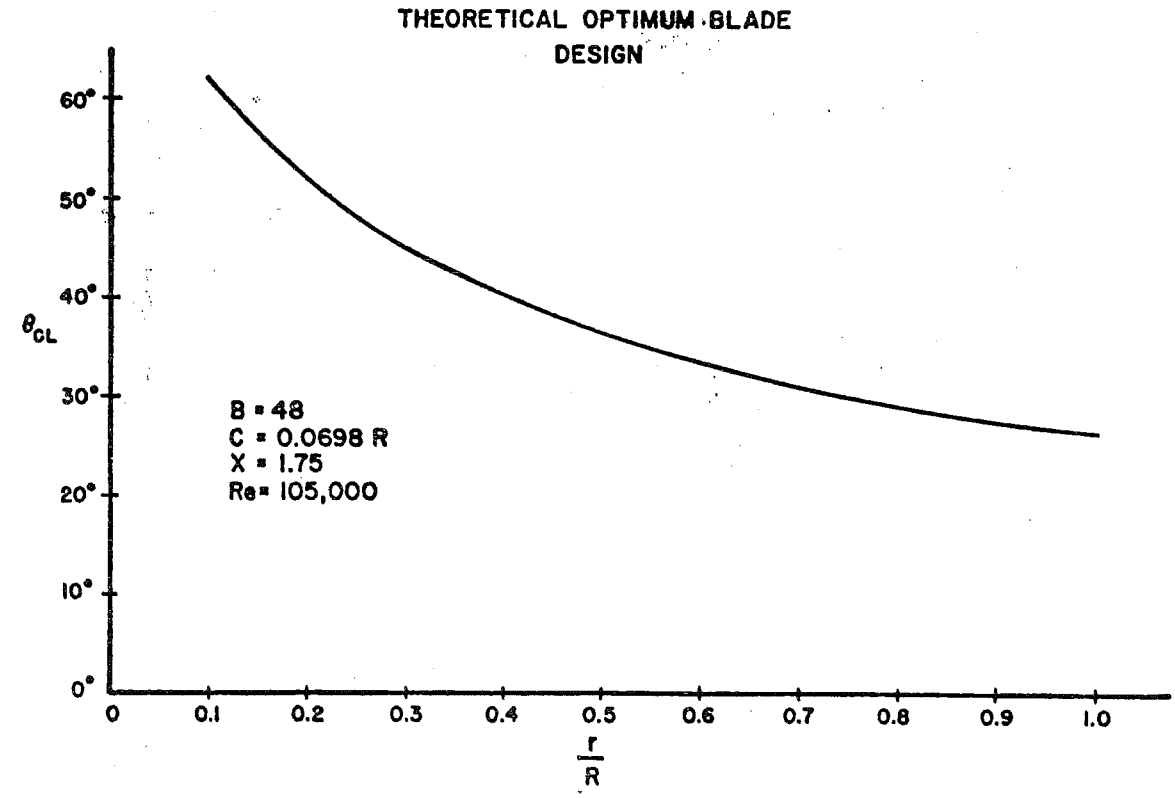

Figure 3.2.14 Optimum blade design for a Chalk-type wind turbine (θ_{CL} - blade angle measured from chord line).

Table 3.2.6 Optimum Geometry for Chalk Wind Turbine

r/R x 100%	c/R	C_L	α°	θ° zero lift line	θ° chord line
100	.0698	0.430	0	19.5	26.2
90	.0698	0.473	0.7	20.6	27.3
80	.0698	0.509	1.3	22.2	28.9
70	.0698	0.540	1.8	24.3	31.0
60	.0698	0.568	2.2	26.8	33.5
50	.0698	0.589	2.6	30.0	36.7
40	.0698	0.595	2.7	33.9	40.6
30	.0698	0.573	2.3	37.8	44.5
20	.0698	0.494	1.1	45.0	51.7
10	.0698	0.302	-2.0	55.4	62.1

L/D range, 12.5 → 13.5
Maximum radius, 2.3241 m
Hub radius, 0.8001 m
Chord, 0.1621 m

Tip blade angle, 26.2°
Hub blade angle, 42.5°
Blade twist, ∿ 16°

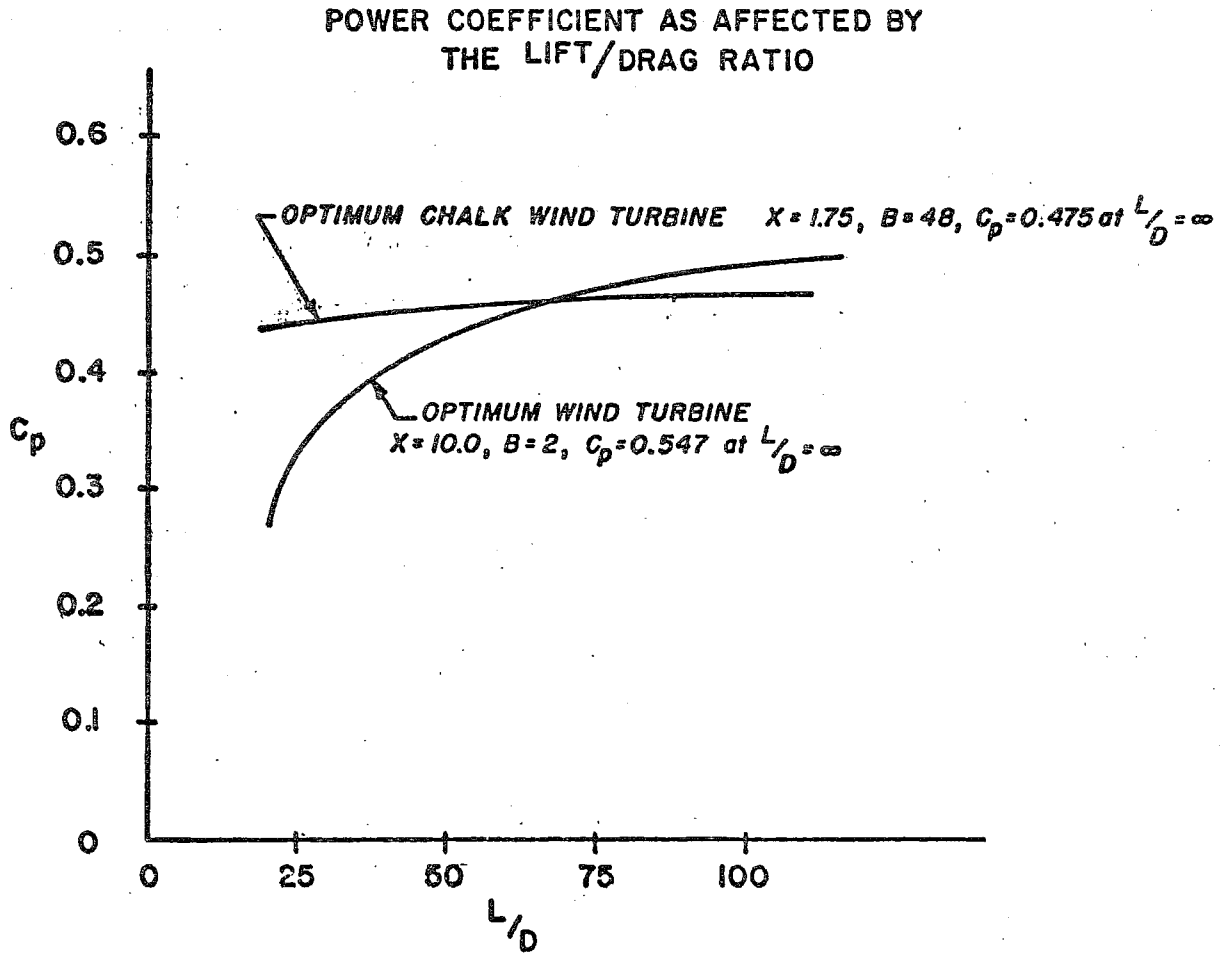

Figure 3.2.15 Power coefficient as affected by the lift/drag ratio for the optimum Chalk wind turbine and an optimum two-bladed wind turbine.

3.4 CLOSURE

Performance optimization of wind turbines does not share the rigorous foundation that exists for the determination of optimum performance propellers. A strip theory approach using local optimization results in higher calculated performance than either constant axial velocity or constant wake displacement velocity methods that have been applied to wind turbines.

Optimized wind turbines perform best at high lift/drag ratios as is to be expected. Structural and cost considerations, as well as off-design operating conditions may dictate some departure from the performance optimized configuration. Knowledge of the optimized configuration will enable design changes to be directed as to minimize performance loss.

Figures 3.4.1, 3.4.2, 3.4.3, and 3.4.4 summarize the maximum performance that can be obtained from horizontal axis wind turbines.

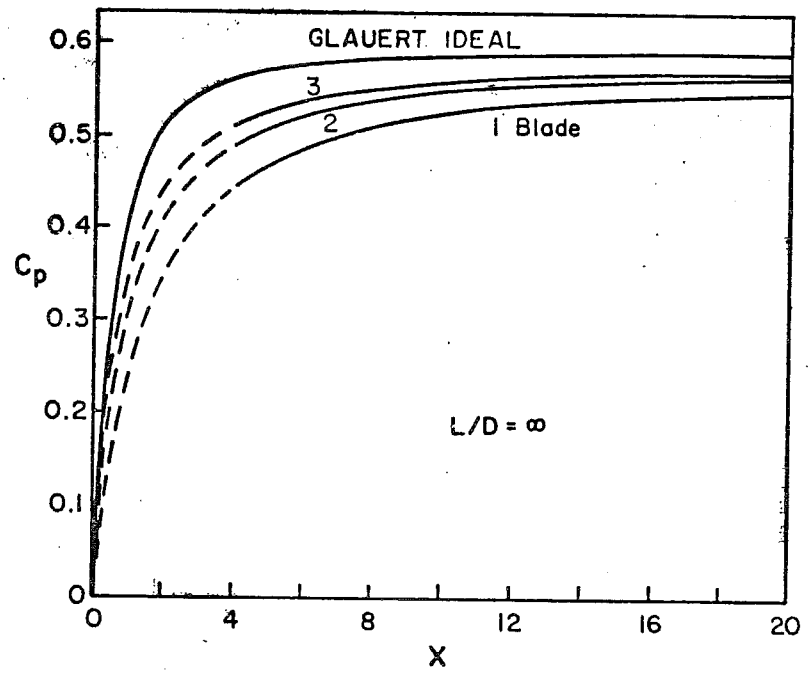

Figure 3.4.1 Effect of Number of Blades on Peak Performance of Optimum Wind Turbines

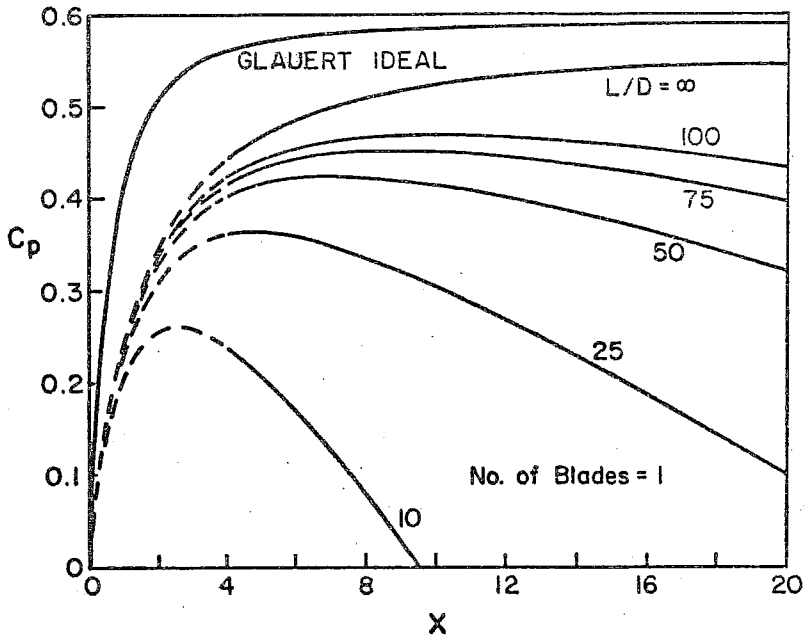

Figure 3.4.2 Effect of L/D on Peak Performance of Optimum One-Bladed Wind Turbines

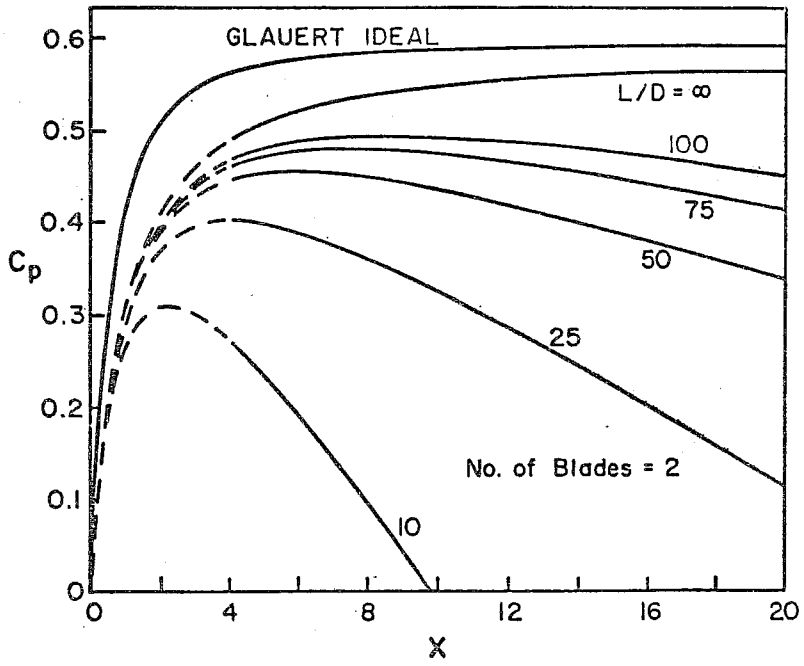

Figure 3.4.3 Effect of L/D on Peak Performance of Optimum Two-Bladed Wind Turbines

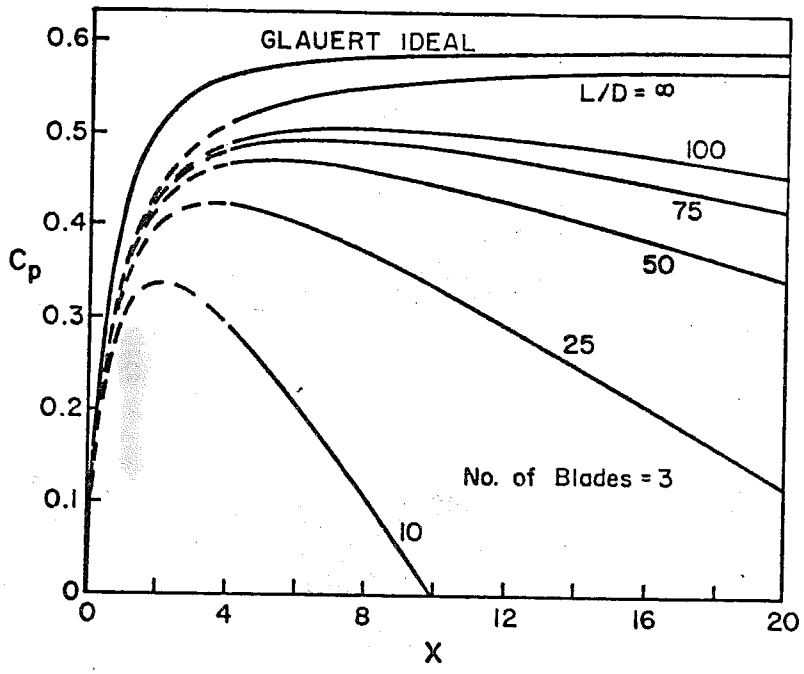

Figure 3.4.4 Effect of L/D on Peak Performance of Optimum Three-Bladed Wind Turbines

REFERENCES

1. Betz, A., Gottinger Nachr., p. 193, 1919.

2. Goldstein, S., "On the Vortex Theory of Screw Propellers," Proc. Royal Soc. A123, 440, 1929.

3. Theodorsen, Theodore, "The Theory of Propellers, I - Determination of the Circulation Function and the Mass Coefficient for Dual-Rotating Propellers, NACA Rept. 775, 1944.

4. Theodorsen, Theodore, "The Theory of Propellers, II - Method for Calculating the Axial Interference Velocity," NACA Rept. 776, 1944.

5. Theodorsen, Theodore, "The Theory of Propellers, III - The Slipstream Contraction with Numerical Values for Two-Blade and Four-Blade Propellers," NACA Rept. 777, 1944.

6. Theodorsen, Theodore, "The Theory of Propellers, IV - Thrust, Energy and Efficiency Formulas for Single and Dual-Rotating Propellers with Ideal Circulation Distribution," NACA Rept. 778, 1944.

7. Theodorsen, Theodore, "Theory of Propellers," McGraw-Hill Book Co., Inc., New York, 1948.

8. Crigler, John L., "Application of Theodorsen's Theory to Propeller Design," NACA Report 924.

9. Lerbs, H. W., "An Appropriate Theory of Heavily Loaded Free-Running Propellers in the Optimum Condition," Trans. Soc. NAVAL Architects and Marine Engrs., 137-183, 1950.

10. Lerbs, H. W., "Moderately Loaded Propellers with a Finite Number of Blades and an Arbitrary Distribution of Circulation," Trans. Soc. Naval Architects and Marine Engrs., 60, 73-117, 1952.

11. Rohrbach, Carl and Worobel, Rose, "Performance Characteristics of Aerodynamically Optimum Turbines for Wind Energy Generators," American Helicopter Soc., Preprint No. S-996, May 1975.

12. Durand, W. F. (Ed.), "Aerodynamic Theory," Glauert, H., "Airplane Propellers," Vol. IV, Division I, Chapter VII, Section 4, pp. 169-360, Julius Springer, Berlin, 1935.

13. Wilson, Robert E. and Lissaman, Peter B. S., "Applied Aerodynamics of Wind Power Machines," Oregon State University, May 1974.

14. Walker, Stel N., "Performance and Optimum Design Analysis/Computation for Propeller-Type Wind Turbines," Ph.D. Thesis, Oregon State University, May 1976.

15. Schmitz, F. W., "Aerodynamics of the Model Airplane, Part 1, Airfoil Measurements," N70-39001, NTIS, November 1967.

16. Rohrbach, Carl and Worobel, Rose, Private Communication, June 1976.

CHAPTER IV

AERODYNAMICS OF THE DARRIEUS ROTOR

INTRODUCTION

Interest in the wind as an alternative energy source has resulted in a number of investigations of unconventional wind-powered machines. South and Rangi[1] have developed a vertical axis turbine of a type earlier proposed by Darrieus[2]. This device is illustrated in Figure 4.0.1. The performance of Darrieus-type rotors has been experimentally determined by wind tunnel tests.

Performance models of the Darrieus Rotor have been formulated by Wilson and Lissaman[3], Templin[4], James[5], Muraca[6], Shankar[7], Strickland[8] and Holme[9]. The flow models published by Wilson and Lissaman, Shankar and Strickland are identical and have been found to yield the best correlation with experimental results, however Holme's analysis is considered to be the most rigorous to date in that the effects of both bound and wake vorticity are included. Since Holme's analysis is restricted to linear aerodynamics and 2-D rotors no test data comparisons are possible. The current method of performance analysis for 3-D machines[3,7,8] is in essence a strip theory in which the time-averaged force on a blade element is equated to the mean momentum flux through a streamtube of fixed location and dimensions. The analysis uses quasi-steady aerodynamics neglecting the effects of mutual interference and of more significance, neglects the effects of the rear blades in crossing the vortex sheets of the forward blades (front and rear blade loads are the same). While the analysis correlates well with the available test data, it may be noted that the test data obtained to date has centered on time-averaged quantities such as power and the force in the free stream direction.

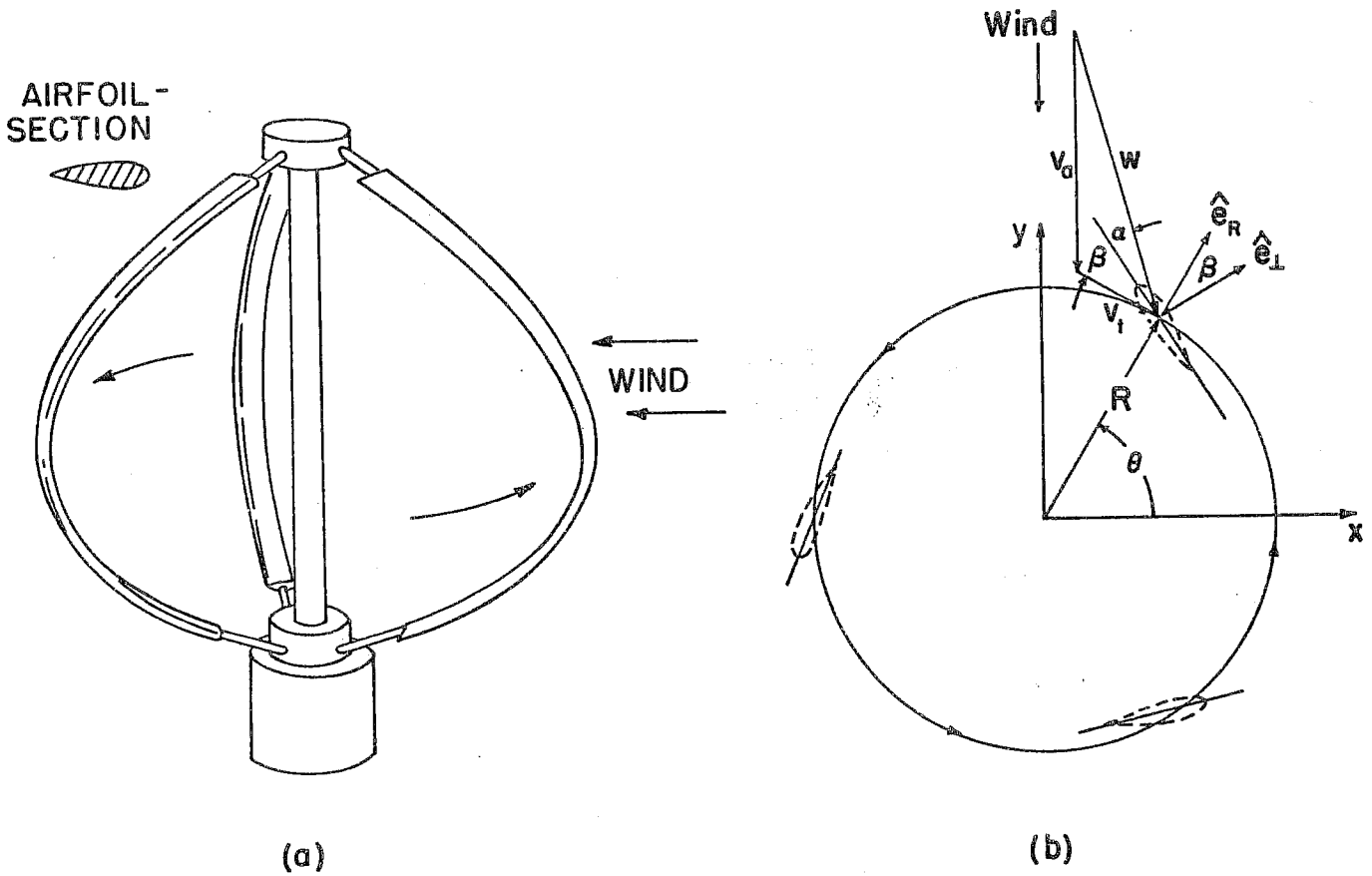

Figure 4.0.1 Darrieus Wind Turbine and Flow System

4.1 LINEAR THEORY

To analyze a Darrieus-type crosswind-axis device we adopt the standard approach of wing theory, which is to express the forces on the system by a momentum analysis of the wake as well as by an airfoil theory at the lifting surface itself. The expression for these forces contains unknown induced flows. By equating the wake and blade forces one obtains sufficient equations to determine the induced flows.

For the device considered we assume that each spanwise station parallel to the axis behaves independently in the sense that the forces on the device at each station may be equated to the wake forces. In general, these devices can experience a windwise as well as a cross-wind force, so that the wake can be deflected to the side.

Consistent with vortex theory of airfoils, we will assume the induced flows at the device are one half their value in the wake. Thus, we obtain that if the wake windwise perturbation is $\Delta V \simeq -2aV_\infty$, then at the device itself the incoming flow has velocity $V_\infty(1-a)$, giving the flow system illustrated in Figure 4.0.1.

In order to simplify the analysis we shall first adopt the following assumptions,

1. $\beta = 0$
2. $C_D = 0$
3. $C_L = 2\pi \sin\alpha$
4. $c << R$
5. Straight blades ($\gamma=0$)

Our results will then be limited to an inviscid analysis at high tip speed ratios where the maximum angle of attack α is small. The low tip

speed ratio performance requires numerical analysis to model the nonlinear aerodynamics near stall. Using the above assumptions and starting with the Kutta-Joukowski law, we can write

$$\frac{dL}{dz} = \rho W\Gamma = 1/2\rho W^2 c C_L$$

so that

$$\Gamma = \frac{c}{2} WC_L = \pi c W \sin \alpha$$

Since the force on the airfoil can be expressed as

$$\frac{d\vec{F}}{dz} = \rho \vec{W} x \vec{\Gamma}$$

we obtain

$$\frac{d\vec{F}}{dz} = p\pi c \left[-V_a V_t \sin^2\theta \hat{j} - (V_a \sin \theta + V_a V_t \sin \theta \cos \theta)\hat{i}\right] \qquad (4.1.1)$$

Now we can equate the force on the airfoil to the change in momentum in the streamtube which the airfoil occupies. Let the streamtube be of width dx when the airfoil goes from angular position θ to position $\theta + d\theta$. The width dx is related to $d\theta$ by

$$dx = Rd\theta|\sin \theta|$$

The process will repeat itself every revolution so the time interval of our analysis shall be one period which is $2\pi/\Omega$. Of this time period, the airfoil will spend a time increment of $d\theta/\Omega$ in the front portion of the streamtube and another time increment of $d\theta/\Omega$ in the rear portion of the wake. Since the streamwise force contribution from equation (4.1.1) is seen to be symmetrical with respect to the angles $\pm\theta$ we may write the blade force equation for the time period $2\pi/\Omega$ as

$$\left(\hat{j} \cdot \frac{d\vec{F}}{dz}\right)_{blade} = -2\rho\pi c V_t V_a \sin^2\theta \frac{d\theta}{\Omega}$$

Now the momentum equation yields the force in the streamtube as

$$\left(\hat{j} \cdot \frac{d\vec{F}}{dz}\right)_{momentum} = \rho R d\theta |\sin\theta| (1-a) V_\infty 2V_\infty a \frac{2\pi}{\Omega}$$

Equating these two forces under the assumption that $V_a = V_\infty(1-a)$ and $V_t = R\Omega$ yields an expression for the axial induction factor a for one blade

$$a = \frac{c}{2R} \frac{R\Omega}{V_\infty} |\sin\theta|$$

or for B blades

$$a = \frac{Bc}{2R} \frac{R\Omega}{V_\infty} |\sin\theta|$$

Now that a is defined, the blade force may be resolved into tangential and radial components. The torque is given by

$$Q = \rho\pi c R V_\infty^2 (1-a)^2 \sin^2\theta$$

The average torque for a rotor with B blades is

$$\overline{Q} = [\rho\pi BcRV_\infty^2] \left[1/2 - \frac{4}{3\pi}\frac{BcX}{R} + \frac{3}{32}\left(\frac{BcX}{R}\right)^2\right]$$

and the corresponding sectional power coefficient is given by

$$C_p = \frac{\text{Power}}{1/2\ \rho V_\infty^2 (\text{Swept Area})} = \pi X \frac{Bc}{R}\left[1/2 - \frac{4}{3\pi}\frac{BcX}{R} + \frac{3}{32}\frac{B^2c^2X^2}{R^2}\right]$$

where $X = \frac{R\Omega}{V_\infty}$ is the tip speed ratio.

This expression yields a maximum power coefficient of 0.554 when the quantity $BcX/2R = a_{max} = 0.401$. Further refinements can be made with consideration of drag and stall.

Figure 4.1.1 illustrates the dimensionless mass flow, streamwise force and power for the case of a cylindrical rotor using the analysis of Templin[4], Wilson and Lissaman[3] and Holme[9]. The coefficients are defined for a unit depth of rotor.

$$C_{\dot{m}} = \frac{\text{Mass Flux}}{\rho V_\infty 2R \cdot 1}$$

$$C_T = \frac{\text{Streamwise Force}}{1/2\pi V_\infty^2 \; 2R \cdot 1}$$

$$C_P = \frac{\text{Power}}{1/2\rho V_\infty^3 \; 2R \cdot 1}$$

Templin's analysis uses a uniform induced velocity while the analysis of Holme considered induced velocities that varied in both the x and y directions.

From the figure it may be seen that all three theories approach the same limits for zero loading. For large loadings however the so-called multiple streamtube method[3,7,8] yields better agreement with the results of Holme. Neither our analysis nor that of Templin's predicts unsymmetrical loading conditions as does the analysis of Holme. Holme's results show that the blade encounters higher angles of attack at the front stations than at the rearward positions.

Figure 4.1.2 shows the position of the shed vorticity for both the Templin model and our flow model. Since the flow through the rotor is uniform in Templin's model the vorticity sheet does not deform in the streamwise direction. In the case of non-uniform induced velocities it may be seen that the shed vortex sheet deforms continuously in the streamwise direction.

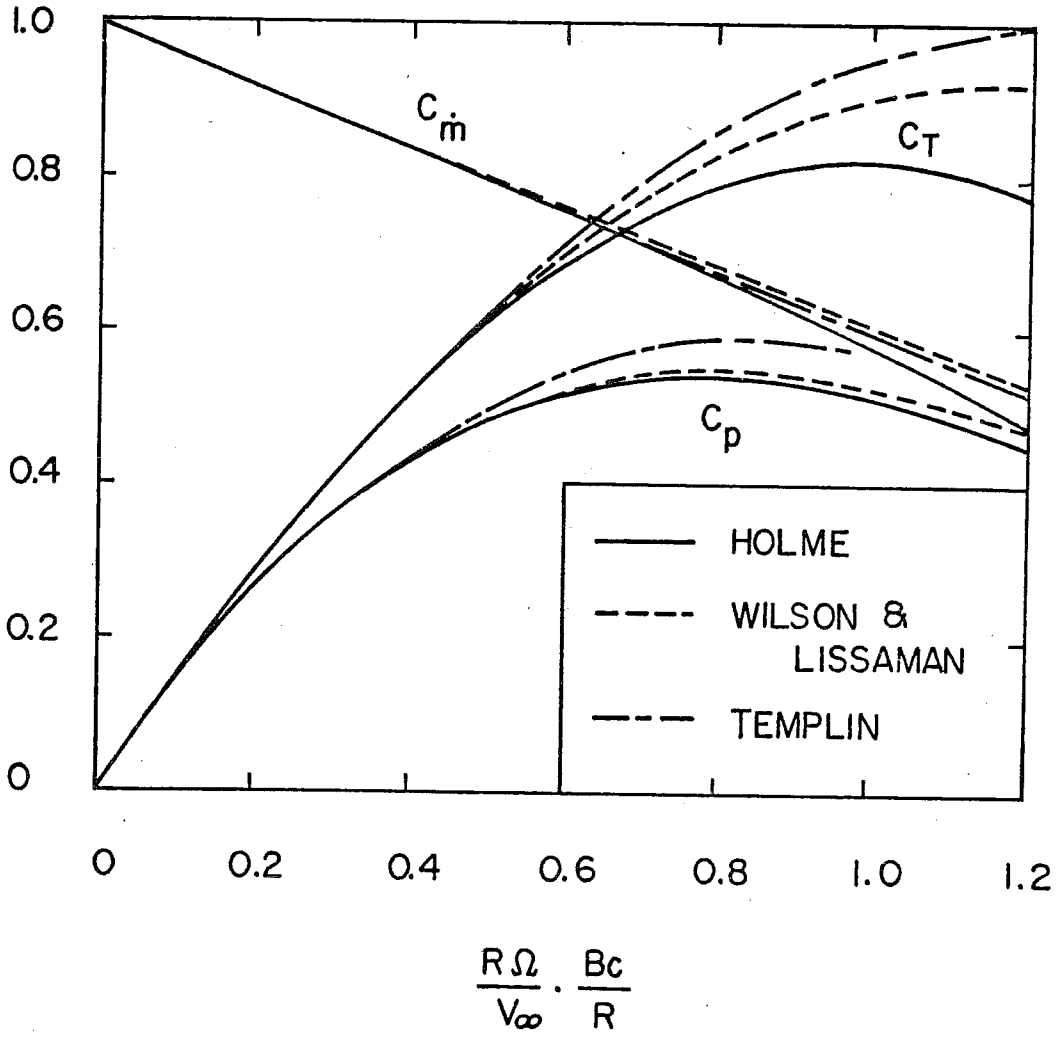

Figure 4.1.1 Mass Flow, Resultant Force and Power Coefficients in Non-Viscous Flow

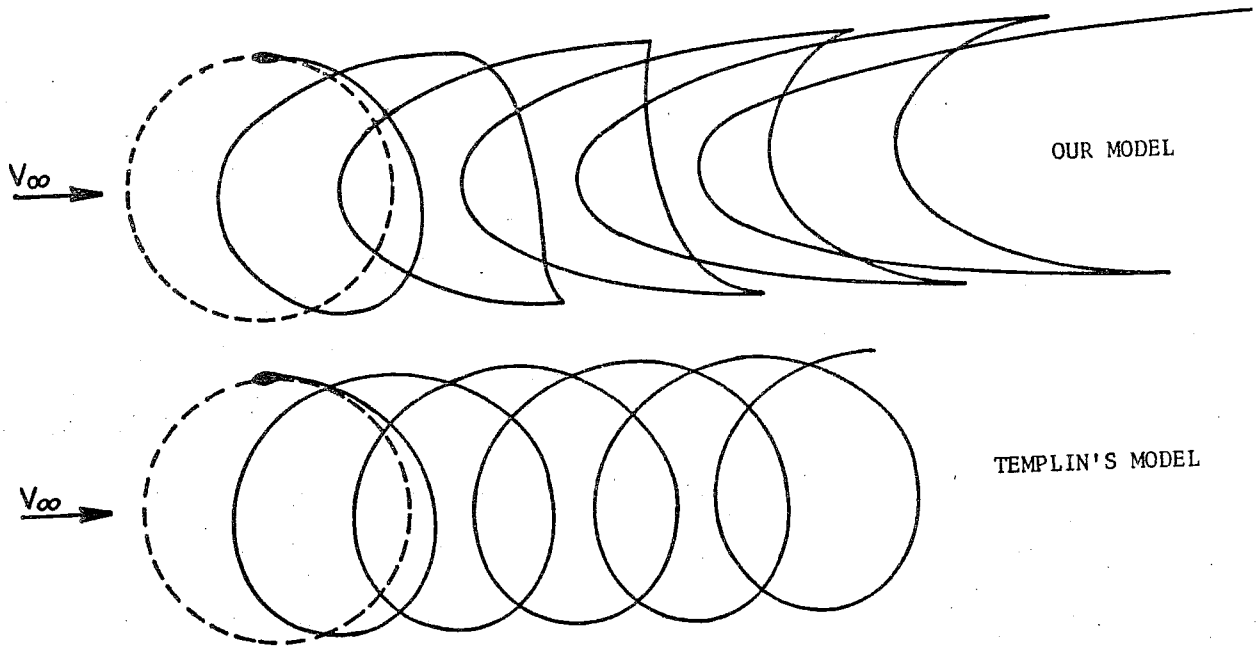

Figure 4.1.2 Position of Shed Vorticity

At the high rotational speeds required for the Darrieus-type rotor, the inertial loads are large and result in substantial bending loads in the blades. These bending loads may be removed by deploying the blade in a shape similar to the catenary so that the loads are entirely tensile. The required shape has been investigated by Blackwell[10] and given the name troposkien. The curve is described by elliptic integrals and is approximated by a sine curve or parabola. The effect on performance caused by bringing the blades closer to the axis of rotation is substantial since both the local rotational speed and the usable component of the lift are reduced.

The analysis of a curved rotor proceeds in the same manner as above. If we analyze a unit height of the rotor, the expression for a becomes

$$a = \frac{Bc}{R_m} X \cos \gamma |\sin \theta|$$

where γ is the local angle between the blade tangent and the axis of rotation. The average torque generated by a slice dz along the axis of rotation is

$$\frac{d\bar{Q}}{dz} = \rho \pi Bc V_\infty^2 \cos \gamma \left[1/2 - \frac{8}{3\pi} \sigma X \cos \gamma + \frac{3}{8} \sigma^2 X^2 \cos^2 \gamma\right]$$

and the incremental power coefficient is

$$\frac{dC_p}{dz} = \frac{d\bar{Q}}{dz} \frac{\Omega}{1/2 \rho V_\infty^2 A} = \frac{4\pi\sigma X}{A} R \cos \gamma \left[1/2 - \frac{8}{3\pi} \sigma X \cos \gamma + \frac{3}{8} \sigma^2 X^2 \cos^2 \gamma\right] \qquad (4.1.2)$$

where $\sigma = \frac{Bc}{2R_m}$ is a solidity defined as the ratio of blade circumference to disc diameter.

The integration of equation (4.1.2) for an arbitrary geometry may be accomplished; one simple case is the circular blade for which a maximum power coefficient of 0.536 occurs at $\sigma X = a_{max} = 0.461$.

4.2 NON-LINEAR THEORY

In the previous section, the aerodynamics of the Darrieus Rotor was examined for the case in which $C_L = 2\pi\sin\alpha$. This lift curve selection results in a linear relation between the circulation Γ and the component of the relative wind that is perpendicular to the blade. Since airfoils do not exhibit lift coefficients that are expressible in single closed form analytical expressions, a numerical approach must be used.

Figure 4.2.1 below shows a curved Darrieus Rotor blade and the unit vectors to be used in describing the flow. It is to be noted that $\vec{e}_B$ is a unit vector which is parallel to the blade.

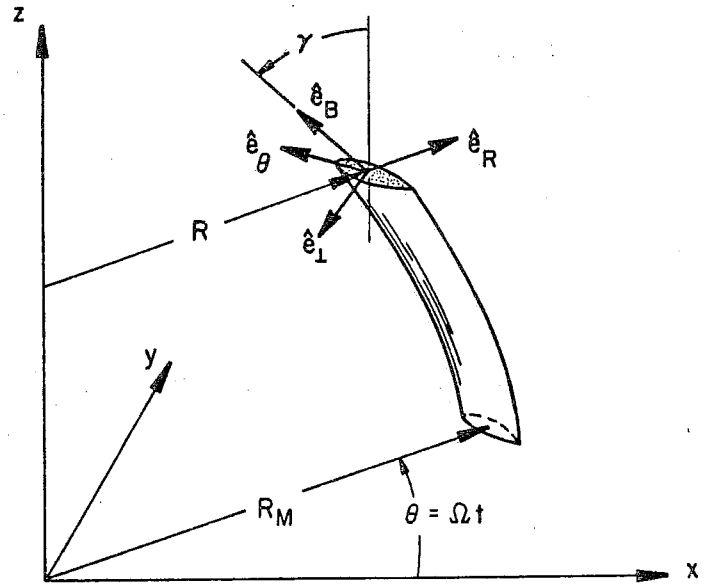

$$\hat{e}_R = \hat{i}\cos\theta + \hat{j}\sin\theta$$

$$\hat{e}_\theta = -\hat{i}\sin\theta + \hat{j}\cos\theta$$

$$\hat{e}_\perp = -\hat{e}_R\cos\gamma - \hat{k}\sin\gamma$$

$$\hat{e}_B = \hat{k}\cos\gamma - \hat{e}_R\sin\gamma$$

Figure 4.2.1 Unit Vectors Used in Describing the Flow for a Curved Darrieus Rotor Blade

The velocity of the air relative to the blade is

$$\vec{W} = \hat{\imath}\, V_t \sin\theta - \hat{\jmath}(V_a + V_t \cos\theta)$$

Transforming the relative velocity to components in blade coordinates, we obtain for the effective relative velocity

$$\vec{W}_e = -(V_t + V_a \cos\theta)\hat{e}_\theta - V_a \sin\theta \cos\gamma \hat{e}_\perp$$

here the spanwise component of the flow has been omitted. Since the lift developed by the blade is in the $W_e \times \hat{e}_B$ direction, it can be shown that

$$\vec{W}_e \hat{e}_L \cdot \hat{\jmath} \equiv W_e \times \hat{e}_B \cdot \hat{\jmath} = -V_t \sin\theta \cos\gamma$$

where $\hat{e}_L$ is a unit vector in the direction of the lift.

A section of blade of length ds in the $\hat{e}_B$ direction develops a lift force dL where

$$d\vec{L} = \frac{1}{2}\rho W_e^2 c C_L \hat{e}_L$$

the streamwise component of this force is

$$d\vec{L} \cdot \hat{\jmath} = -\frac{1}{2}\rho W_e c C_L V_t \sin\theta \cos\gamma$$

As $dz = ds \cos\gamma$, equating the momentum change in a streamtube of dimensions $Rd\theta|\sin\theta|dz$ to the streamwise force generated by a rotor with B blades, we obtain

$$1/2\rho W_e B c C_L V_t \cos\gamma \sin\theta \frac{2d\theta}{\Omega} dz = \rho R d\theta |\sin\theta| dz\, V_a \Delta V \frac{2\pi}{\Omega}$$

The left-hand side of the above equation represents the blade-generated streamwise force while the right-hand side of the above equation is the momentum flux in the streamtube.

Simplification of this equation results in

$$\frac{Bc}{R}\frac{R\Omega}{V_\infty}\frac{C_L}{\pi}\frac{W_e}{V_\infty} = 4a(1-a) \tag{4.2.1}$$

or using the nomenclature of Chapter 2.

$$(C_{T_L})_{\text{Blade}} = (C_{T_L})_{\text{Momentum}}$$

The angle of attack α is given by

$$\tan\alpha = -\frac{W_\perp}{W_\theta} = -\frac{\vec{W}\cdot\hat{e}_\perp}{\vec{W}\cdot\hat{e}_\theta} = \frac{V_a\sin\theta\cos\gamma}{V_a\cos\theta+V_t} \tag{4.2.2}$$

It is to be noted that consistent with strip theory for horizontal axis rotors, the drag force has not been included in the determination of the induced velocities. It may be also remarked that inclusion of drag forces results in a singularity at the $\theta = 0$ and at $\theta = \pi$ stations for Darrieus Rotors since the streamtube width ($dx = R|\sin\theta|d\theta$) at these points goes to zero while the streamwise force does not reach zero when drag is included.

The induced velocity is determined by iteration using equations (4.2.1), (4.2.2), and aerodynamic data for the airfoil in the form $C_L = C_L(\alpha)$.

Once the induced velocity has been evaluated, the torque contributions from lift and drag may be determined. The lift contribution to the torque is

$$dQ_L = d\vec{L}\cdot\hat{e}_\theta R = \frac{R_m^2}{2}\rho V_\infty^2\frac{Bc}{R_m}\frac{W_e}{V_\infty}C_L(1-a)\sin\theta\frac{R}{R_m}dz$$

while the drag contribution is

$$dQ_D = d\vec{D}\cdot\hat{e}_\theta R = -\frac{R_m^2}{2}\rho V_\infty^2\frac{Bc}{R_m}\frac{We}{V_\infty}\frac{C_D}{\cos\gamma}\left[\frac{V_t}{V_\infty}+\frac{V_a}{V_\infty}\cos\theta\right]\frac{R}{R_m}dz$$

Here R_m is the maximum rotor radius.

Thus

$$dQ_{TOTAL} = dQ_L + dQ_D$$

The average torque for a slice of rotor dz in height is given by

$$d\overline{Q}_T = \frac{1}{2\pi} \int_0^{2\pi} dQ_T = \frac{1}{\pi} \int_0^{\pi} dQ_T$$

Since dQ_T varies with θ and the torque is symmetric about the x-axis. The power is given by $\overline{Q}_T\Omega$ or

$$\text{Power} = \Omega \int_0^{z_{max}} \frac{dQ_T}{dz}\, dz$$

where it is to be noted that R = R(z).

4.3 COMPARISON WITH EXPERIMENT

Studies of references 11 and 12 give experimental results for Darrieus rotors with diameters of 12 to 14 feet with one, two, or three blades. The blades used in these studies were NACA 0012 sections having about a 6 inch chord. The resulting Reynolds numbers for the blades were of the order of $3 \cdot 10^5$. References 11 and 12 were used to check the analytical formulations of Templin, Muraca, and Wilson and Lissaman. The later analytical formulation was found to give the best results when compared to the data. Figures 4.3.1 and 4.3.2 present a performance comparison between analytical and experimental results. There still exist notable differences between theory and experiment.

TABLE 4.3.1 Aerodynamic Data Used in Calculation for Figures 4.3.1 and 4.3.2

Maximum Lift Coefficient	0.9
Maximum Drag Coefficient	2.0
Stall Angle	9.21°
Lift Curve Slope	5.6/radian
For Angles of Attack, α less than 9.21°	
Lift Coefficient	5.6α
Drag Coefficient	$0.014 + (8.255 \times 10^{-5})\alpha^2$
For Angles of Attack, α greater than 9.21°	
Lift Coefficient	0.9
Drag Coefficient	$-0.1841 + 0.02912\alpha$

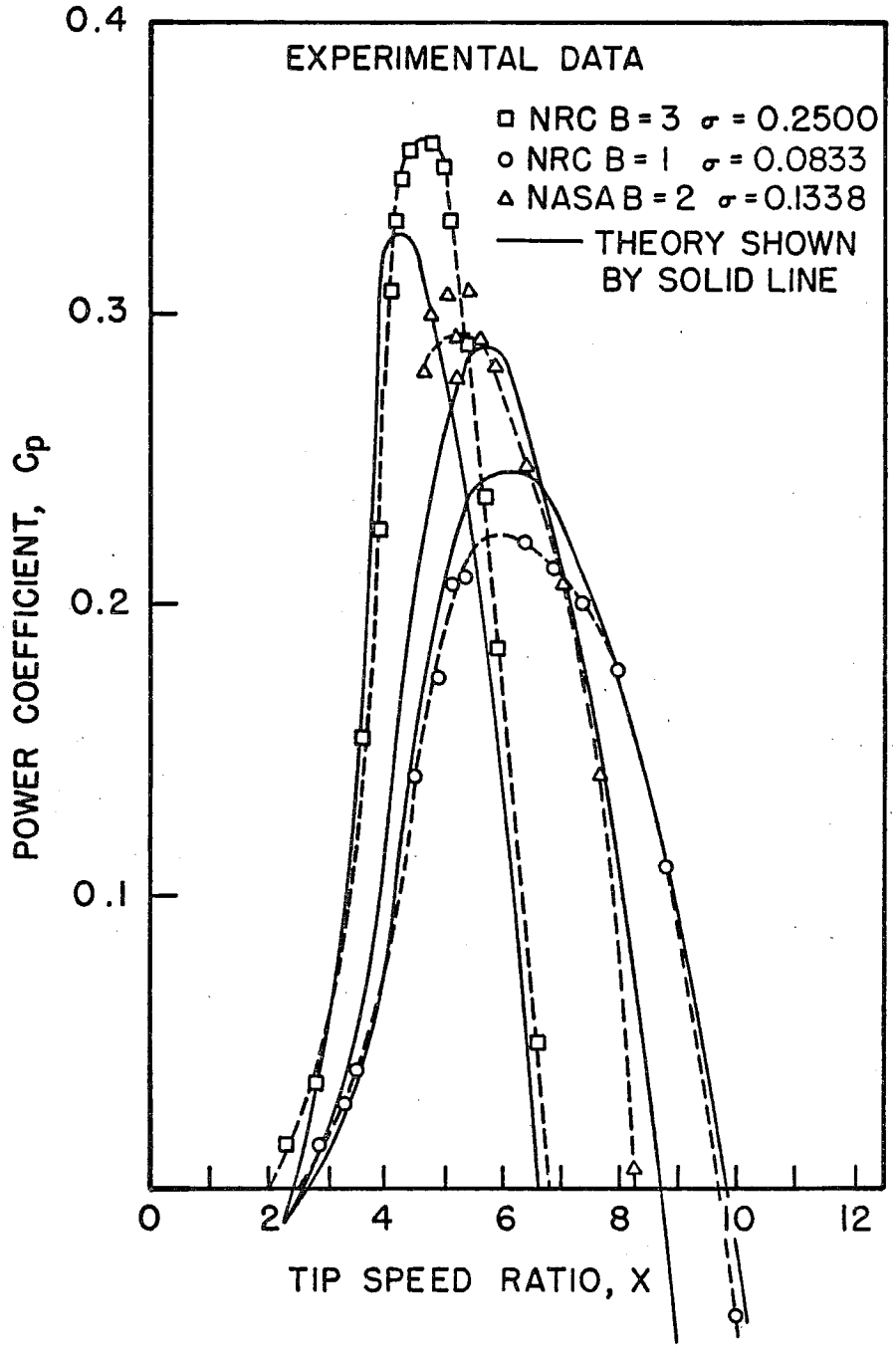

Figure 4.3.1 Comparison of Analytical and Measured Power Coefficients for Darrieus Rotors

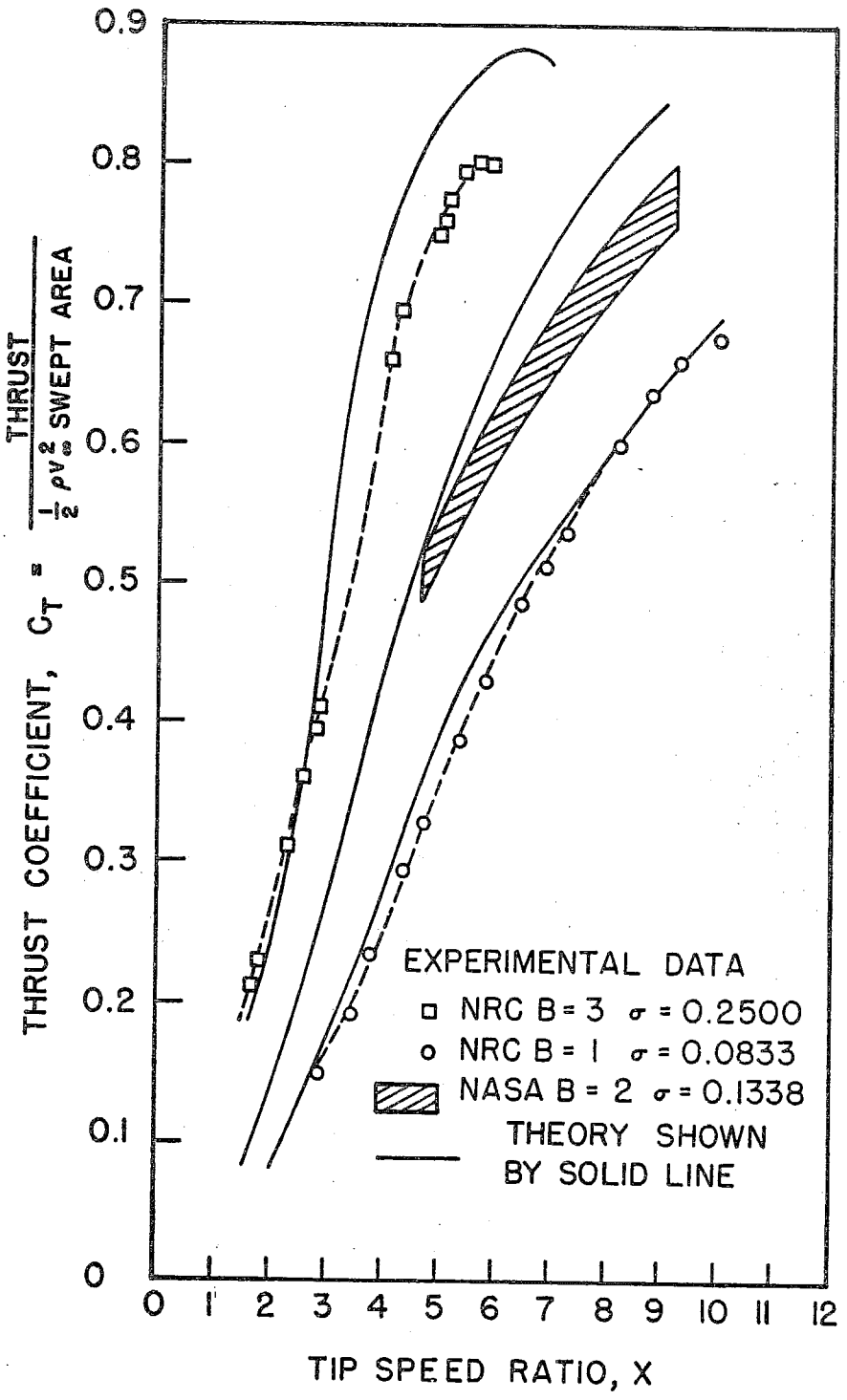

Figure 4.3.2 Comparison of Analytical and Measured Force Coefficients for Darrieus Rotors

Several observations can be made concerning this flow model for the Darrieus Rotor.

1. The flow model predicts a maximum power coefficient which is less than that of an actuator disk (0.593). A closed-form solution for a Darrieus Rotor with circular arc blades and $C_D = 0$ yields $C_{p\ max} = 0.536$.
2. The reduced frequency $(\frac{\Omega c}{2V_{Local}})$ has the same value for all test data used. The value is about 0.04, small enough that the aerodynamics should be quasi-steady unless static stall is approached by the blades. Incorporation of the effects of unsteady lift into the analysis will result in two effects. First, the magnitude of the lift developed will be reduced. This will result in lower predicted performance. Second, the lift will lag the angle of attack. The principle effect of the phase lag is that the rotor will experience a net side force.
3. Test data and theory both show that the three-bladed Darrieus rotor has the most desirable operating conditions, i.e. highest power output and lowest runway speed and almost constant torque.
4. Available test data covers power and overall force measurements only. A complete wake velocity survey has not yet been made by any of the investigators (Muraca[12] made one traverse). Since any aerodynamic theory for Darrieus requires explicit knowledge of the induced velocity, a fundamental piece of information has yet to be obtained.
5. The airfoil pitching moment does contribute to the rotor torque and hence to the power. For a symmetrical airfoil the pitching moment is zero below the stall when the aerodynamic forces can be considered quasi-steady. Above the stall symmetrical airfoils do experience

pitching moments. Because of the symmetry of the flow about the x-axis there is no net contribution of the pitching moment in this flow model. There would be a contribution to the blade loads however.

6. The flow model predicts a near uniform total torque for a three-bladed rotor at high tip speed ratios. However at lower tip speed ratios, the predicted total torque fluctuates considerably. The torque variation is of particular importance when using synchronous operation. Figure 4.3.3 illustrates the total torque as a function of blade position. Note that at a tip speed ratio of 3, there is no longer a near-uniform torque. When using synchronous operation, low tip speed ratios occur at high wind speeds. The character of the stall also has a large effect on the torque variation.

   Figure 4.3.4 illustrates the torque history for one blade of the rotor described in Figure 4.3.3. Again it may be noted that both the tip speed ratios and the character of the stall have a large effect on the predicted torque history.

7. The maximum power coefficient predicted by this flow model is extremely sensitive to $C_{L_{max}}$. The maximum lift coefficient has a large effect on the range of operating tip speed ratios. Figure 4.3.5 illustrates the dimensionless performance of a family of three-bladed Darrieus Rotors for which the maximum lift coefficient varies by 0.1.

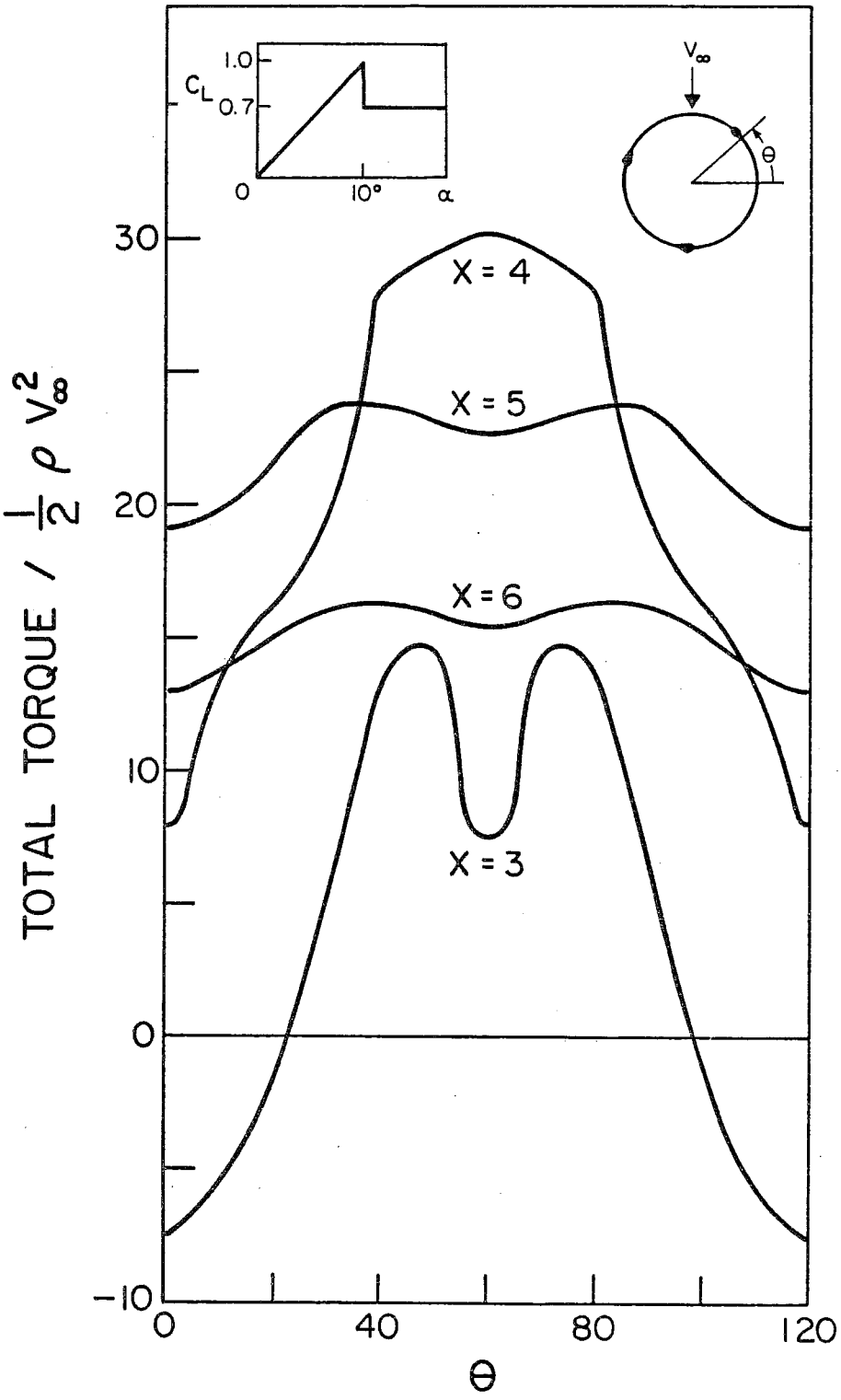

Figure 4.3.3 Rotor Torque vs Blade Position for a 3-Bladed Rotor at Various Tip Speed Ratios. R_{max} = 15 feet, Chord = 1 foot.

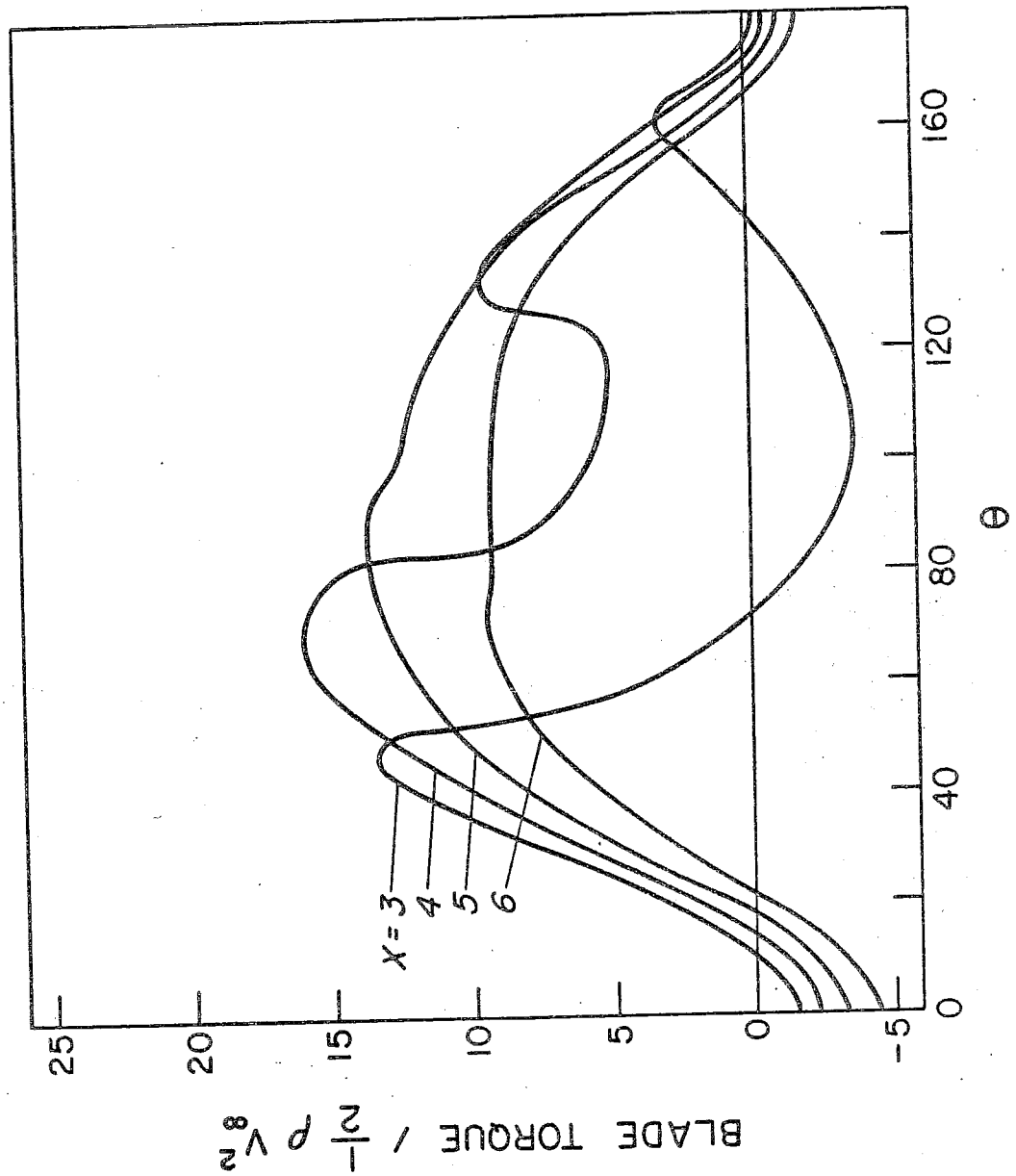

Figure 4.3.4 Blade Torque vs Blade Position for a 3-Bladed Rotor at Various Tip Speed Ratios. R_{max} = 15 feet, Chord = 1 foot.

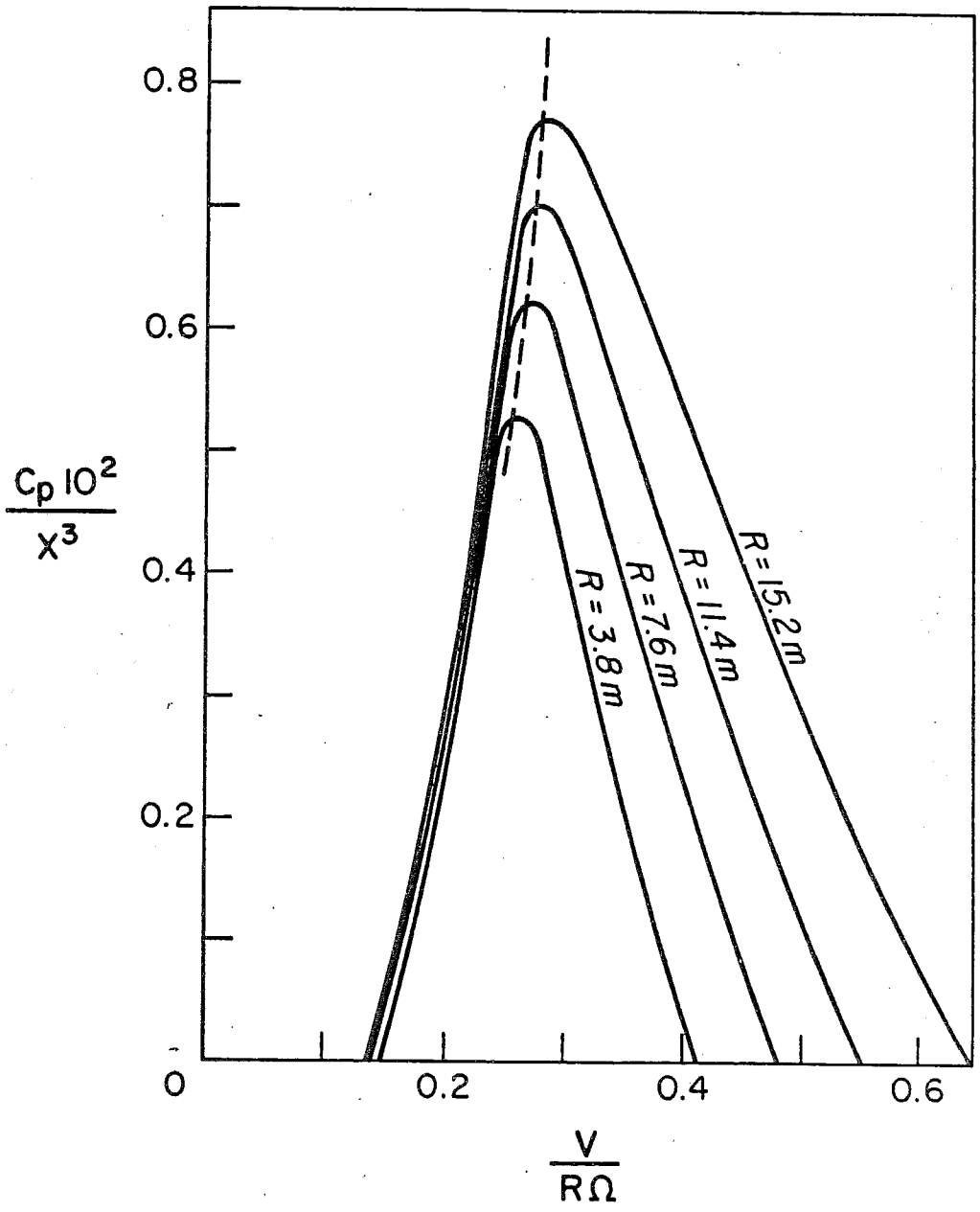

Figure 4.3.5 Dimensionless Power Output of a Family of 3-Bladed Darrieus Rotors. $Bc/R_{max} = 0.25$

4.4 MULTIPLE SOLUTIONS

The iterative solution of Equation (4.2.1) can result in multiple solutions for the Darrieus Rotor just as is the case for horizontal axis rotors. Recalling that equation (4.2.1) can be written in the form

$$(C_{T_L})_{BLADE} = (C_{T_L})_{MOMENTUM}$$

we may graphically illustrate the multiple solutions in the same manner as given in Chapter II.

Figures 4.4.1, 4.4.2 and 4.4.3 show the effects of tip speed ratio, blade solidity and blade position on the blade force equations. The same characteristic lift curve that was used in Chapter II was used to generate these curves.

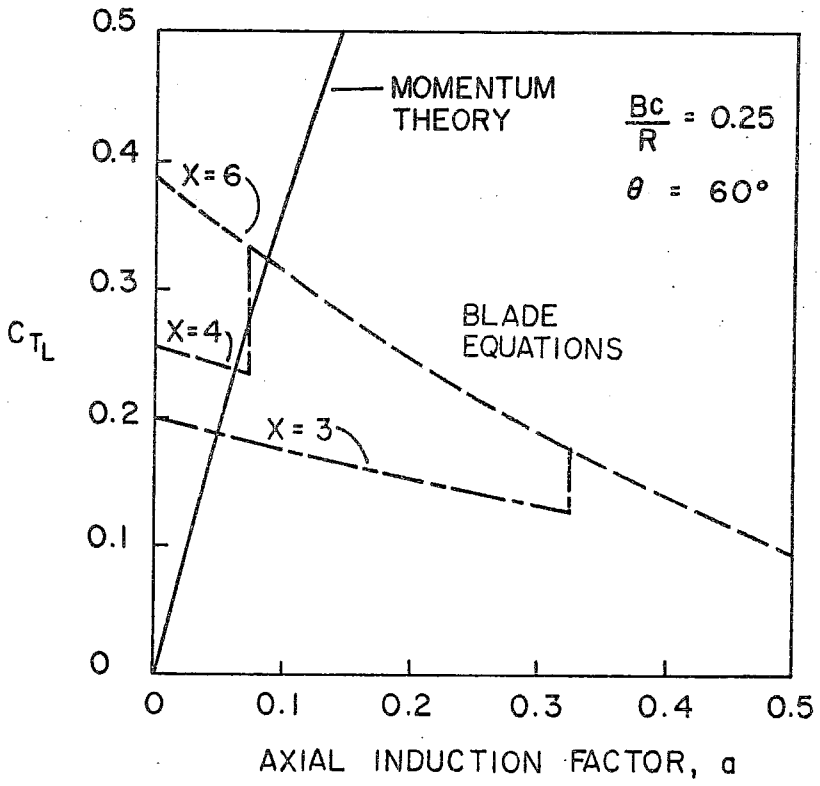

Figure 4.4.1 Effect of Local Tip Speed Ratio

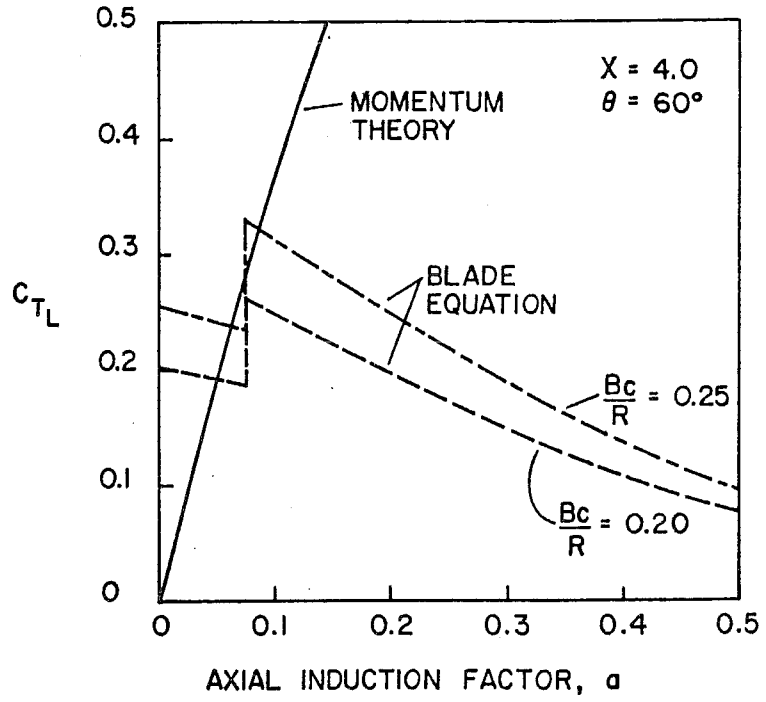

Figure 4.4.2 Effect of Solidity

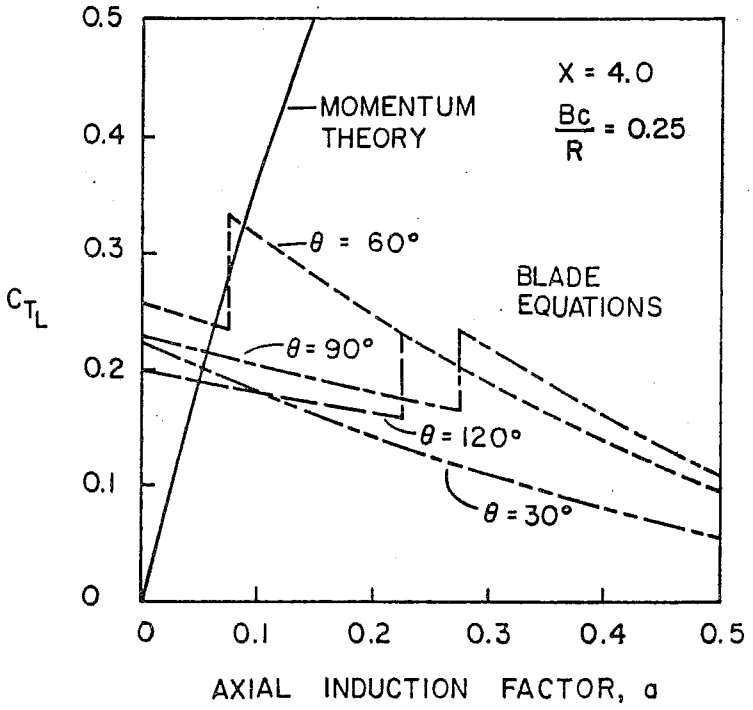

Figure 4.4.3 Effect of Blade Position

REFERENCES

1. South, P. and Rangi, R., "The Performance and Economics of the Vertical-Axis Wind Turbine developed at the National Research Council, Ottawa, Canada. Presented at the 1973 Annual Meeting of the Pacific Northwest Region of the American Society of Agricultural Engineers, Calgary, Alberta, October 10-12, 1973.

2. Darrieus, G.J.M., U.S. Patent No. 1,835,018, December 8, 1931.

3. Wilson, R.E. and Lissaman, Peter B.S., "Applied Aerodynamics of Wind Powered Machines," Oregon State University, May 1974.

4. Templin, R.J., "Aerodynamic Performance Theory for the NRC Vertical-Axis Wind Turbine," National Research Council of Canada, LTR-LA-160, June 1974.

5. James, E.C., "Unsteady Aerodynamics of Variable Pitch Vertical Axis Windmill," AIAA Paper No. 75-649, AIAA/AAS Solar Energy for Earth Conference, Los Angeles, CA, April 21-24, 1975.

6. Muraca, Ralph J., Stephen, S., Maria, V., and Dagenhart, Ray J., Theoretical Performance of Vertical Axis Windmills," NASA-Langley Research Center, NASA TM TMX-72662, May 1975.

7. Shankar, P.N., "On the Aerodynamic Performance of a Class of Vertical Axis Windmills," National Aeronautical Laboratory, Bangalore TM AE-TM-13-75, July 1975.

8. Strickland, J.H., "The Darrieus Turbine: A Performance Prediction Model Using Multiple Streamtubes," Advanced Energy Projects Department, Sandia Laboratory, SAND 75-0431, October 1975.

9. Holme, Olof, "A Contribution to the Aerodynamic Theory of the Vertical-Axis Wind Turbine," Submitted, International Symposium on Wind Energy Systems, Cambridge, England, September, 1976.

10. Blackwell, B.F. and Reis, G.E., "Blade Shape for a Troposkien Type of Vertical-Axis Wind Turbine," SLA-74-0154, Sandia Laboratories, Albuquerque, N.M., April, 1974.

11. South, P. and Rangi, R.S., "An Experimental Investigation of a 12 ft. Diameter High Speed Vertical Axis Windmill," National Research Council of Canada, LTR-LA-166, April 1975.

12. Muraca, Ralph J. and Guillotte, R.J.,"Wind Tunnel Investigation of a 14 ft Vertical Axis Windmill," NASA-Langley Research Center, NASA TM X-72663, March 1976.

CHAPTER V

SAVONIUS ROTOR

INTRODUCTION

The Savonius Rotor was invented by S. J. Savonius of Finland in the early 1920's as a power source to drive Flettner rotors on ships. Savonius soon discovered that his S-shaped rotor developed more propulsive force than the Flettner rotor which generated thrust due to the Magnus effect. His first application of the rotor was to drive a small boat. Since Savonius[1] published his work in 1931 a variety of other applications have been conceived, including exhaust fans, propelling toy ships, and generating electricity. The later use has generated interest to investigate this type of rotor.

The Savonius Rotor has been experimentally investigated by Bach[10], Simonds and Bodek[11], Mercier[12], Newman[7], and others. Because of the large side forces developed by the Savonius Rotor, wind tunnel test results must be viewed with caution.

Wind tunnel testing of Savonius Rotors requires a much larger ratio of tunnel area to rotor area since the wake experiences large crosswind forces as well as moderate windwise forces.

In this chapter, the flow field is described and an analytical model is developed for performance analysis of this rotor. This is the first time the analysis of the Savonius Rotor has been presented.

5.1 DESCRIPTION OF FLOW FIELD

From the global point of view the operation of a Savonius type rotor is like that of any other windmill device. The free stream flow (or wind) produces an aerodynamic force on the rotor blading and this blading moves with at least some component of the aerodynamic force in the direction of motion. Thus work is done on the machine and energy extracted from the flow. This energy extraction is associated with change in total head of portions of the flow, which is always kinematically realized by the generation of vorticity. This is expressed in its most basic form by Crocco's Equation.

$$\vec{V} \times \vec{\Omega} = \nabla H - T\nabla S + \frac{\partial \vec{V}}{\partial t}$$

Here $\vec{V}$ is the local velocity vector, $\vec{\Omega}$ the vorticity, H the total energy or stagnation enthalpy, T and S the temperature and entropy. This indicates that, neglecting viscosity and heat conduction, vorticity must always be in the flow field when the distribution of total energy H or the entropy S is non-uniform. It is also of interest to observe that for this condition the vorticity, $\vec{\Omega}$, cannot be parallel to the local flow, $\vec{V}$. This vorticity appears in the form of discrete vortices, of vortex sheets, and of regions of distributed vorticity. The vorticity will extend downstream and will manifest the kinematics defining the forces on the rotor, and the power extracted from the flow.

For the specific case of the Savonius type rotor there is always a significant unsteady flow component. This is in distinction to some other types where, although unsteady flows always occur, the effects of the unsteadiness may be sufficiently small that a steady or quasisteady

approach can be used for analysis. To illustrate these effects we discuss and describe the actual flow as illustrated by motion picture records of flow in one type of Savonius machine.

The motion pictures[2] (Figure 5.1.1) show smoke streak lines of a Savonius rotor operating at zero power coefficient at a free stream speed of about 32 ft/sec, a Reynolds number, based on free stream speed and rotor total diameter, of about .094 million and a tip speed ratio of about 1.64. The flow is from left to right and the rotor turns in a clockwise direction. In analyzing these photographs it must be clearly recognized that the smoke lines are streak lines, and as such are not parallel to the streamlines of the flow, nor is their spacing inversely proportional to the flow velocity as would be the case with streamlines. We will refer to the blade on the left in frame 1 as vane 1, the other as vane 2, with the outer edge as the tip. We will define vorticity in the same sense as the rotation (clockwise) as positive vorticity.

The frames have been printed directly from a positive motion picture, that is areas shown dark in the figures are in reality light, and the real smoke was white against a dark background. The rotor end plate is indicated by a dark circular ring of larger radius than the vanes, while the rotor support shaft is the light bar extending upwards from the rotor axis at 10 o'clock radial position.

From frame 1 through frame 22 we note that there is apparently attached flow on both the convex and concave faces of vane 1, while vane 2 appears to show separation on its convex face. At frame 22 we observe the beginning of vorticity shedding from the tip of vane 1 developing into a positive vortex near the tip of vane 1 in frame 29. It appears

that the vortex shedding on vane 1 begins when the dividing streak line (corresponding to the stagnation streamline in steady flow) reaches the tip of this vane in frame 23. Vane 2 appears to show distinct separated flow on its concave face in frames 20 through 32.

By frame 43 the vorticity shed from vane 1 has organized itself into a "free" vortex and is proceeding downstream at a distinct downwash angle and, taking this downwash into account at approximately the tip radius separation of vane 1 in frame 25. It will be noted that the flow picture has returned to that of frame 1, with vane 2 in the position of vane 2.

The process of vortex shedding from the advancing blade (vane 2) is not as easy to determine. In frames 2 through 7 we observe the formation of an indistinct region of smoke on the forward portion of convex face of vane 2. This appears approximately fixed with respect to the observer, that is it seems to move backwards along the vane with time until it appears to join with the flow on the concave face of vane 2 at frames 19 through 21. What appears to be a negative vortex (possibly also containing low energy separated flow) can be seen in frames 29 through 39. This vortex is best identified by the cusp like streak line in frames 30 through 34. This cusp appears near the edge of the rotor end plate on an imaginary line which is the extension of the rotor support strut. This cusp can be seen to move downwards and backwards, with its predecessor near the bottom of the picture in frames 1 through 19.

It is of interest to note that the motion picture appears to indicate a non-uniform rotational speed in the vicinity of frames 4 through 7 where the rotor speed seems to have significantly slowed down.

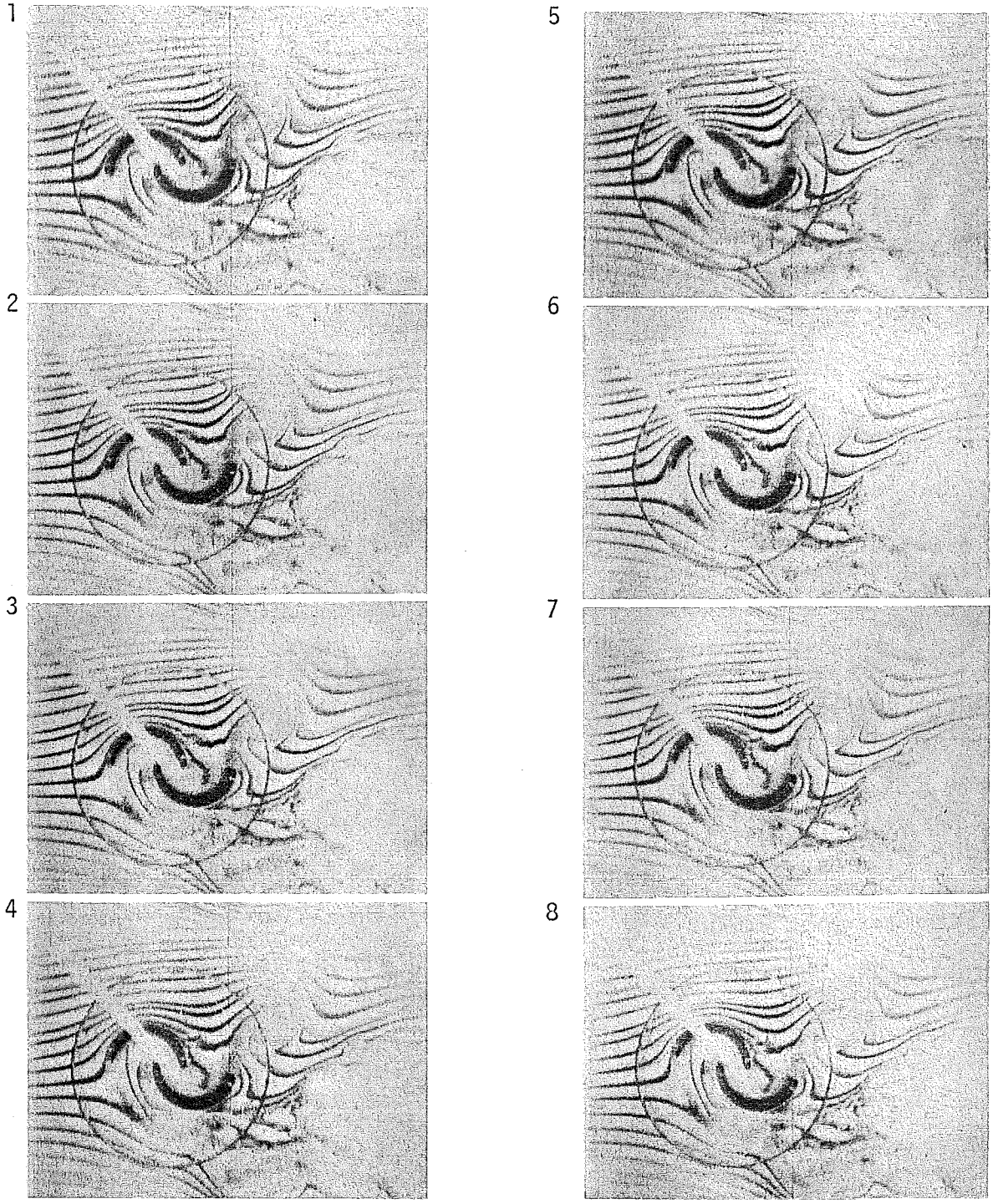

Fig. 5.1.1 Flow Field of Savonius Rotor. Frames 1-8.

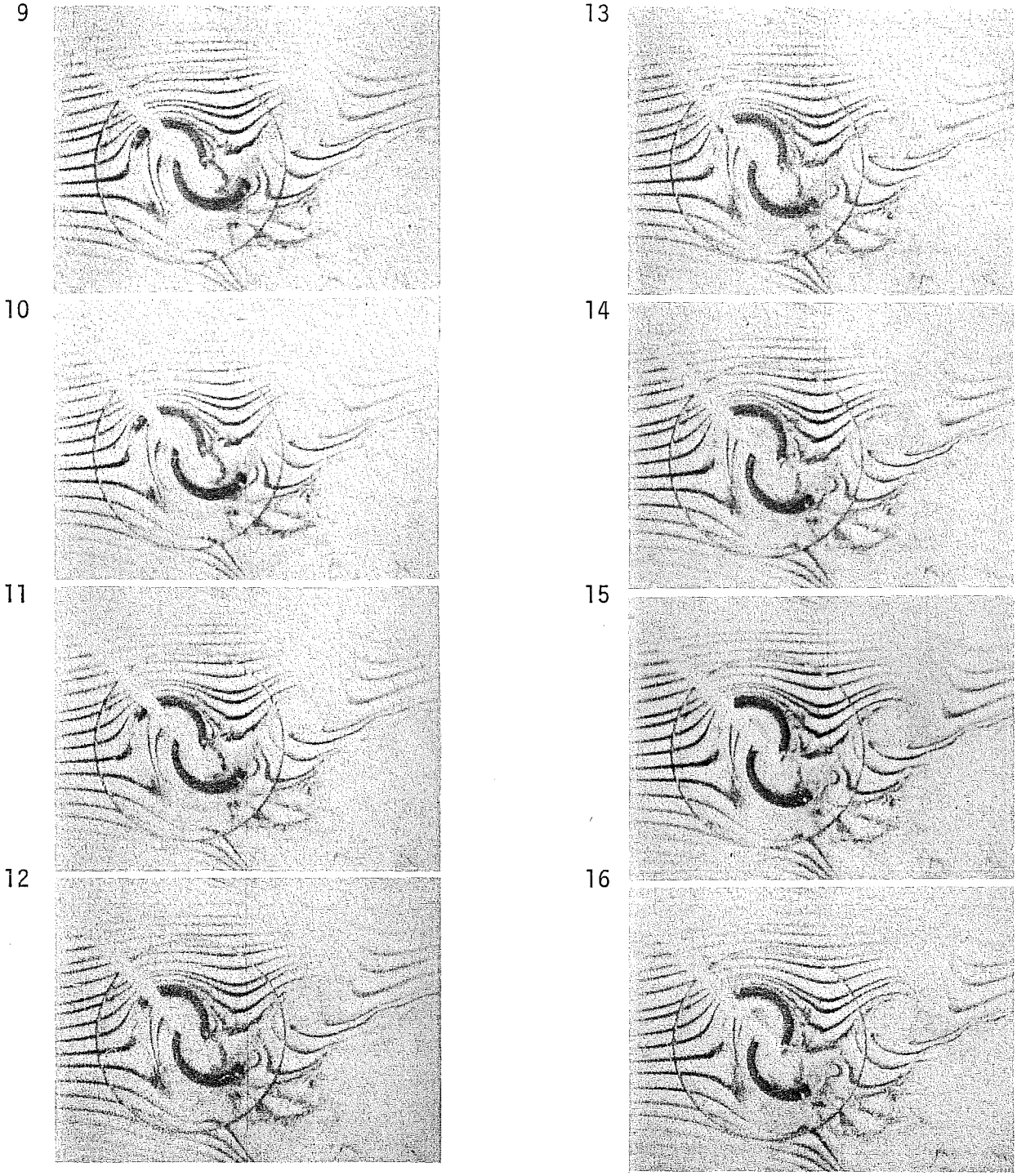

Fig. 5.1.1 (cont.). Flow Field of Savonius Rotor. Frames 9-16.

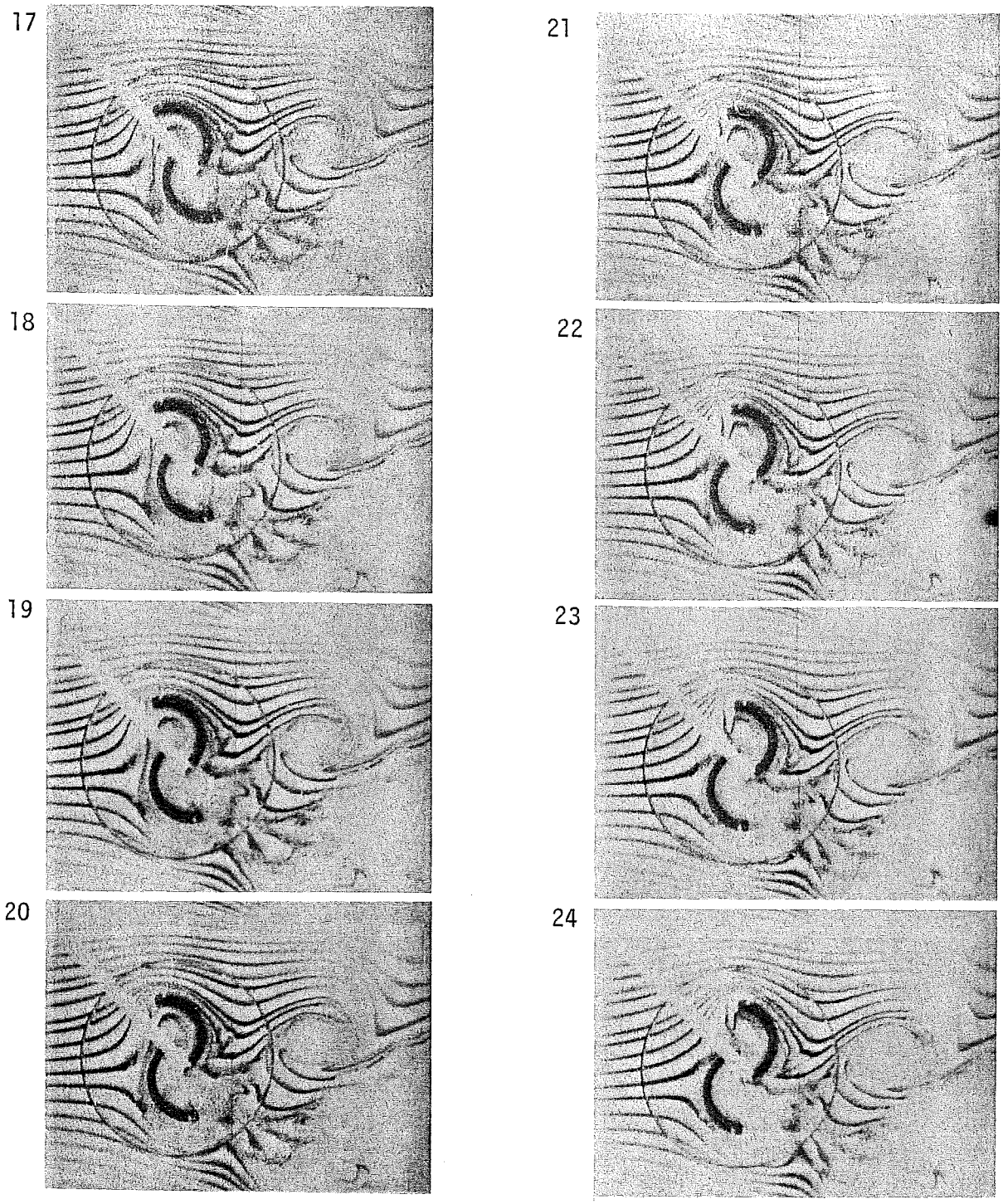

Fig. 5.1.1 (cont.) Flow Field of Savonius Rotor. Frames 17-24.

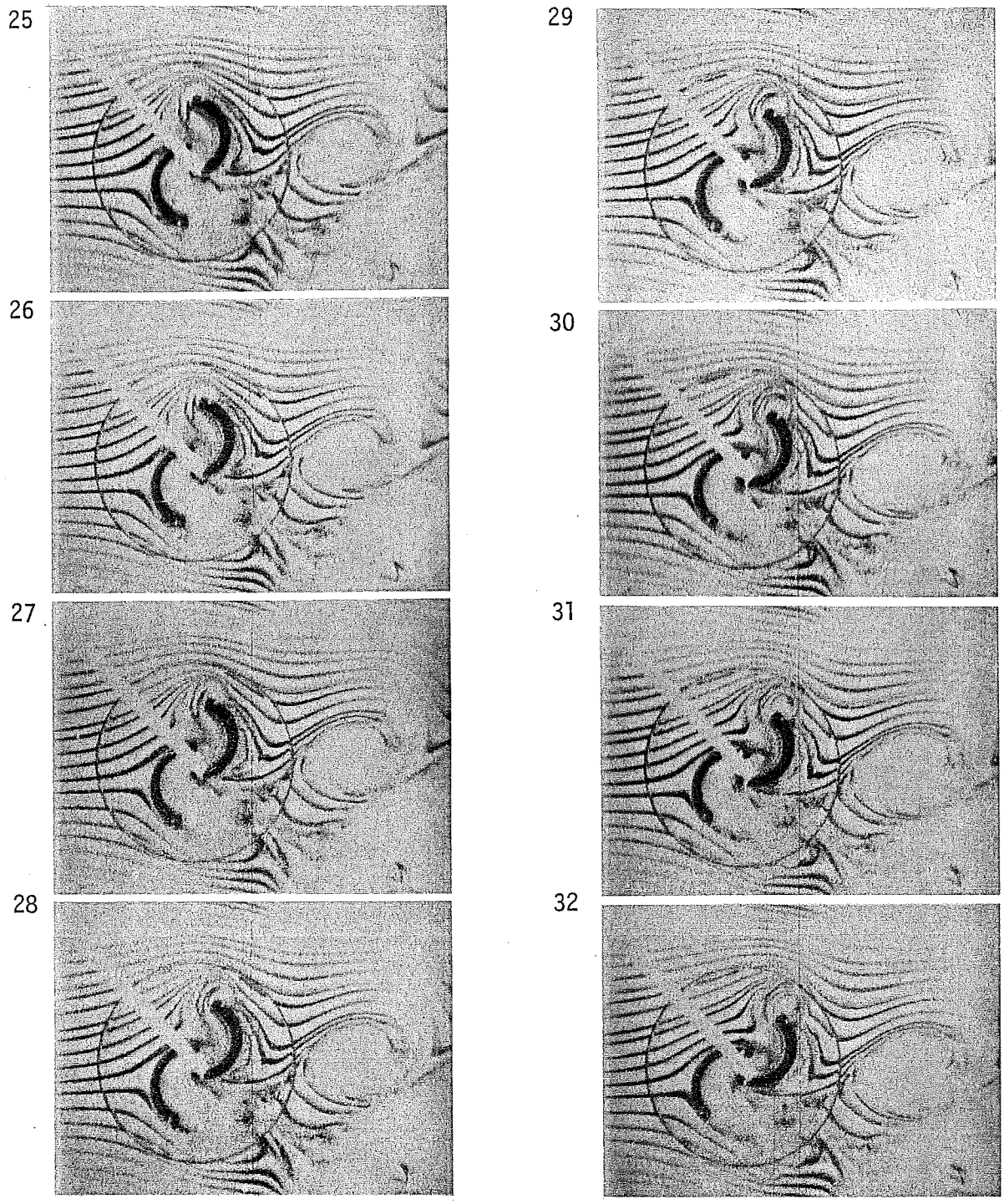

Fig. 5.1.1 (cont.) Flow Field of Savonius Rotor. Frames 25-32.

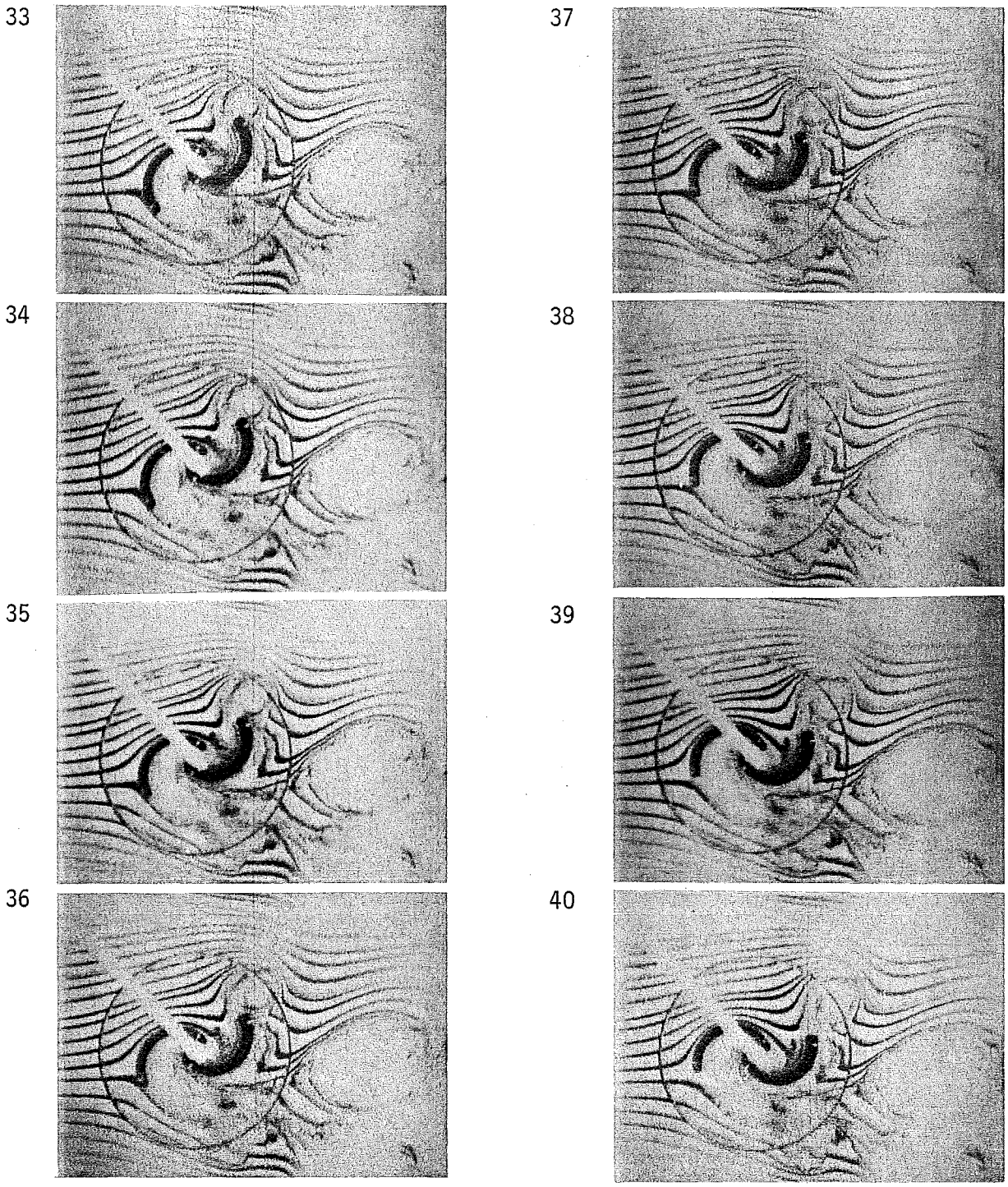

Fig. 5.1.1 (cont.) Flow Field of Savonius Rotor. Frames 33-40.

41

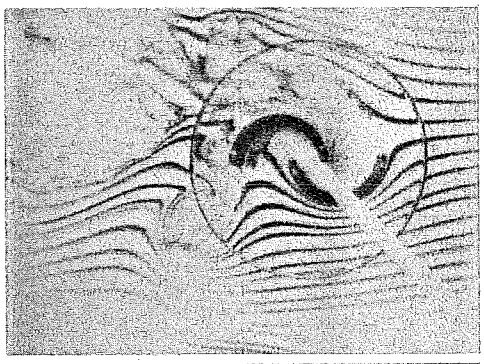

42

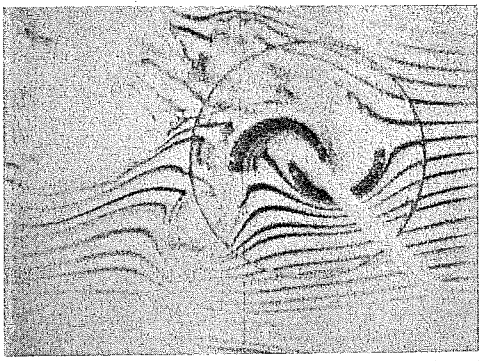

43

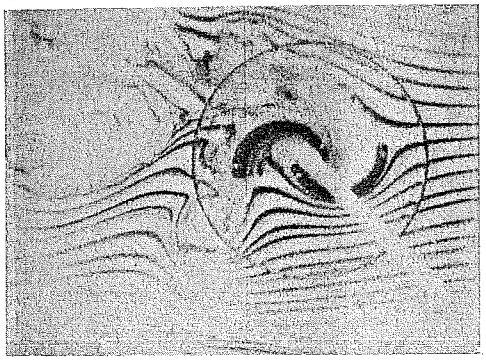

Fig. 5.1.1 (cont.) Flow Field of Savonius Rotor. Frames 41-43.

The flow system described above is very helpful in constructing a rational flow model for analysis. The major discernible features are reiterated below:

1) Distinct vortices are shed from the vane tips when the vane is approximately at right angles to the flow.
2) These vortices are counter rotating with the one from the retreating vane rotating in the same sense as the rotor itself.
3) The shed vortices move rearward at approximately free stream speed, with a distinct downwash associated with bound vorticity of the same sense as the vane rotation.
4) There appears to be attached flow on both sides of the retreating vane.

Other features of the flow are less easy to specify definitively. Unfortunately, the movie frame does not show far wake details and extends only about two rotor diameters downstream. Thus the nature of the vortex shed from the advancing vane is not recorded since due to the downwash it occurs below the movie frame. This would be of particular interest since it is in this vortex that any large separation regions might be expected to occur.

Thus tentative conclusions which can be drawn are:

1) There appears to be a separated flow on both sides of the advancing vane when it is approximately normal to the flow.
2) This separated flow is apparently shed as a bubble and contains the vortex shed from the advancing blade.
3) The advancing blade vortex apparently contains a region of low energy flow, which extends towards the wake centerline as the vortex moves downstream.

A number of questions are raised, which cannot be answered by the existing photographs. These questions are posed as very worthwhile research topics for future flow visualization work.

1) Does the character of the flow change with tip speed ratio? Particularly, what is the flow picture at the tip speed ratio corresponding to maximum power?

2) What is the nature and location of the flow separation?

3) If the vortices are shed approximately simultaneously from top and botton vanes, are they unstable as they proceed downstream as would be expected from Von Kármán's[3] analysis?

4) It is believed that the flow shown in the movies was for zero power coefficient. Does this imply that the flow is non-representative of power generating states and that it contains larger regions of low energy flow than would occur under maximum power extraction?

5.2 INVISCID ANALYTICAL MODEL

5.2.1 Discussion of Analytical Model

It is evident that the flow field which must be analyzed is certainly unsteady and cyclic, and probably also separated in certain tip speed ratio ranges. We will treat this with a potential analysis, which will thus ignore any separation effects.

Even the potential analysis involves serious theoretical difficulties which relate to assumptions concerning the flow near the rotor tip, and the induced flow of the shed vorticity. We will first discuss the tip flow.

For simplicity in the model we have considered a two vaned rotor with no center gap, that is it is an S shaped airfoil of zero thickness, with camber antisymmetic about the half chord, and rotating about the half chord. We will call the extremities (the outer edges) the tips, and note that there are no grounds for them to be either leading or trailing edges. There is no apriori reason to assume a Kutta condition (no flow around the trailing edge) occurs, and thus no method of establishing a circulation.

If we assume that all details of the external flow (that is the induced wash and any wake vorticity) are known, then the kinematic boundary conditions are uniquely defined and in principle we can determine an exact potential flow solution for the rotating vane. However, there is a circulatory potential solution which also matches all kinematic boundary conditions on the rotor, which can be added like a homogeneous solution to any selected solution. This homogeneous solution can really only be determined by boundary conditions at infinity, where it produces a pertur-

bation similar to that of a point vortex, thus it dictates the circulation about the rotor. Thus the unsteady solution can be determined subject to a circulatory solution of arbitrary magnitude.

In classical airfoil theory, this ambiguity is resolved by a local condition, namely the application of the Kutta condition to flow at what is arbitrarily defined as the trailing edge of the airfoil. Under normal conditions of steady flow, rounded leading edge, sharp trailing edge and representative viscosity, the application of the Kutta condition to the trailing edge gives excellent correlation with experiment.

In the case of the Savonius rotor conditions are quite different. First we note that with unsteady flows it is possible to have a noncirculatory potential flow with flow around sharp edges - however this flow exists for a very short time and is followed by vortex shedding from these sharp edges although the flow remains potential with no separation of the type associated with a low energy wake. It is not clear how long the non-circulatory flow exists, but theoretical calculations (Hunt[4]) suggest that, for sharp edges, vortex shedding commences immediately. Now, it is possible to add a circulatory component to the solution which will eliminate flow around one or the other tip, but a Kutta condition on each tip cannot be achieved unless there is a special distribution of vorticity in the wake. However, it is always possible to satisfy the Kutta condition at a tip if vorticity is shed into the stream.

This technique was used by Kármán and Sears[3] in their classic paper on unsteady airfoil theory. In their case, a single trailing edge was defined by the airfoil geometry, and this edge was considered a source of vorticity flux into the stream. Now, subject to various vorticity conser-

vation and convection laws, and the assumption that there is never flow around the trailing edge (Kutta) it becomes possible to uniquely define the unsteady circulation. It would be possible to apply the Kármán-Sears methodology to our problem with the basic assumption that Kutta condition must be satisfied at both tips of the rotor, and that vorticity is shed from these tips to maintin this flow. This approach is much more complicated than can be treated here. The approximation used here is consistent with the approximation for wake vorticity and we will describe it after discussing the wake vorticity or induced flow models.

It is well known for propeller-type rotors that the drag on the disc is represented by a reduction in wind speed through the rotor, known as axial interference, or drag induced flow.

For propeller rotors and for crosswind axis machines of the Darrieus type, this can be represented as a uniform steady flow, at least in an annulus, or in a "slice" for the crosswind axis machine. The implication here is that the rotor develops a wake of dimensions comparable to the swept frontal area, and that this wake is steady and bounded by a vortex sheet shed from the rotor. Conditions necessary for this to be a good assumption are that product of the number of blades and the tip speed ratio should be large.

For the two-vaned Savonius rotor neither of these conditions are satisfied so that the wake cannot strictly be represented by a pair of vortex sheets of uniform strength and separation. In fact, the vortex shedding is cyclic and the positions from which vorticity is shed vary so that the wake varies both in width and vorticity. We note that this is one degree more complicated than the Kármán-Sears analysis, where the

wake varies in strength but not in lateral (crosswind) position. In the actual case of the Savonius, the wake is apparently of approximately sinusoidally varying width, with vortex sheet strength also approximately sinusoidal with maximum strength at greatest wake width. Recognizing the complexity of computing the spatially varying induced field due to such a system and the further complication of consistently matching this vorticity to the vane shedding and the induced flows to the kinematic vane boundary conditions we assume as a first approximation that the wake can be treated like a vortex tube of constant strength and rectangular cross section.

On this basis the induced flow will be uniform across the vane, and the vane will respond as though it were in a stream of reduced velocity $V_\infty(1-a)$ where V_∞ is the free stream velocity and $\underline{a}$ the windwise induction ratio. This stream will also be deflected in a crosswind direction associated with the crosswind or lift force on the vane.

Subject to this assumption, we now note that it will be impossible to meet Kutta conditions at both of the vane tips since only a single circulation variable is available. On this basis, the most rational choice of circulation is that which simultaneously minimizes the flow around both tips.

Thus, for the analysis of the following section we have initially used the most simple rational model. This model is sufficient to reproduce the main observed characteristics of the Savonius rotors.

5.2.2 Description of Potential Functions

Before embarking on the mathematical analysis it is useful to describe the nature of the three potential functions employed in the theoretical solution. If we consider a vane in the position shown, Figure 5.2.1, we note the three velocity components which specify the kinematic boundary conditions. Potential functions satisfying each of these can be defined and we describe them as ϕ^n, that due to flow normal to the vane $V_\infty(1-a)$ sin ϕ, ϕ^c that due to flow across the vane $V_\infty(1-a)$ cos θ and ϕ^Ω that due to the rotation induced velocity, Ωr.

We show the character of the potential and distributed vane vorticity in order to illustrate the contribution of each component.

The potential is shown in Figure 5.2.2, the distributed vorticity in Figure 5.2.3. We note that the local pressure force is related to the time derivative of ϕ, ϕ_t and to the spatial derivative ϕ_r, which is directly proportional to the local vortictiy.

First we note that the ϕ^n, ϕ^c vorticity components will generally produce flow around the tips. However the arrangement shown actually minimizes the net total tip flow since any additional circulatory component will reduce flow around one tip but increase it at the other.

We note that ϕ^n, ϕ^c produce torque moments, but no net lift, while ϕ^c produces a lift without any moment. It is noted that ϕ^Ω does automatically satisfy a Kutta condition at each tip, also that there always exists an angle of the vane at which the tip Kutta condition is satisfied. This angle corresponds to the ideal angle when the rotor is treated as a cambered airfoil, and is independent of the angular velocity.

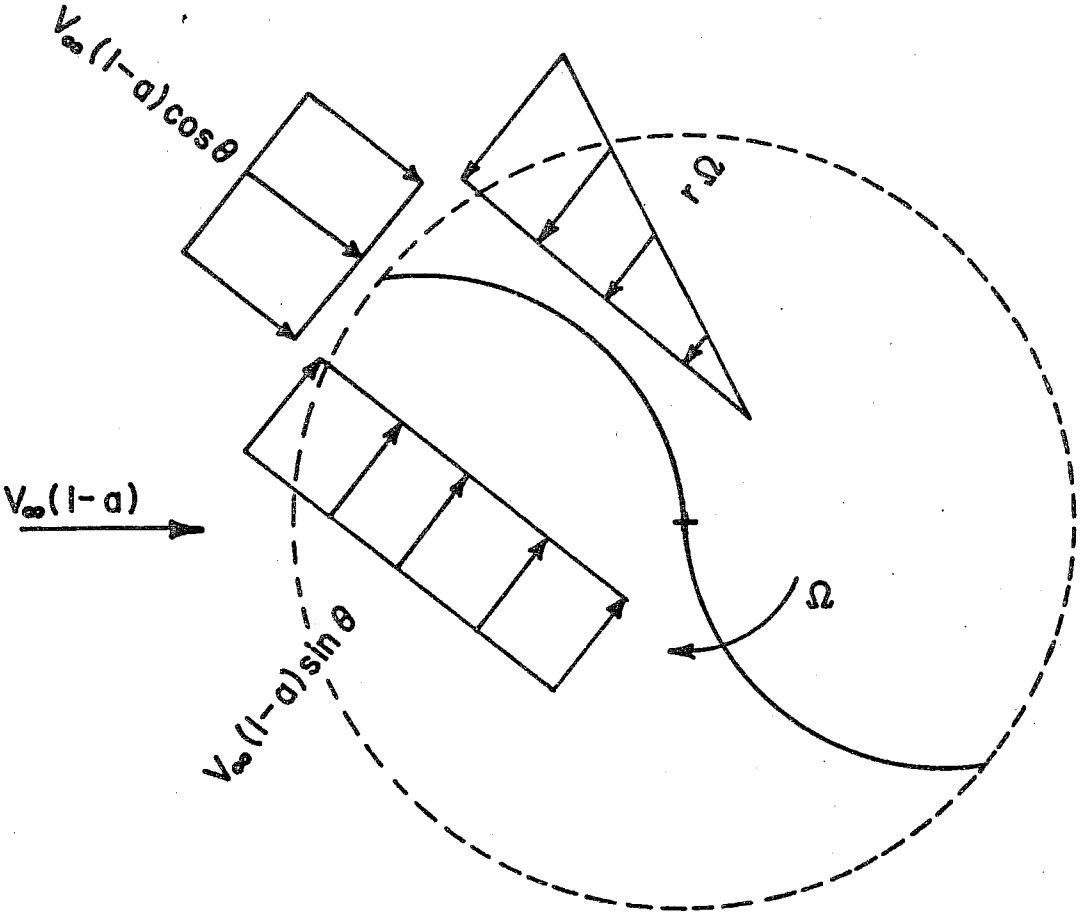

Figure 5.2.1 Components of Flow Defining Kinematic Boundary Conditions

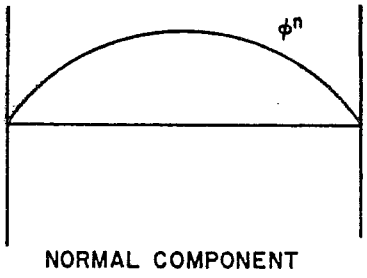

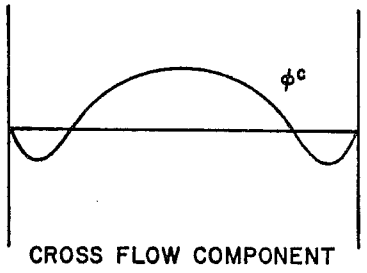

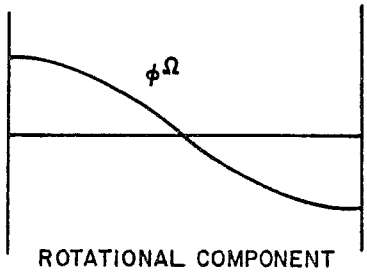

Figure 5.2.2 Vane Potential Distribution for Each Flow Component

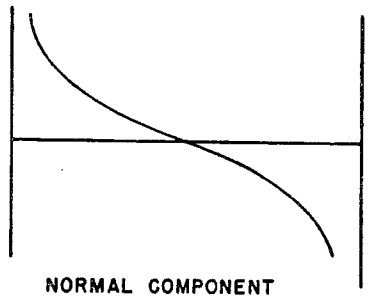

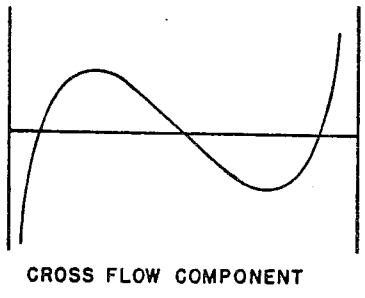

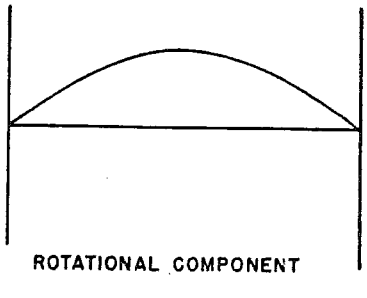

Figure 5.2.3 Vane Vorticity Distribution for Each Potential Component

It is also noted that there is a circulation developed on the rotor, which is independent of rotor angle and vane camber and is related linearly to the angular velocity Ω. Thus, in this model the circulation remains constant throughout the cycle. However, this does not imply that the lift is constant through the cycle since unsteady terms contribute to the total lift, causing it to be different from that implied by the vane circulation alone.

5.2.3 Potential Analysis for Two-Dimensional, Uniform Wake Model

Consider the geometry of Figure 5.2.4. We have a two-vaned rotor of radius R and angular velocity Ω in a stream of uniform velocity $V^* = V_\infty(1-a)$. The rotor has antisymmetric camber defined by $C = \beta Rf(r)$ where r is the radius position normalized by the outer radius R. The non-dimensional term β now plays the same role as blade angle of attack. Then, assuming we have a perturbation potential given by $V^*R\phi(r,t,\theta)$ we see by linearized theory that the normal derivative of this potential is given by

$$V^*\phi_n = V^*\sin\theta + V^*\cos\theta\ \beta\ f' - \Omega Rr$$

We now write ϕ as

$$\phi = \phi^n \sin\theta + \beta\,\phi^c \cos\theta - X^*\phi^\Omega$$

where X^* is the <u>local</u> tip speed ratio $\Omega r/V^*$.

where each potential is identified through its inner boundary condition, (B.C.), as follows

ϕ^n is the normal potential with B.C. $\phi^n_n = 1$

ϕ^c is the camber potential with B.C. $\phi^c_n = f'$

ϕ^Ω is the rotational potential with B.C. $\phi^\Omega_n = r$

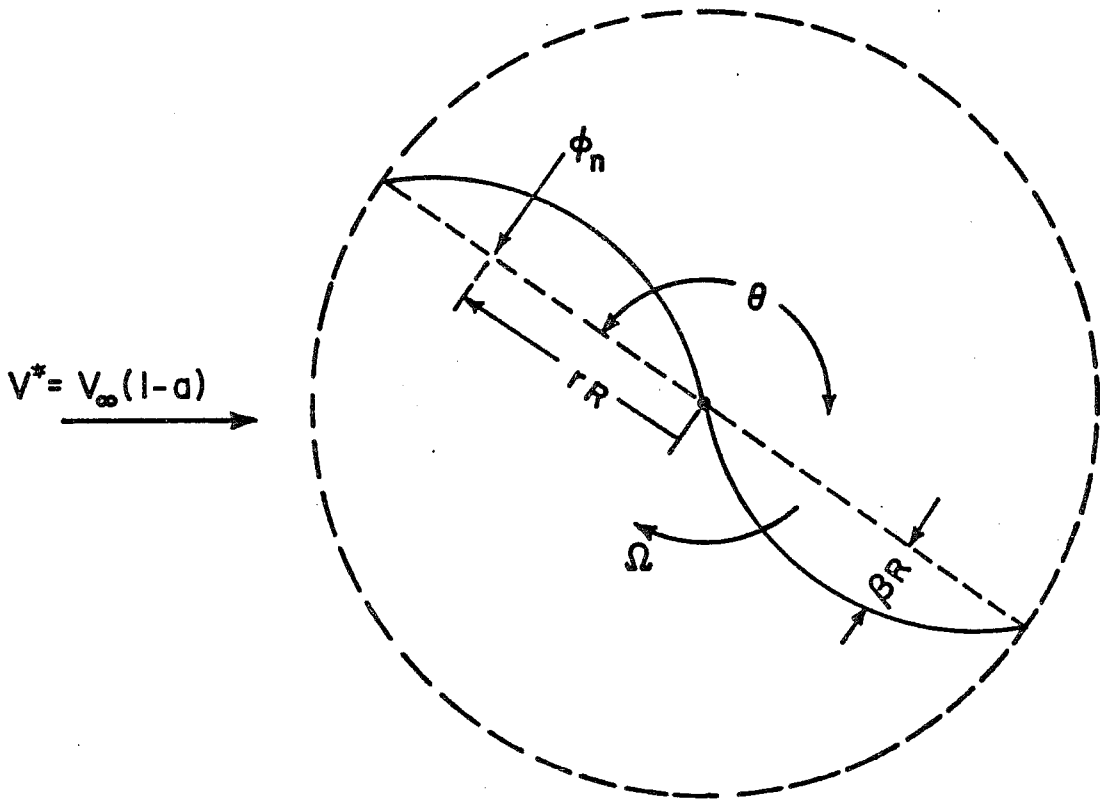

Figure 5.2.4 Geometry of Two-Vaned Rotor

We now note that in an unsteady coordinate system rotating with the vane we can write the net pressure coefficient on the vane

$$C_p^* = -\Delta p/1/2\ \rho V^{*2} \quad \text{as}$$

$$C_p^* = + 4\ (\phi_r \cos\theta + X^* \phi_\theta)$$

From this we can calculate loads on the rotor.

TORQUE

The local torque on an element is given by

$$q = 1/2\ \rho V^{*2} R^2\ C_p^*\ r\ dr$$

While the mean torque Q of both values is given by

$$Q = \frac{\rho V^{*2} R^2}{2\pi} \int_0^1 \int_0^{2\pi} C_p^*\ r\ d\theta\ dr$$

Defining the torque coefficient as

$$C_Q^* = Q/(\rho V^{*2} R^2)$$

we get

$$C_Q^* = 2\beta \int_0^1 \phi_r^c\ r\ dr$$

We can identify ϕ^c in a simple fashion, according to steady aerodynamics. If we consider the case of $X^* = 0$, $\theta = 0$

$$C_{Q_o} = 4\beta \int_0^1 \phi_r^c\ r\ dr$$

But, if we take the vane as a reflexed airfoil of chord 2R we see

$$C_{Q_o} = 2\ C_m$$

Where C_m is the pitching moment of the airfoil at zero lift about the mid chord. Since it is at zero lift, it can also be identifed as C_{m_o}, the pitching moment about the quarter chord. Thus we obtain the interesting result

$$C_Q^* \equiv C_m = C_{m_o}$$

and

$$C_m = 2\beta \int_o^1 \phi_r^c \, r \, dr$$

DRAG

The local drag is given by

$$D = 1/2 \, \rho V^{*2} R \, C_p^* \, dr \sin\theta$$

while the mean drag D of both vanes is given by

$$D = \frac{\rho V^{*2} R}{2\pi} \int_o^1 \int_o^{2\pi} C_p^* \sin\theta \, d\theta \, dr$$

Defining the drag coefficient $C_D^* = D/\rho V^{*2} R$ we get

$$C_D^* = 2\beta \, X^* \int_o^1 r \, \phi_r^c \, dr$$

$$= X^* \, C_m$$

LIFT

Similary, the lift is given by

$$C_L^* = 2 \, X^* \int_o^1 (\phi_r^\Omega + \phi^n) dr$$

We now note from the boundary conditions that $\phi_r^\Omega = \phi^n$

Thus

$$C_L^* = 4X^* \int_o^1 \phi^n \, dr$$

5.2.4 Comparison with Basic Power Extraction Theory and Global Results

If we now assume a two-dimensional rotor, so that there is no wake deflection

$$C_D^* = 4a/(1-a) = X^* C_m$$

Now we can write the power coefficient based on $\rho V_\infty^2 R^2$ and the conventional tip speed ratio $X = \Omega R/V_\infty$ as

$$C_p = X\, C_Q (1-a)^2$$

$$C_p = X\, C_m (1-a)^2 \quad \text{but } X^* = X/(1-a)$$

But $XC_m = 4a$ from first equation above

Thus $C_p = 4a(1-a)^2$ recovering the well known result for power coefficient under conditions of uniform induced wake flow. We note that we can write C_p as

$$C_p = X\, C_m \left(1 - \frac{XC_m}{4}\right)^2$$

Next considering the lifting term, C_L, we note that the only potential with circulatory component is ϕ^Ω and that the circulation, Γ, is constant given by

$$\Gamma = 4V^* R \int_0^1 X^* \phi_r^\Omega \, dr$$

$$\Gamma = 4V^* RX \int_0^1 \phi_r^\Omega \, dr$$

$$\Gamma = 4V^* RX^* \int_0^1 \phi^n \, dr$$

But applying the Joukowsky theorem $L = \rho V^* \Gamma$ we get

$$C_L^* = 4X^* \int_0^1 \phi^n \, dr$$

which is an explicit representation of the well known Magnus effect and recovers the result from direct integration.

Now noting that $\phi^n = \sqrt{1-r^2}$ we get

$$C_L^* = X^* \pi$$

so that $C_L^*/C_D^* = \pi/C_m$.

Thus we determine the circulation Γ to be given by $\Gamma = V^* R C_L$.

If we express this in terms of the tip speed V_t, we obtain

$$\Gamma = V_t \pi R$$

This result is interesting since for a rotating circular cylinder, assuming the no slip condition we would get $\Gamma = 2 V_t \pi R$. This may be expected to be the result obtained for an infinite number of vanes. Thus, based on this assumption we note that the two-vaned rotor develops half the circulation associated with an infinite number of vanes.

It is also of interest to observe that although the circulation is constant throughout the cycle, the lift is not, varying from a maximum at $\theta = 0$ to zero at $\theta = \pi/2$ such that the mean lift per cycle is given by $\rho V^* \Gamma$.

It is shown in the next section that for typical antisymmetric camber shapes the pitching moment is given approximately by $\pi\beta$. Thus

for $\beta = 1/2$, corresponding approximately to semicircular arc vanes we get the lift to drag ratio given by

$$C_L^*/C_D^* = 1/\beta = 2.$$

This indicates that the crosswind force on the Savonius rotor is larger than the windwise force.

5.2.5 Pitching Moment of Vane

For the vane shape it is a simple matter to compute the pitching moment if linear theory is used. It is certainly true that the magnitude of camber of the vane is such that slopes are not small enough to justify, á priori, the accuracy of linearized theory. However it is a matter of interest that linearized theory gives excellent accuracy for thin airfoils of large camber. For example, the lift coefficient at zero angle of attack for a parabolic arc is given by linear theory as $4\pi\beta$, where β is the dimensionless camber (ratio of maximum camber height to chord), while for a semi-circular arc airfoil exact nonlinear theory gives the result $4\pi\beta$.

Glauert[5] gives the required pitching moment, C_m, as

$$C_m = 2\mu - \pi\varepsilon_o/2$$

where

$$\mu = \int_o^1 -\frac{y(1-2x)}{\sqrt{x(1-x)}}\,dx$$

$$\varepsilon_o = \int_o^1 \frac{y}{\pi(1-x)\sqrt{x(1-x)}}\,dx$$

with y the camber height and x the chordwise position, both normalized on unit chord.

For a typical antisymmetric reflexed camber line given by the cubic

$$y = \beta 6\sqrt{3}\, x\,(1-x)(1-2x)$$

We can exactly compute the pitching moment to be

$$C_m = \pi\beta \, 9\sqrt{3} \, / \, 16$$

$$= 0.975 \, \pi\beta.$$

For a camber line consisting of two joined semicircular arcs μ can be exactly computed, but ε_o becomes logarithmically unbounded because of the infinite camberline slope at the trailing edge (x=1), as might have been expected from the small slope limitations of linear theory. This can be arbitrarily regularized by applying the procedure recommended in Glauert, which is to approximate the last 5% of the camberline by a straight line of finite slope having the same ordinate at 95% chord as the original camber line.

On this basis, for a camber line of a pair of semi-circular arcs, the moment is given by

$$C_m = 0.858 \, \pi\beta.$$

We note that this is slightly less than the cubic camber line, which is to be expected, since the maximum camber of the cubic occurs further out towards the tip than that of the circular arc camber.

Since the constant in the moment equation is approximately unity, it is convenient to introduce an effective camber, β_e, defined by

$$C_m = \pi \, \beta_e$$

This effective camber is now independent of the vane camber line details, but is approximately equal to the physical camber, for example, for a semicircular arc of physical camber β we find

$$\beta_e = 0.858\ \beta$$

5.2.6 Effect of Non-Uniform Induced Flow

The analysis so far has considered an induced flow which is uniform in the direction across the wind. This could be produced only by a wake containing no interior vorticity, that is having a vortex sheet only on its boundaries. This would imply that vorticity was shed from the vane only when it was at the $\theta = \pi/2$ position, that is at right angles to the wind. Now the main source of wake vorticity is the rate of change of vorticity induced by vane camber, this vane camber term varies like $\cos\theta$, so that its temporal gradient is like $\sin\theta$, indicating that vorticity is shed throughout the wake. However, we are not entitled to make the many-bladed, high-tip-speed-ratio ($NX \to \infty$) assumption used in Darrieus rotor theory, thus we must assume that the wake width varies in some approximately sinusoidal fashion. The wake vorticity and induced flow is shown in Figure 5.2.5. It will be seen that the axial induction, which relates to the drag, varies in a consistent way such that induction and drag are maximum at $\theta = \pi/2$.

It is thus clear that wake induction varies in both the wind-wise and cross-wind direction. It is believed that this effect is too complicated to take into account here, especially when other approximations inherent to the analysis are considered.

As a first-order approximation, which may be somewhat more realistic than the uniform wake assumed in the previous section we will assume that the wake varies in the cross wind direction (the sheared wake model) so that the local velocity at the rotor has the form

$$V_\infty(1-a \sin^2\theta)$$

We will still assume that the wake is uniform in the wind-wise direction.

Subject to this assumption, it is now necessary to equate the loads evaluated in the wake to the local vane loads. The wake loads can be estimated by standard momentum analysis, and this is done in the next section. The local vane load computation would be an extremely complicated procedure since the rotor is immersed in a highly non-uniform flow.

As an approximation, we will make the assumption that the major contribution to the mean lift load occurs when the vane is in the horizontal position so that we use the results for the vane in a uniform stream with velocity $V_\infty(1-a)$. For the drag force we assume that the major contribution occurs when the vane is approximately at right angles to the flow, and thus assume that we can define an equivalent uniform wake velocity of magnitude related to some mean position of the vane.

Under this sheared-wake assumption the onset velocity at any station on the vane is given by

$$V^1 = (1-a\sqrt{1-r^2\cos^2\theta}\,)/V_\infty$$

$$= V_\infty(1-a)S$$

where S is the sheared-flow factor and is given by

$$S = (1 - a\sqrt{1 - r^2\cos^2\theta}\,)/(1-a)$$

On this basis we obtain for the drag coefficient at the vane, C_D,

$$C_D = X\, C_m(1-a)S^2$$

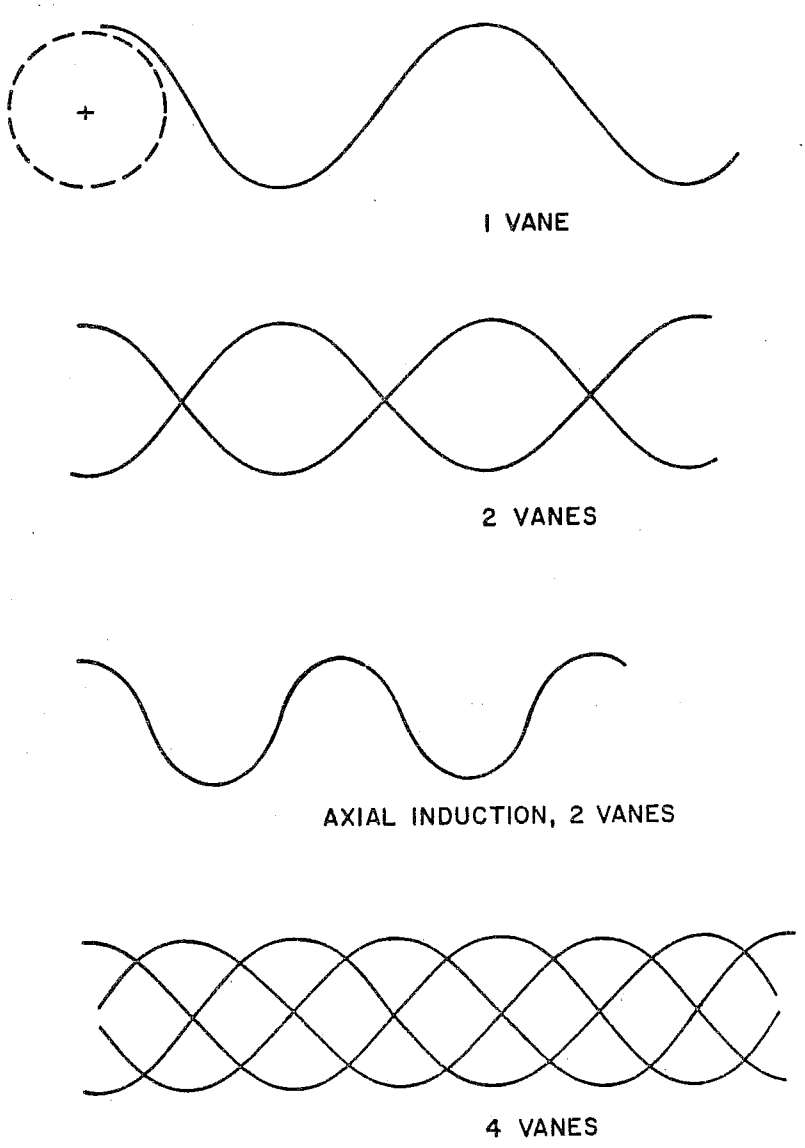

Figure 5.2.5 Wake Vorticity Geometry for Different Vane Numbers

The selection of S is certainly arbitrary but for our calculations we have simply used $r^2 = 1/4$, $\theta = 67.5°$.

Thus, for the local forces as computed in section 5.2.3, we obtain

$$C_L = X\pi(1-a)$$

$$C_D = X\, C_m(1-a)S^2$$

where S is the shear factor.

These local forces may then be used in the full three-dimensional force balance.

5.2.7 Three Dimensional Effects

Because the rotor experiences a cross-wind force which is of comparable magnitude to the drag force there will be a significant defelection of the wake in the cross-wind direction. This implies that the outer flow, which did not pass through the rotor will also be affected, and these considerations must be taken into account in determining the induced fields at the rotor.

Consistent with linear theory, we will assume that both the wind-wise velocity perturbation, a, and the cross-wind deflection angle, α, will develop to twice the value at the rotor when they are in the far downstream wake (the Trefftz Plane). This is shown in Figure 5.2.6. We use this assumption to determine the forces on the rotor, then equate to the forces determined directly on the rotor to obtain equations for α and a in terms of rotor geometry.

Forces in Trefftz Plane

As in the method used in V/STOL aerodynamics with powered wakes we must consider both the rotor flow from which energy has been removed, and the outer isoenergetic flow.

Rotor Flow

The force in the direction of the distant wind, F_x can be written

$$F_x = b \int_{-R}^{R} V_\infty [1-a(y)] 2V_\infty a(y) dy$$

where integration is performed across the rotor disc, of extent 2R.

For uniform flow this becomes in coefficient form with $C_x = F_x/V_\infty^2 Rb$

$$C_x = 4a(1-a)$$

For sheared flow of the form $a(y) = a \cos \theta$ with $y = R \sin \theta$ we get

$$C_x = \pi a(1 - \frac{8}{3\pi} a)$$

which will be seen to be a very similar expression.

The crosswind force, F_y, can be written in coefficient form as

$$C_y = 2\alpha \int_{-1}^{1} [1-a(y)][1-2a(y)] dy/R.$$

For uniform flow we get

$$C_y = 4\alpha(1-a)(1-2a)$$

While for the sheared flow we get

$$C_y = 4\alpha(1 - \frac{3\pi}{4} a + \frac{4}{3} a^2)$$

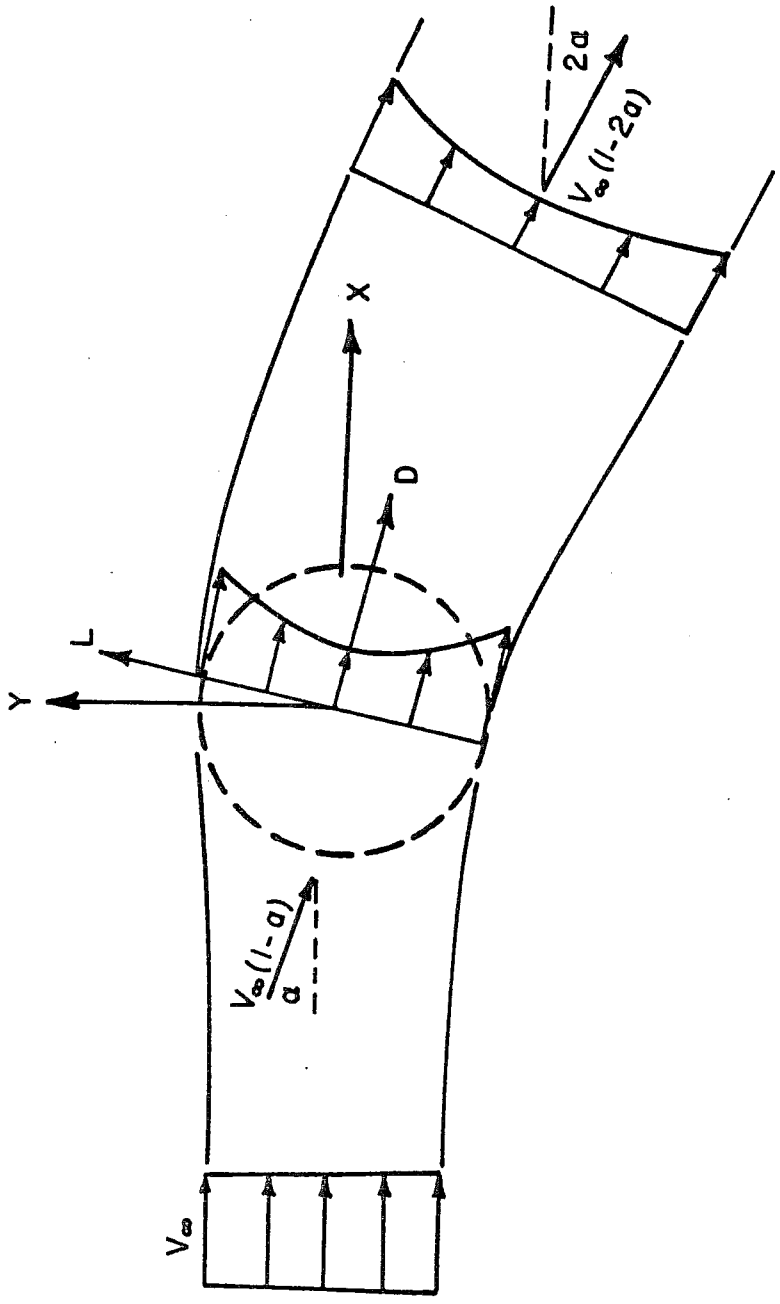

Figure 5.2.6 Induced Flows Near Rotor and in Trefftz Plane

Outer Flow

Here we consider the outer flow defelected by the cross-wind wash of the rotor flow. We can show that this flow corresponds exactly to the added mass of a rectangle of sides 2R, b. For cross flow normal to the span, b, this added mass is given by $\lambda\pi b^2$ where λ depends upon the aspect ratio, A, of the rectangle, given by $A = b/2R$.

The added mass constant λ can be determined by standard conformal mapping procedure. For our purposes, we need an operational formula. By curve fitting the exact results given by Wendel[6] we can show that

$$\lambda = 1 + 0.5/\sqrt{A} \qquad 1 < A < 10$$

with less than 1% error.

Then for the outer flow we get the second order expression

$$C_x^{\,o} = 2\alpha^2 \lambda\pi A/2$$

While for the cross wind force we get

$$C_y^{\,o} = 2\alpha\ \lambda\pi A/2$$

Rotor Forces

Recalling that the rotor forces were determined with respect to the local flow, which is inclined at an angle α we get

$$C_x = C_D(1 + \alpha C_L/C_D)$$

$$C_y = C_D(C_L/C_D - \alpha)$$

Equating Trefftz and Rotor Forces

Observing that because we are maintaining first order linear theory the drag term of the outer flow is negligble we obtain

$$(1 + \alpha C_L/C_D)C_D = C_X$$

$$(C_L/C_D - \alpha)C_D = C_y + C_y^{o}$$

It will be noted that the above pair of equations can be used to express a variety of cases, for example letting $A \to \infty$ recovers the result

$$X\pi\beta_e S = C_x$$

While reversing the sign of $X\beta$ either by rotating in the opposite direction, or reversing the camber gives a propulsive device adding power to the airstream. It may be noted too that letting $X \to 0$ recovers the correct tip-plated multiplane-lifting solution.

Then, writing $C_m = \beta\pi_e$ where β_e is the effective camber; $C_L = X\pi(1-a)$ and $C_D = A\, C_m(1-a)S^2$, we can simplify these equations. The cross-flow angle can be eliminated from the pair to give a quadratic in X, with L*, D* defined as force coefficients determined in the Trefftz Plane.

The quadratic becomes:

$$X^2\pi^2(1 + \beta_e^2 S^2) + X\pi\beta_e S(L^*-D^*) - L^*D^* \equiv 0$$

where

$$\alpha L^* = (C_y + C_y^{o})/(1-a)$$

$$D^* = C_x/(1-a)$$

For given vane camber, β, aspect ratio A, and induced flow profile $a = a(y)$ the above can be solved for X, then the inviscid power coefficient determined.

5.2.8 Results of Inviscid Calculation

The equations presented in the previous sections make it possible to compute torque or power coefficients for an arbitrary range of camber pitching moment and aspect ratio. If it is assumed that there is no central slot or gap, that is that the vanes are joined at the rotor axis, then these are the only variables. It is noted that there is an infinite range of camber line shapes, but according to this theory they can be collapsed if C_m, the vane pitching moment, is considered as the variable. It will be observed that this is very similar to monoplane wing theory, with the advance ratio, X, corresponding to wing angle of attack, and camber or pitching moment and aspect ratio playing similar roles in the rotor as they do in the wing. As in wing theory, the details of the camber line are only important if viscous effects relating to separation are significant.

Since most Savonius rotors have circular arc vane shapes, the inviscid performance curves are plotted for this type of camber line. The figures illustrate the effect of aspect ratio and magnitude of camber as well as the differences due to assuming uniform or sheared wakes.

Performance curves are shown in Figures 5.2.7 through 5.2.10. It will be noted that the aspect ratio effects are quite large and are still present even at aspect ratios of 10.

To illustrate the significance of the wake model, Figure 5.2.11 shows the different performances for a representative rotor of semicircular camber and aspect ratio 5.0 for the uniform or sheared wake assumption. It is evident that the wake model has a major effect on predicted inviscid performance.

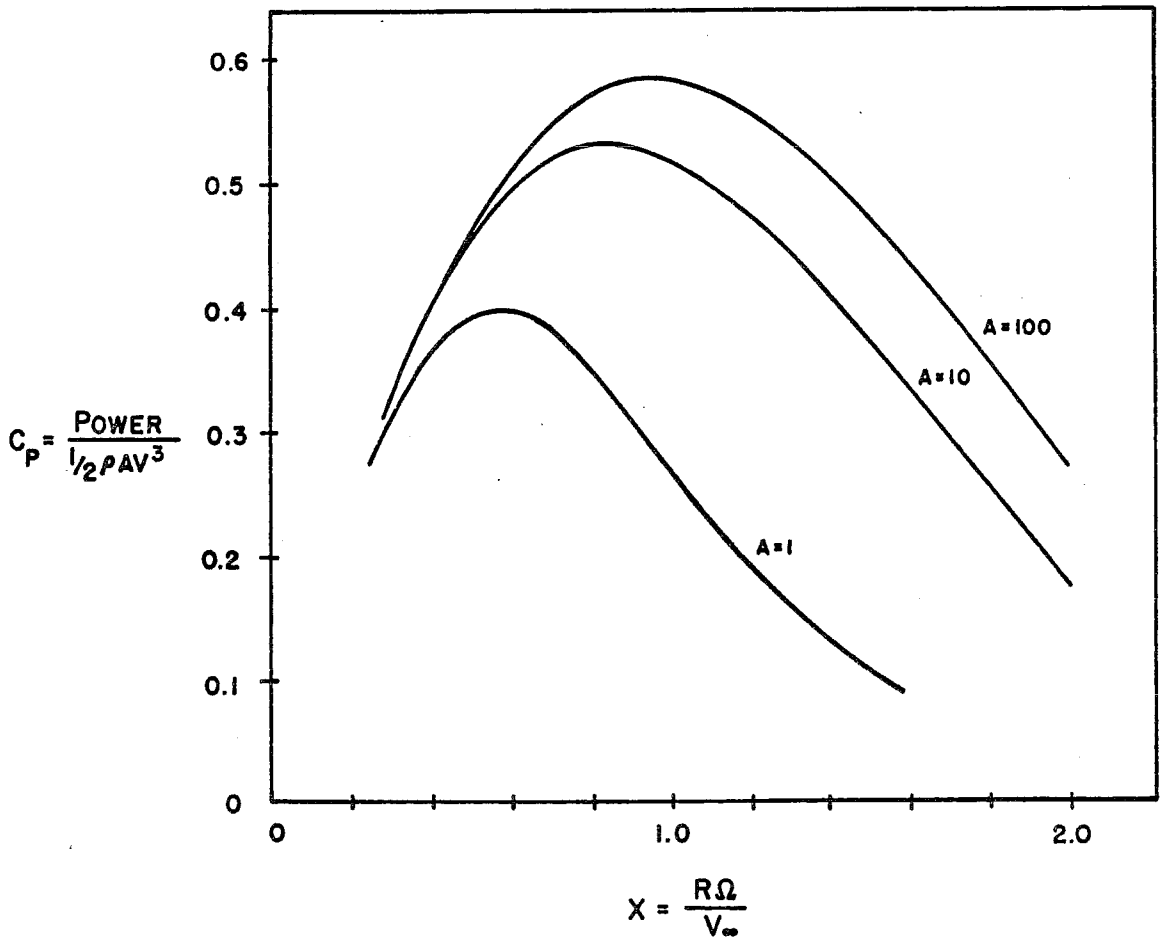

Figure 5.2.7 Inviscid Power Coefficient for Uniform Wake Model with Semicircular Vane (β = 0.5)

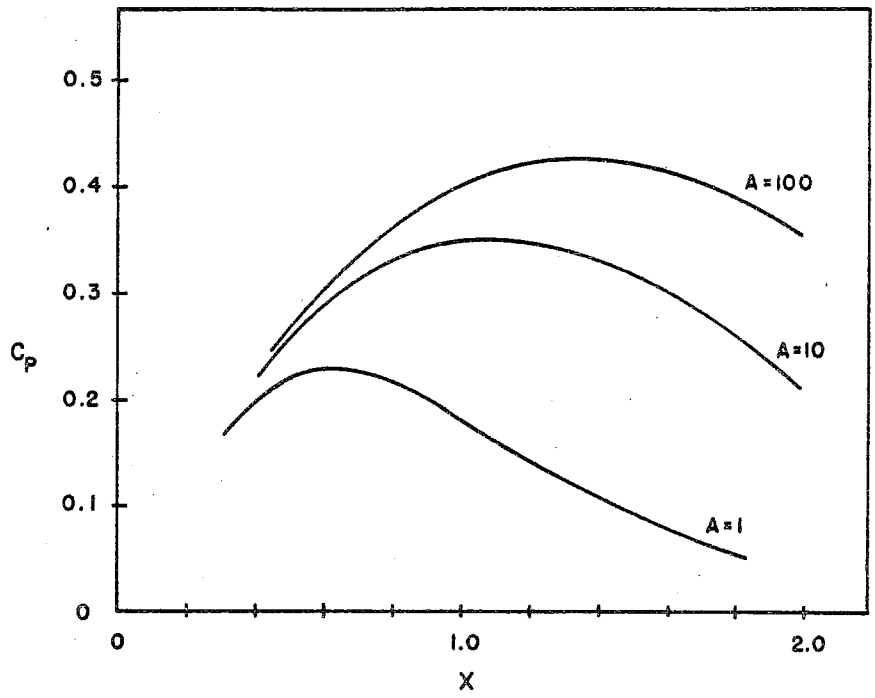

Figure 5.2.8 Inviscid Power Coefficient for Uniform Wake Model with Low Camber Vane (β = 0.25)

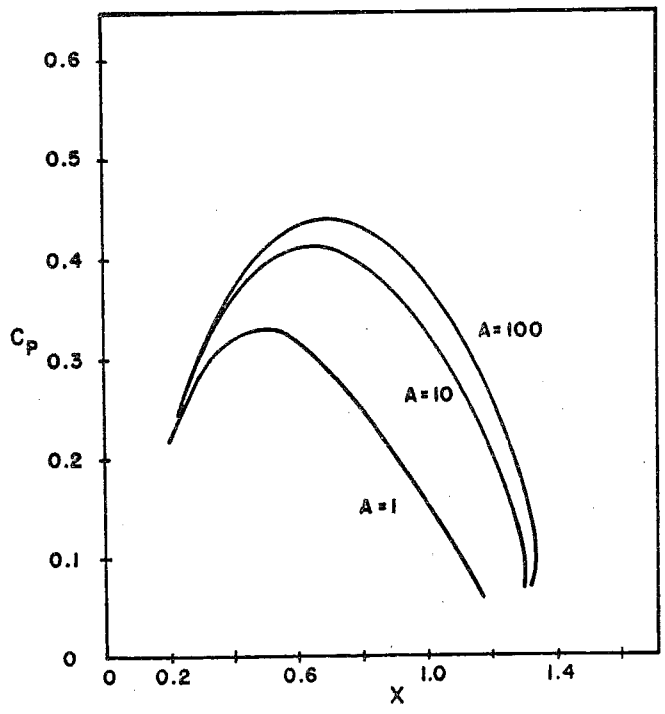

Figure 5.2.9 Inviscid Power Coefficient for Sheared Wake Model with Semi-circular Vane (β = 0.5)

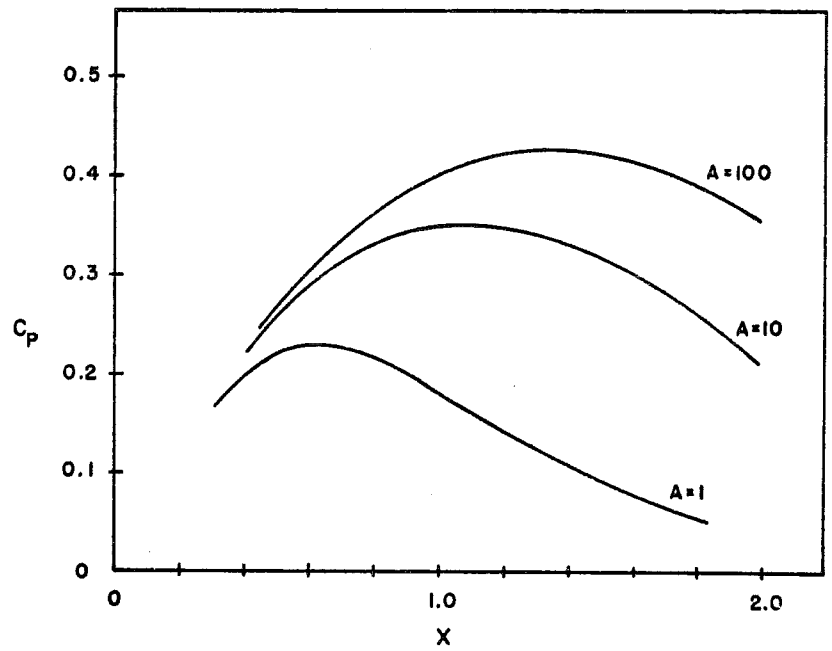

Figure 5.2.10 Inviscid Power Coefficient for Sheared Wake Model with Low Camber Vane (β = 0.25)

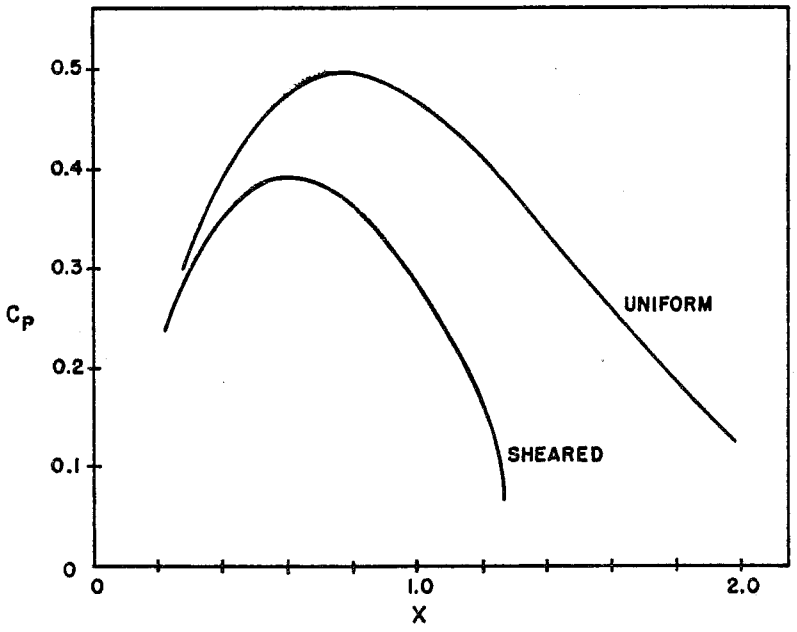

Figure 5.2.11 Comparison of Uniform and Sheared Wake Models for Typical Rotor (β = 0.5, A = 5)

5.3 VISCOUS EFFECTS ON POWER COEFFICIENT

5.3.1 General

It is to be expected that viscosity will cause the power coefficient to be lower than that computed by potential methods. For propeller type rotors and Darrieus rotors these effects can be treated quite adequately by methods already used in wing and airfoil analysis; that is, it is assumed that viscosity develops profile drag, that is a force roughly parallel to the airfoil chord. This force then can be introduced into the torque equation where it normally appears as a term resisting rotation and hence reducing the torque produced in ideal flow. It is of interest to note that for the Savonius rotor, any direct-skin-shear stress due to viscosity will not produce a significant effect on the torque because of the geometry of the rotor.

However, it is probable that the viscous effects are indeed large. We have no direct estimation of this, because there are no results comparing test data with the potential flow solution. Wind tunnel corrections due both to wake blockage and to wake deflection can be large, and as pointed out by Newman[7] some previously published test data may require adjustment for tunnel corrections. However, Newmans reports shows two factors indicating the importance of viscous effects. The first is that the maximum C_p is about 0.18 when theoretical considerations suggest one might achieve at least about 0.30, the second is the quite distinct deterioration of rotor performance for reduction in free-speed Reynolds number. Here, Newman shows a degradation of C_p from about 0.30 to 0.28 for Reynolds number changes from 1.9 a 10^5 to 1.0 x 10^5. Note this is tunnel C_p, which must be reduced by about 30% for wall effects.

We have pointed out that to obtain viscous power losses of this magnitude, one cannot expect skin shear terms to do it. Thus we must search for a mechanism by which the viscous effects can create pressure perturbations on the vanes. One obvious mechanism is separation from the advancing vane, changing the unsteady potential pressures. A further mechanism is viscous pumping by which the angular velocity causes the boundary layers on the vane to flow radially outwards towards the tips. Presumably the modified boundary layer displacement thickness due to this will change the vane effective camber, so that the pressure fields on the vane will differ from those computed in the inviscid case. Thus this does constitute a mechanism by which viscous effects can produce pressure pertubations on the blades without separation occurring.

A further viscous effect which will reduce output power of the rotor occurs at the tip plates. Frequently these are circular discs of radius somewhat larger than the rotor radius. This is the only place where viscous shear produces direct power loss torque and, although the mechanism can easily be visualized, there is no valid theory for the torque on a rotating plate in a uniform flow.

Some estimates of the magnitude of these viscous power losses in attached flow has been made and is described in the next paragraphs. It will be seen that the losses do not appear to be of sufficient magnitude to account for the actual loss which is believed to occur.

5.3.2 Estimate of Viscous Losses in Attached Flow

Tip Plates

The torque on a circular disc of radius R*, rotating at an angular velocity of Ω can be defined in terms of the mean torque moment C_M^* where

$$C_M^* = 2M/(1/2\ \rho\Omega^2 R^{*5})$$

with M being the torque for a disc wetted on both sides.

The torque coefficient C_m^* has been given (Schlichting[8]) in terms of rotational Reynolds number, R_Ω, (= $R^* \Omega/\nu$) as

$$C_m^* = 3.87 \ (R_\Omega)^{-1/2} \qquad R_\Omega < 5 \times 10^4$$

$$= 0.146 \ (R_\Omega)^{-1/5} \qquad R_\Omega > 5 \times 10^5$$

The value of C_m^* in the intermediate transition range $5x10^4 < R_\Omega < 5x10^5$ depends upon plate roughness.

For two fully wetted side plates we obtain the viscous power loss, C_{p_v}, in standard coefficient form as

$$C_{p_v} = \frac{C_{m^*}}{4A} \ X^3 r^5$$

where A is the rotor aspect ratio 2R/h and r the ratio of tip plate size, R', to rotor radius R, that is r = R'/R. For an estimate of the magnitude of this effect we consider the tests reported by Newman[7].

Here we take a rotor of aspect ratio 1.50 with r ≃ 1.0. At X ≃ 1, we get $R_\Omega \simeq 1.20 \times 10^5$ giving $C_{p_v} \simeq .010$. Since the maximum measured corrected power coefficient is of order 0.20 at X = 0.90 these viscous terms are not large enough to grossly affect the character of the inviscid calculations. We note that the formula for disc torque used here is strictly for a disc rotating in still air, and thus could not be a good approximation for tip speeds significantly greater than zero, still the power loss due to the tip plates appears to be about an order of magnitude less than that actually occurring.

Viscous Induced Torque Losses on Vane

Evidently we cannot at this stage compute the boundary layer on the vanes themselves. However, a crude estimate can be made using the assumption that the vane camber is reduced proportionately to the boundary layer displacement thickness. If we assume that there is some effective boundary layer displacement thickness, δ^*, on the vane, which is directly functionally related to the drag of the vane when regarded as an airfoil then

$$\delta^*/R = k\ C_D$$

where k is expected to be of order one, and C_D is the profile drag coefficient at the appropriate Reynolds number. Then, assuming the C_M, the vane pitching moment is a function of effective camber, we estimate that the ratio of viscous power loss due to vane boundary layers to inviscid power must be

$$C_{p_v} = k\ \ C_D\ X\ (1-a)^2$$

$$C_{p_v}/C_p = k\ C_D/C_M$$

To roughly estimate C_D we simply use data given by Schmitz[8] for flat and cambered plates at low Reynolds number. Schmitz gives C_D values between 0.01 and 0.04 at Reynolds number of about 0.75×10^5. Noting that C_M is about 0.5 for semicircular vanes, we note that this correction appears to be at most 1/10 of the inviscid power.

5.3.3 Heuristic Approach to Viscous Correction

As explained, the various attached flow viscous corrections do not appear to be of sufficiently large magnitude. However, we have one set of test data (Newman[7]) in which the measured performance (C_p versus X) of a rotor is plotted for three different Reynolds numbers. In principal this provides sufficient information to infer the viscous correction, if we postulate some general functional dependence. To a certain extent, this dependence can be estimated by examination of the differences in power coefficient for varying Reynolds number while holding tip speed ratio fixed. Extracting this data gives rise to a pair of curves (uncorrected for wind tunnel constraint) giving the difference in correction at different Reynolds numbers as a function of tip speed ratio. If the viscous power (uncorrected) is assumed to be of the form

$$C_{p_{vT}} = (a + b\ X^{\alpha})R^{\beta}$$

where R is the Reynolds number based on free stream speed and vane diameter ($2VR/\nu$) we propose a viscous power term of the form

$$C_{p_{vT}} = 7.5(1 + X^{3/2})/R^{1/3}$$

where constraints and exponents have been deliberately rounded off to express the approximate nature of the computation.

The quality of this fit is shown in Figure 5.3.1. Here we have plotted the difference in power coefficient $\Delta C_p^{\ o}$ from that occurring at R = 100,000 from the power coefficients at R = 160,000 and R = 190,000. It will be

seen that this is a reasonable fit for tip speed ratios in excess of 0.6. For tip speed ratios lower than this it is expected that the flow separation is of a different nature.

We must now adjust this result for the tunnel constraint. Because of the very approximate nature of this approach we will not attempt to compute a tunnel correction varying with tip speed ratio but simply use the maximum correction employed in the reference paper, here in Figure 5.2.8 of Newman[7] a correction on measured wind tunnel power coefficient of 0.651 is shown. Thus we modify the uncorrected viscous power term to propose a corrected viscous power loss.

$$C_{p_v} = 4.9(1 + X^{3/2})/R^{1/3}$$

We note that this will give much larger values of the viscous power coefficient than the previous estimates, for example, for the rotor tested by Newman at diameter and free stream based Reynolds number of 1.9×10^5 we get viscous term, C_{p_v}, of about 0.17. This term is much larger than those computed previously.

This correction is of interest since it was derived without reference to the basic uncorrected result; thus if the viscous correction could be considered accurate, it would serve as a means of checking the inviscid potential theory. However, it is noted that at this point in the state of the art, neither the viscous correction nor the inviscid model can be considered sufficiently reliable to serve as a check for the other.

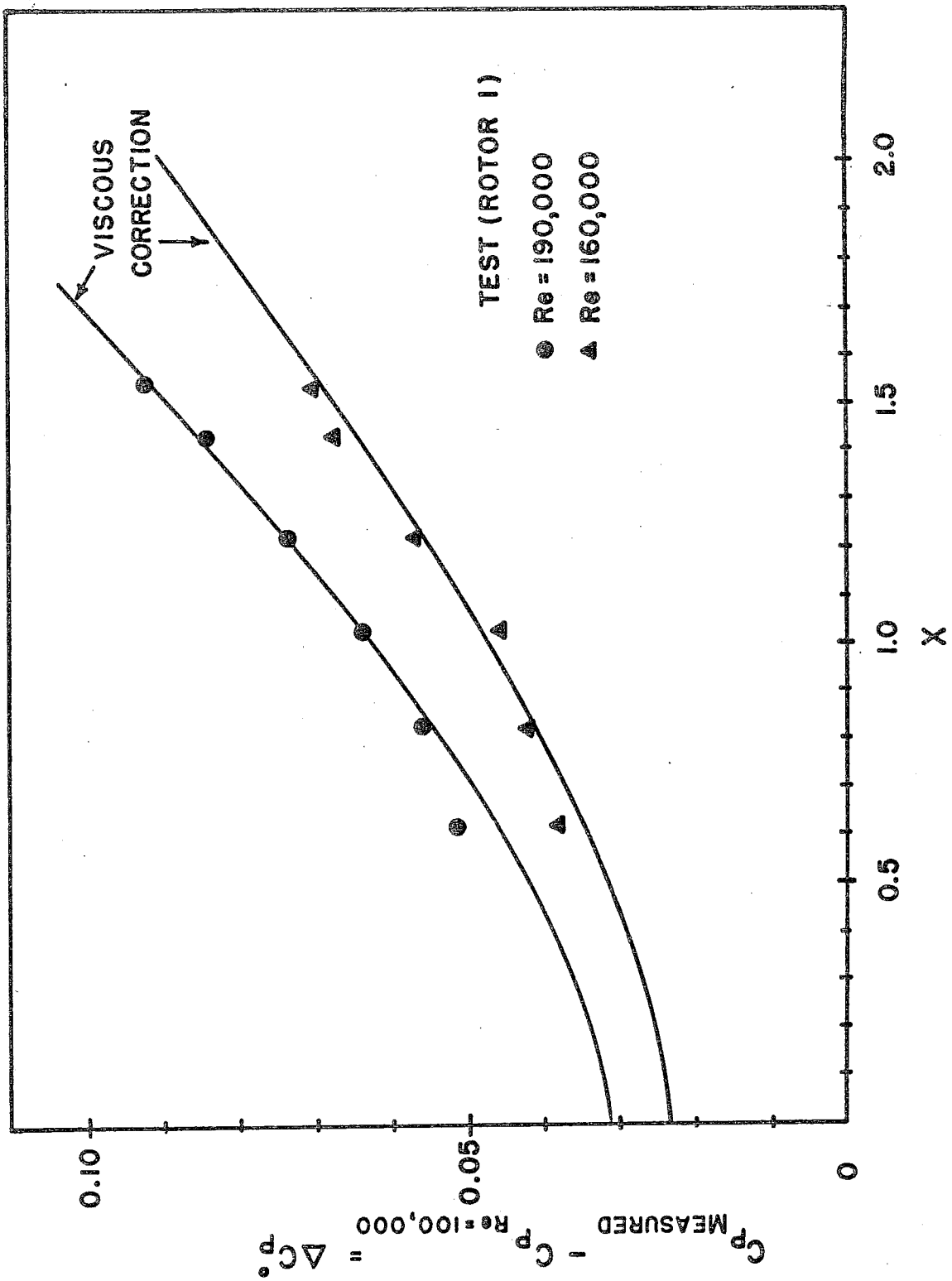

Figure 5.3.1 Comparison of Viscous Correction with Test

5.4 CORRELATION WITH EXPERIMENT

Although there is a reasonable amount of test data on Savonius rotors (Savonius[1], Bach[10], Simonds and Bodek[11], Mercier[12], and Newman[7], it is not easy to use these results for comparison with the present theory. The reason is principally that the free tests in the natural wind involve necessarily poorly controlled measurements, while the wind tunnel data normally involves a very large and uncertain wind tunnel correction to convert to free air data. The nature of this correction relates to two effects; the change in incoming flow speed, and circulation changes due to wall constraints.

The Wall Constraints

The first effect occurs with both wind axis (propeller) and cross-wind axis machines and is accounted for by blockage (solid and wake) corrections. Due to this blockage and the wall confinement, the flow speed at the rotor is higher than it would be in a free flow. The rotor thus generates forces and powers associated with higher free wind speeds than the nominal tunnel speed measured by instruments upstream of the working section. If power coefficients are computed on the nominal tunnel speed they must then be reduced to account for wall constraint. This correction can be appreciable since it is related to the cube of the speed, and the speed itself may require a 10% correction.

The second effect occurs with cross-wind axis machines only. Here the device develops a cross-wind force, causing a cross-wind deflection of the incoming stream. As has been shown in the section on Aspect Ratio Effects the general effect of this deflection is to reduce the power output of the device. The effects of wall constraints are to reduce the wake deflections, so that the device tested appears to be of higher aspect ratio than implied by its physical dimensions.

A theory for tunnel corrections where there is no cross-wind force has been given by Durand[13]. No theory for the correction with cross-wind force exists, but such analysis could be developed using the finite span analysis given here coupled with appropriate imaging.

We note the significant result, that both the wind speed and deflection correction will reduce the measured wind tunnel power coefficients, or alternatively, the tunnel tests will always apparently give higher powers than those occurring in free flow. The magnitude and nature of this correction is discussed by Newman, and a tunnel constraint correction is applied to Newmans data, however, it is not clear whether the important lift induced correction has been applied, or if only the solid and wake blockage correction terms are used. It should also be noted that the test data of the different references is in general for different tunnel blockages, Reynolds number and Aspect Ratios as well as for different vane shapes. Thus it is not possible to examine the existing results for mutual consistency, except to note that the experiments agree to within about 30% for power, lift and drag coefficients.

In order to attempt to compare the existing theory it was decided that the case most directly similar to the model developed in the present paper was Rotor I of Newman[7]. This rotor has vanes of semicircular cross section, with no gap, and is thus similar to the theoretical model used to determine the vane pitching moment. The heuristic viscous power correction derived in Section 5.3 is applied to the inviscid results for both the uniform and sheared wake models.

Now, it is noted that although the viscous power correction was in fact derived from Newman we are not using a self-justifying model in comparing with Newman's results, since as pointed out in Section 5.3 there is sufficient data in Newman to permit one to estimate the viscous power correction without making assumptions about the inviscid power.

Thus the total power coefficient for a semicircular rotor ($\beta = 0.50$) of aspect ratio 1.25 and Reynolds number 190,000 was computed for the uniform and sheared wake models. This is shown in Figure 5.4.1 when it is compared with the test results of Newman. These results are presented uncorrected for tunnel wall constraints in Newman and no correction is given for Rotor I. Thus we have assumed the correction for Rotor I is the same as that for Rotor IV, since for this case tunnel and corrected data are given in Newman. The corrected test curve is shown in Figure 5.4.1 but it must be recalled that the accuracy of this correction is very much in question.

We reiterate that there are fundamentally two uncertainties in this correction. The first is that the correction given by Newman for Rotor IV has been used for Rotor I, although there are significant differences between the rotors. The second, as mentioned by Newman, is that even the correction for Rotor IV is open to question. For this reason we have shown an estimated correction band in Figure 5.4.1.

It will be seen by examination of Figure 5.4.1 that the present theory appears to approximately represent the main features of the performance but that there are significant discrepancies, both in the magnitude of the peak power coefficient and the tip speed ratio at which it occurs. The uncertainties in the tunnel corrections creates difficulty in making any statements about the peak power coefficient. However, the tip speed ratio for peak power is not as strongly affected by the tunnel correction, and Figure 5.4.1 suggests that the theory proposed here requires modification to increase the tip speed ratio at peak power.

Although it is recognized that the inaccuracies described imply that the corrected test results for Rotor I do not constitute a very critical test of our analysis, we now discuss some ad hoc adjustments to the theory which will bring the curves into better correspondence. First we note

(Figure 5.4.2), assuming the viscous power correction is approximately correct in magnitude, that changes in Reynolds number of the magnitude associated with the tests, will not have a very large effect.

Then observing (Figure 5.4.1) that the uniform wake model appears nearer to the test data than the sheared model we confine our attention to correcting the former by changing vane camber and aspect ratio.

As expected, the magnitude of vane camber has a large effect on the peak power coefficient, but causes little change to the tip speed ratio at which this occurs, as illustrated in Figure 5.4.3. On the other hand, raising aspect ratio increases the power at higher tip speed ratio with minor changes in magnitude of peak power (Figure 5.4.4).

It appears that a value of vane camber represented by $\beta = 0.30$ gives a fairly good fit to the test results for Rotor I for assumed aspect ratios between 2.0 and 3.0. This is illustrated in Figure 5.4.5, where the estimated test performance of Rotor I from Figure 5.4.1 has been superimposed on the analytical results of Figure 5.4.4. For construction of the theoretical curves of Figure 5.4.5 the uniform wake model, with $\beta = .30$, and the proposed viscous power correction with $R = 190,000$ was used. It is noted that the actual proportion of Rotor I were $\beta = .50$, $A = 1.25$. Evidently the severe blockage will produce lift effects, so that the effective aspect ratio in the tunnel is increased possibly to 20, but as explained, this effect can not be quantitatively accounted for without developing a valid cross-flow power correction.

Thus at this stage, with the very inadequate data, it is believed that a pair of equations, one for the inviscid power and one for the viscous power correction can adequately represent the power output of the Savonius Rotor. The cross-wind force (lift induced) effect is large, and has a large

influence on the rotor performance. Separation effects also appear to be important but we have no information on their relative significance at different tip speed ratios.

There is not enough good experimental data to check either the inviscid power predictions, the viscous corrections, or the tunnel wall corrections. However, it is believed that the analytical developments presented here make it possible to establish the proper form of the Savonius Rotor performance equations and to establish constants and correction terms in these equations.

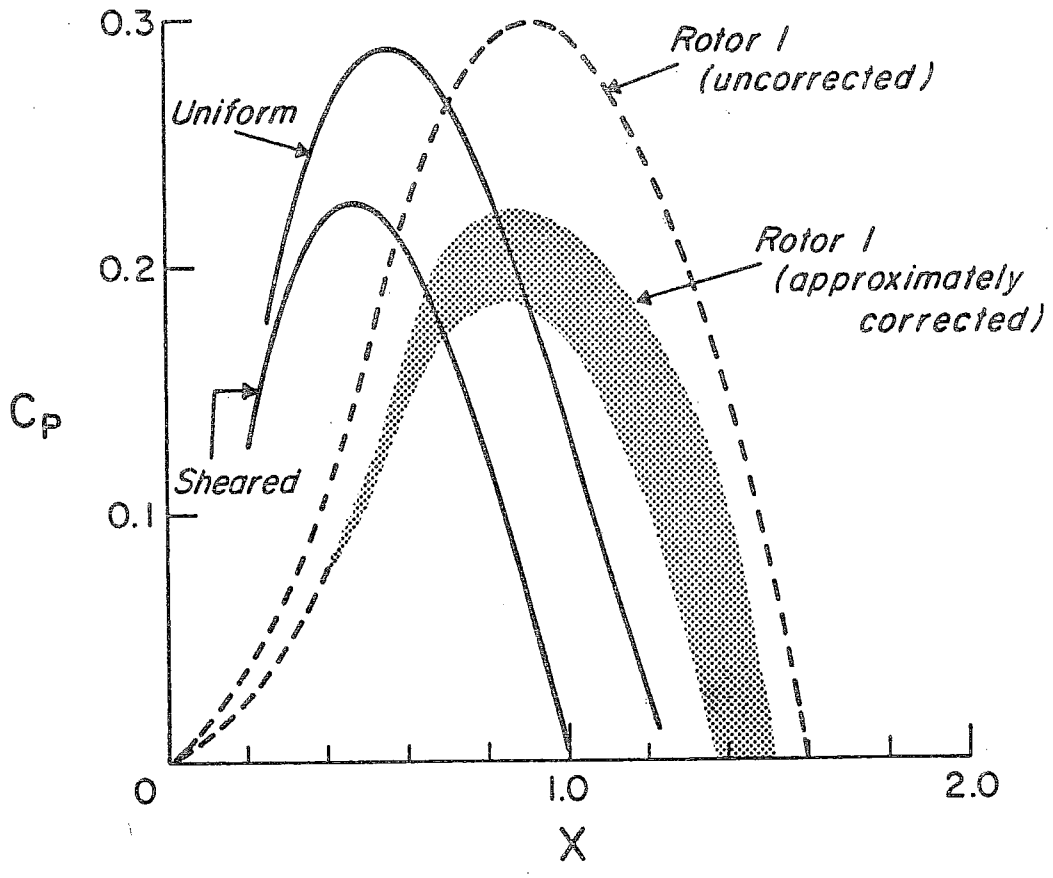

Figure 5.4.1 Estimated Power Coefficient with Viscous Correction for Newmans Rotor I (β = 0.5, AR = 1.25, Re = 190,000)

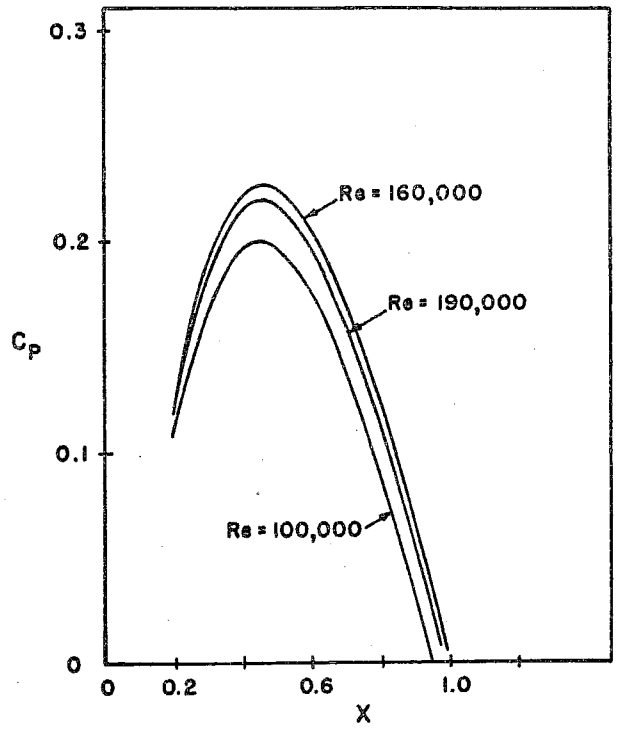

Figure 5.4.2 Effect of Reynolds Number on Power Coefficient (β = 0.5, AR = 1.25)

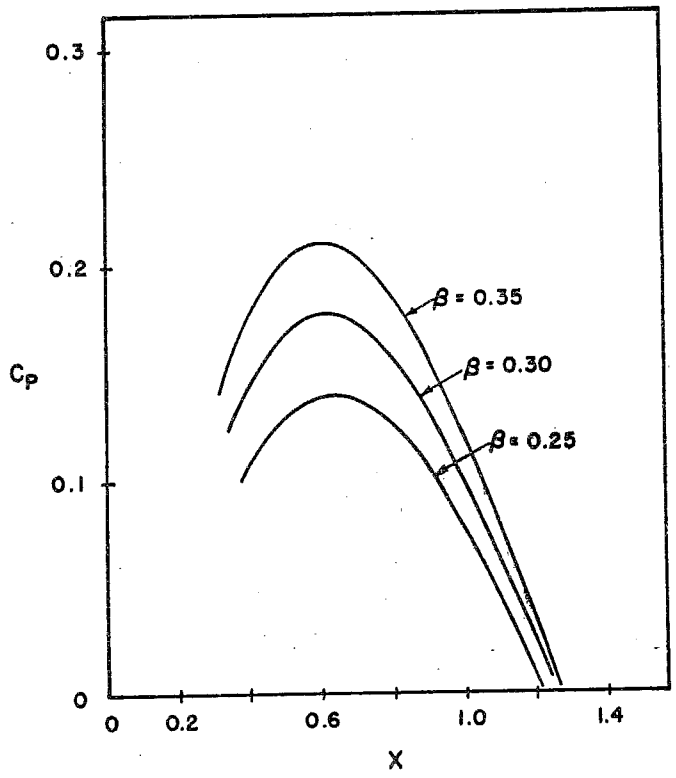

Figure 5.4.3 Effect of Vane Camber of Power Coefficient (AR = 1.25, Re = 190,000)

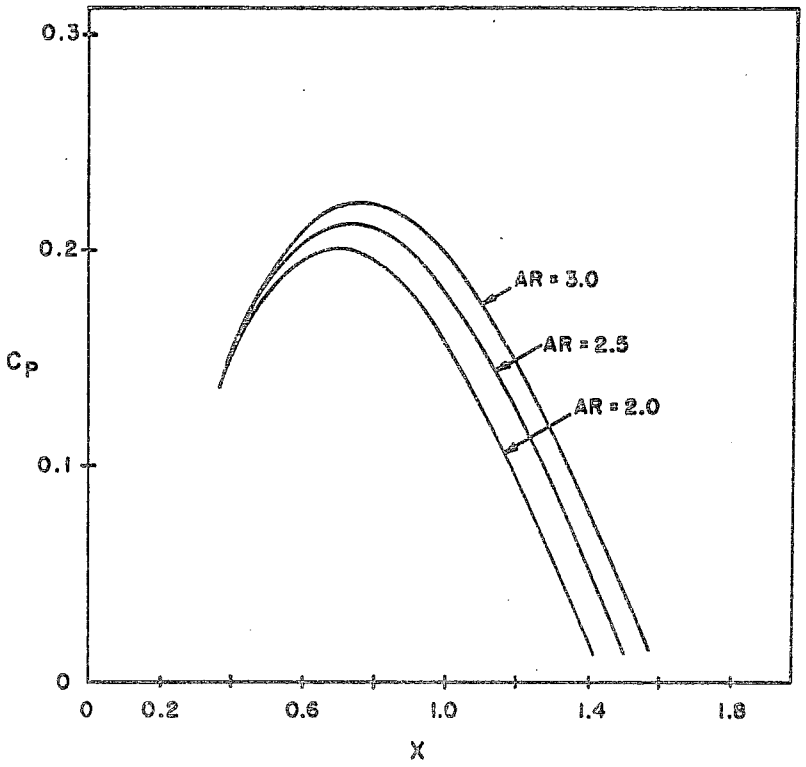

Figure 5.4.4 Effect of Aspect Ratio on Power Coefficient (β = 0.30, Re = 190,000)

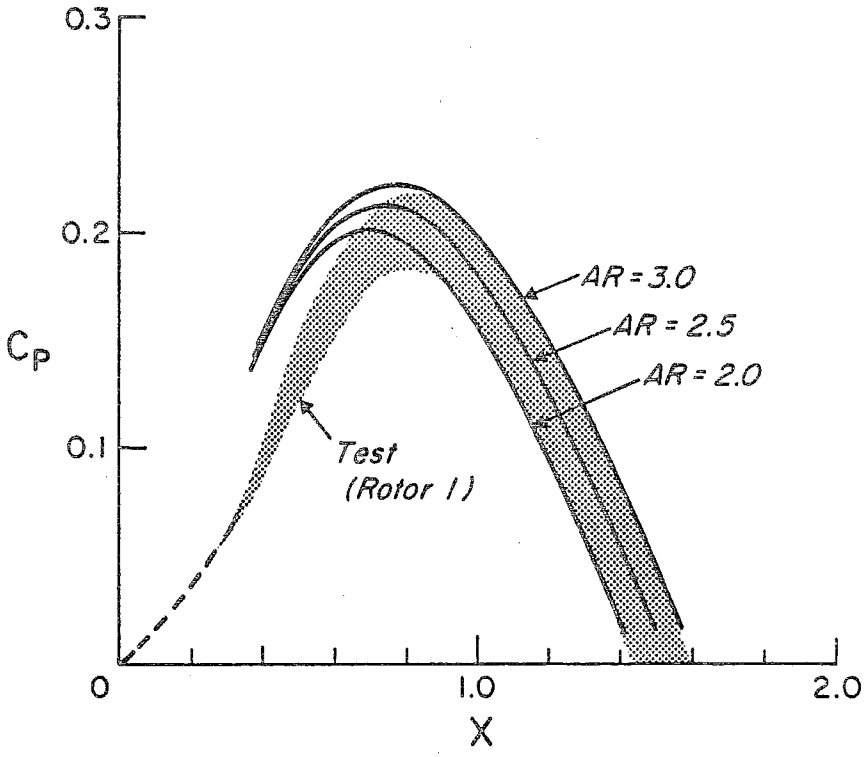

Figure 5.4.5 Power Coefficient of Rotor I compared with Present Theory (β = 0.30, Re = 190,000)

REFERENCES

1. Savonius, S. J. The S-Rotor and Its Applications, Mechanical Engineering 53, pp. 333-338, 1931.

2. Vertical Axis Rotor Smoke Flow Study (film), Edgewood Arsenal.

3. von Kármán, T. and Sears, W. R. "Airfoil Theory for Non-Uniform Motion," Journal of the Aeronautical Sciences, Vol. 5, No. 10, 1938.

4. Hunt, J. N. Incompressible Fluid Dynamics, John Wiley & Sons, 1964.

5. Glauert, H. The Elements of Aero Foil and Airscrew Theory, Cambridge University Press, 2nd Ed., 1948.

6. Wendel, Kurt. Hydrodynamic Masses and Hydrodynamic Moments of Inertia. Jahtb.d STG, Vol. 44, 1950.

7. Newman, B. G. Measurements on a Savonius Rotor with Variable Gap. Sherbrooke University Symp. on Wind Energy, May 1974.

8. Schlichting, H. Boundary Layer Theory, McGraw-Hill Co., 4th Ed., 1960.

9. Schmitz, F. W. Aerodynamics of the Model Airplane, 1942, translated by Redstone Scientific Information Center, 1967, WTIS, N70-39001.

10. Bach, von G., Untersuchungen uber Savonius-Rotoren und verwandte Stromungsmaschienen, Forsch. auf dem Gebiete des Ingenieurwesens, 2, pp. 218-231, 1931.

11. Simonds, M. H. and Bodek, A. Performance Test of A Savonius Rotor, Brace Research Institute, T. R. T10, McGill University, 1964.

12. Mercier, John A. Power Generating Characteristics of Savonius Rotors, Davidson Lab., Stevens Institute of Technology, Report 1181, 1966.

13 Durand, W. F., Aerodynamic Theory, Gugenheim Fund, 1943.